ELECTROSTATIC PROPULSION BEAM DIVERGENCE EFFECTS ON SPACECRAFT SURFACES

VOLUME III
FINAL REPORT

TRW NO. 11985- 6003-RU-00

R. F. KEMP, D. F. HALL, AND E. E. LUEDKE

15 SEPTEMBER 1973

CONTRACT NO. 952350

Prepared for

JET PROPULSION LABORATORY

CALIFORNIA INSTITUTE OF TECHNOLOGY

PASADENA, CALIFORNIA

TRW
SYSTEMS GROUP

ELECTROSTATIC PROPULSION BEAM DIVERGENCE EFFECTS ON SPACECRAFT SURFACES

VOLUME III
FINAL REPORT

TRW NO. 11985-6003-RU-00

R. F. KEMP, D. F. HALL, AND E. E. LUEDKE

15 SEPTEMBER 1973

CONTRACT NO. 952350

Prepared for

JET PROPULSION LABORATORY
CALIFORNIA INSTITUTE OF TECHNOLOGY
PASADENA, CALIFORNIA

TRW
SYSTEMS GROUP

CONTENTS

PRECEDING PAGE BLANK NOT FILMED

CONTENTS (Continued)

1. INTRODUCTION

1.1 BACKGROUND

This volume is the fifth in a series of Contract Final Reports covering a program of research into the effects of electrostatic thruster effluents on spacecraft surfaces. Pertinent information relative to these volumes is summarized here:

First Volume: "Evaluation of Electric Propulsion Beam Divergence and Effects on Spacecraft," TRW Report 08965-6013-RO-00, 2 September 1969, Final Report to NASA, Pasadena Office on Contract NAS7-575 (Reference 1). Period of performance was from July 1967 to September 1969, Phase I.

> This volume constituted a survey and statement of the problem. It defined an experimental facility and test program required to elucidate information not then available. Consideration was given to erosion, chemical, metallurgical, and electrical effects of thruster propellant materials, both ions and neutrals, on spacecraft thermal control coatings. Extensive appendices considered evaluation of thruster exhaust, proposed sample lists, vacuum contaminants, properties of mercury and cesium, and error analysis of proposed test methods.

Volumes two through five have the common title, "Electrostatic Propulsion Beam Divergence Effects on Spacecraft Surfaces," Final Report, Contract No. 952350, to Jet Propulsion Laboratory, California Institute of Technology, as sponsored by the National Aeronautics and Space Administration under Contract NAS7-100. These four documents include Volumes I, II, III, and an addendum to Volume II of this final report (this book is Volume III).

Volume I: (Reference 2) Period of performance of reported work was from February 1969 to May 1970, Phase II.

> Work progressed in four major areas: chemistry, metallurgy, thermophysics, and surface and vacuum physics; the aim was to elucidate interactive mechanisms between ion thruster effluents and spacecraft materials. Experiments in the first two areas involved immersion of samples in liquid cesium and mercury. In the latter two areas, a spacecraft surface contamination experimental facility was designed and set up, including special sample holders, heat-flux meters, a quartz crystal microbalance, and means for measuring thermophysical properties of samples without removing them from the vacuum environment. Preparations were

made for the Phase III experimental program. Improvements were made in problem definition and in mathematical models. It was recognized that sputtered grid material would be a potential contaminant source.

Volume II: (Reference 3) Period of performance was from June 1970 to July, 1971, Phase III.

This volume presents models of ion thruster effluents and models describing the degradation of spacecraft surfaces by these effluents. emphasis was given to measuring, understanding, and predicting the effects of impinging particles, given their species, impingement rates and energies. Substantial quantities of basic experimental data were obtained. Potential solutions to contamination problems were suggested.

Volume II, Addendum No. 1: "Ion Time-of-Flight Determinations of Doubly to Singly Ionized Mercury Ion Ratios from a Mercury Electron Bombardment Discharge", (Reference 4). Period of Performance was from January to December 1972, part of Phase III.

An electrostatic-switching time-of-flight ion analyzer was designed, fabricated and used to measure the ratio of Hg^{++} to Hg^+ ions in the beam of a 20-centimeter mercury ion engine supplied by the Jet Propulsion Laboratory. The ++/+ ratio was measured for a range of beam current from 0.25 to 0.91 ampere and for a range of discharge anode voltage from 22 to 60 volts. Comparison of laboratory data with an analytical model of ion production clearly indicates that formation of the ++ ion is a two-step process. The data are useful in specifying an operating parameter for ion engine integration and mission design. A parametric description of the ++/+ ion production ratio is given.

Volume III: (This Volume) Period of Performance, August 1971 to August 1973, Phase IV.

The Phase IV effort reported herein is an application of results and techniques from earlier portions of the program to a particular ion engine spacecraft configuration. It is an extensive analytical and experimental examination of the compatibility of the ATS-F Ion Engine Experiment with engineering subsystems and other experiments on the ATS-F spacecraft. While thus specifically motivated and directed, new techniques have been added and additional insights have been gained. Hence, many of the results and techniques will be of wide interest and usefulness.

References 5 through 9 are papers through which results from this program have been communicated to the electric propulsion community.

Section 2 gives the context for this phase of the program in terms of the relationship of the ATS-F ion engine experiment[10, 11] to other space-craft experiments and subsystems. Section 3 reviews the experimental facility and gives details of the cesium ion source used in this phase of the program.

The effort of the Phase IV program was itself divided into four parts. In the first part, a broad examination was made of a rather large number of samples of spacecraft materials in order to identify any for which unexpected reactions might occur. These samples were subjected to both cesium atomic beams and to high- and low-energy cesium ions. The results are given in Sections 4 and 5. In another part of the program, still other types of spacecraft material not readily adaptable to the same type of measurements or mounting were subjected to high concentrations of cesium vapor in order to determine, primarily whether any unexpected mechanical effects would be produced. The results of these experiments are covered in Section 6. In the final series of experiments, selected spacecraft materials were subjected to impingement by low-energy cesium ions, and to backsputtering of spacecraft materials by high-energy cesium ions. The results of these tests are given in Sections 7 and 8. As the fourth part of the program, a detailed diagnostic study was made of the plasma thrust beam of a flight-model ATS-F ion engine. Measurements were made of such plasma properties as beam current density and energy as functions of angle from the thrust beam axis, and of plasma potential and electron temperature as functions of neutralizer bias. Details of this study are reported in Section 9.

2. SENSITIVE SURFACES ON THE ATS-F SPACECRAFT

2.1 ATS-F CONFIGURATION

With the successful launch of the ATS-F spacecraft in early 1974, a major step will have been taken to extend the benefits of geosynchronous communications satellites, now so well known in intercontinental communications, to direct intracontinental uses. In addition, extended environmental, resources, and space-sciences experiments will be performed. This huge spacecraft, shown in deployed configuration in Figure 2-1, is 7.99 meters (26.2 feet) in length, has a main (steerable) antenna which is 9.15 meters (30 feet) in diameter, and has a total span between deployed tips of solar panels of 16.7 meters (54.8 feet).

2.1.1 Experiment List

The importance of ATS-F to intracontinental communications and environmental science can be judged from the proposed list of experiments below:

High Resolution Radiometer. A high resolution meteorological camera will refine concepts of meteorological research, taking pictures day and night in visible and infrared spectra. The infrared radiometer will operate at $100^{\circ}K$, and its temperature will be maintained by a north-viewing "cold patch" surrounded by a high-infrared-reflectance "cooler cone".

Millimeter Waves. Propagation data will be obtained at 20 gHz and 30 gHz which will define near-earth propagation path characteristics for use of future communications satellites.

Environmental Measurements. Eight scientific experiments will study solar cosmic rays; radiation damage to solar cells; electrons, protons, and alpha particles; and the earth's magnetic field.

Cesium Ion Engine. Two cesium microthruster subsystems will be used to demonstrate the capability of electric propulsion systems to provide station-keeping support, with spacecraft compatibility.

Propagation. Data will be gathered at 13 gHz and 18 gHz to determine millimeter-wave attenuation due to rainfall.

COMMUNICATIONS

SERVICE

EXPERIMENTS
MODULE
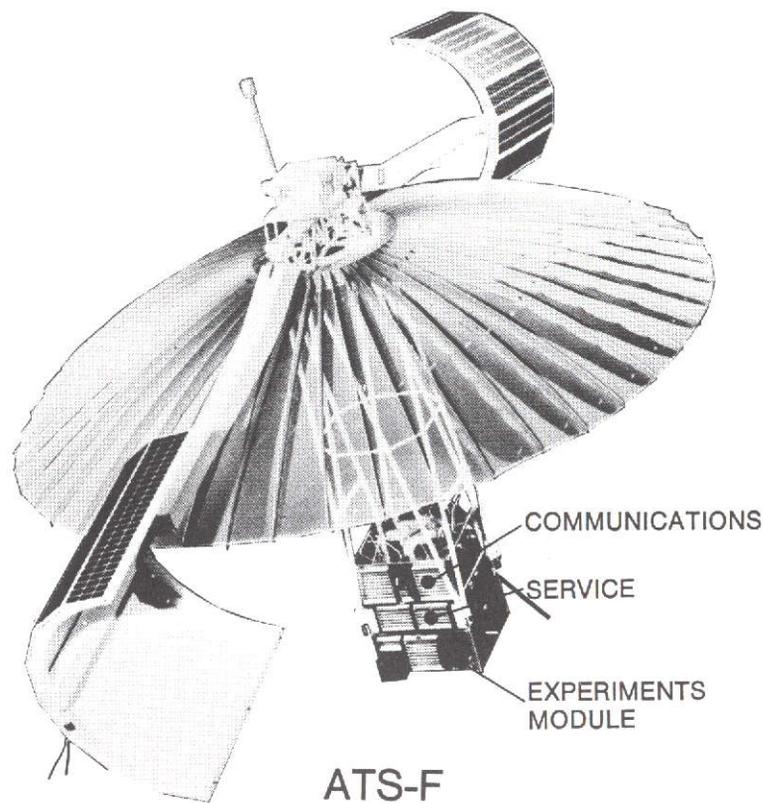
ATS-F

Figure 2-1. Deployed Configuration of ATS-F. The north face
of the Earth-Viewing Module is visible, showing
the location of one ion engine in the upper central
part of the Communications Module. The Polaris
star tracker shields are at the upper right and the
radiometer cooler cone housing is at the lower left
of the Experiments Module. Both the north and
south faces of the EVM include large areas of louv-
ered thermal radiators.

Laser Retroreflector. A laser retroreflector will be provided for accurate distance measurements.

Quartz Crystal Microbalance. This instrument will measure accretion of materials which may degrade equipment performance.

Advanced Thermal Control. A new approach to methods of stabilizing spacecraft temperatures will be demonstrated. This method is based upon varying the ratio of solar absorptance to infrared emittance of the spacecraft surface as follows:

Large areas of the surface are covered with thin quartz second-surface reflectors. Systems of polished aluminum louvers cover these to an extent determined by the temperature of bimetallic actuators. The surfaces radiate heat to the north or south sky when the louvers are open.

Accelerometer. Measurements will be made of the spacecraft vibration characteristics during the launch phase of the mission.

Radio Beacon. A radio beacon experiment at uhf and vhf bands will study the effects of ionospheric particles on radio propagation beyond the atmosphere from positions where the influence of the magnetosphere and solar wind environments can be easily interpreted.

Radio Frequency Interference. This experiment will measure the mutual interference between satellite and terrestrial communications systems for use in improved designs for future communications satellites.

Educational Television. ATS-F will beam educational television programming to low-cost receiving stations in or near schools or community buildings in isolated regions of Alaska and the Rocky Mountains where terrestrial TV converage is not feasible. The Department of Health, Education and Welfare, and the Corporation for Public Broadcasting are cooperating with the National Aeronautics and Space Administration in this venture.

Position Location and Aircraft Communications. Through accurate altitude and position measurements and continuous communications access with aircraft, the trans-Atlantic flight corriders may be reduced from 120 miles width with 15-minute spacing to 30 miles width with 5-minute spacing.

Tracking and Data Relay. By means of its steerable 30-foot antenna, the ATS-F satellite will maintain S-band communications with the low-orbiting NIMBUS satellite and will relay weather data when the acquiring satellite is out of receiving range of earth stations.

Instructional Television. Following one year in orbit, the
ATS-F satellite will be moved from 94° degrees west longitude
to 35° degrees east longitude. There it will transmit instruc-
tional programs from a ground station at Ahmedabad, India to a
network of some 3000 inexpensive community receivers.

Self-Adaptive Precision Pointing Spacecraft Attitude Control.
Active spacecraft control by a ground-based computer will be
demonstrated.

2.1.2 Cesium Ion Engine Locations

The earth viewing module of the ATS-F is basically a rectangular
structure of 137.2 x 137.2 centimeters cross section and 159 centimeters
tall (54 by 54 by 62.5 inches). In orbit, one square surface faces the
earth and the other faces the antenna; the four rectangular surfaces
face the four principal points of the compass. The location of one of
the two cesium thrusters is shown in the north face of the spacecraft
in Figure 2-2. Earthward direction is toward the bottom of the figure.
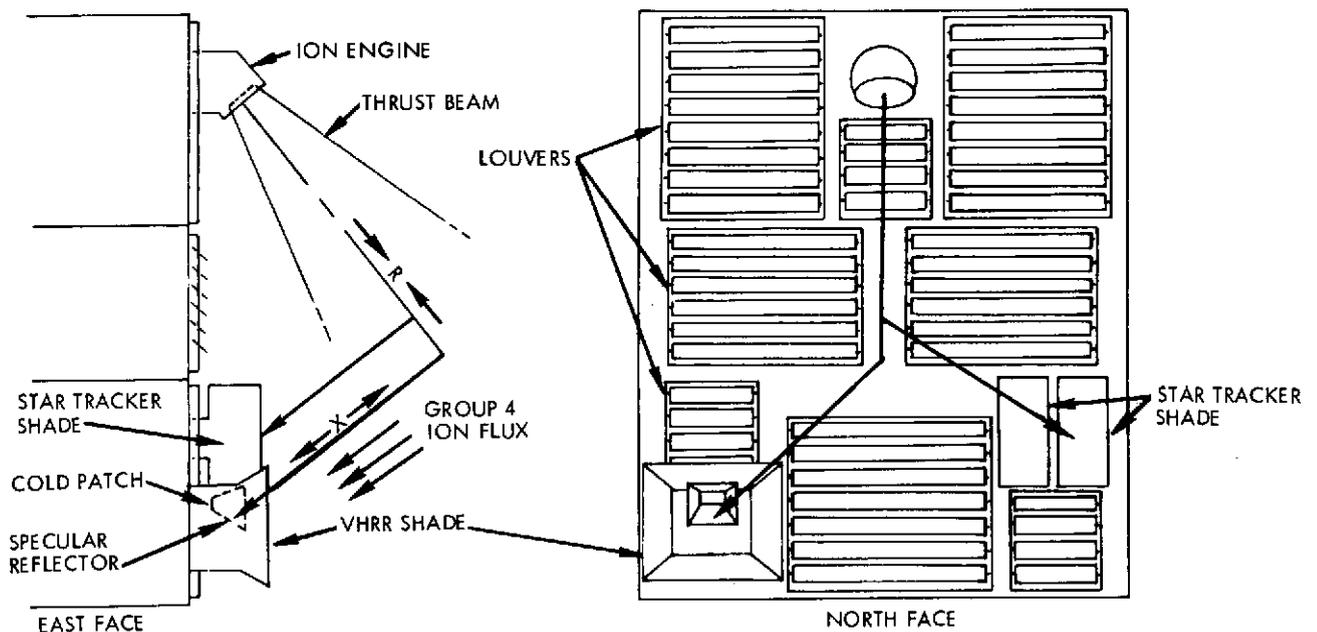
Figure 2-2. Sketch Showing Relative Locations of Three Sensitive
Surfaces of Concern in the Series II Ion Beam Tests

2-4

The other ion engine is similarly located on the south face. The accel grid of each ion engine is about 25.5 centimeters from the top of the spacecraft, and the engines will be mounted so that the angle between thrust beam axis and the adjacent spacecraft surface will be approximately 38 degrees. Figure 2-3 depicts the relative locations of ion engines and the the cylindrical solar arrays.

Of particular interest to this program are potential interactions between the cesium ion engine experiment and three of the ATS-F experiments in particular, as well as possible impact on other spacecraft subsystems in general. The three of particular interest are: (a) the combinations of aluminum louvers with optical solar reflectors (OSR's) which will be used for active temperature control of the earth viewing module, (b) the (Polaris) star tracker, and (c) the earth viewing radiometer. Of these, two have locations on the north face of the EVM only.

2.2 MATERIAL SAMPLES

During the course of this program, samples of many spacecraft structural materials and surface coatings have been made available for testing with propellant ions and atom beams. For internal accountability purposes these have been assigned to a master list which now extends from "(A)" to "(QQQ)". Identifying designations from this master list are shown in the sample lists given in several sections, below. Of approximately 70 items now in the master list, almost 30 were specifically provided by Goddard Space Flight Center from various activities relating to the ATS-F program for use in the Phase IV effort. Some of the samples shown in various lists below were tested in the interest of generality. A few will not, after all, be used on ATS-F; others are not expected to be exposed to ion engine effluents under normal circumstances.

Of principal importance were the following sample materials:

SOLAR ARRAY

PARABOLIC REFLECTOR

92°

92°

78°

78°

ION ENGINE

100 INCHES

ION ENGINE

EARTH
VIEWING
MODULE

37°

37°
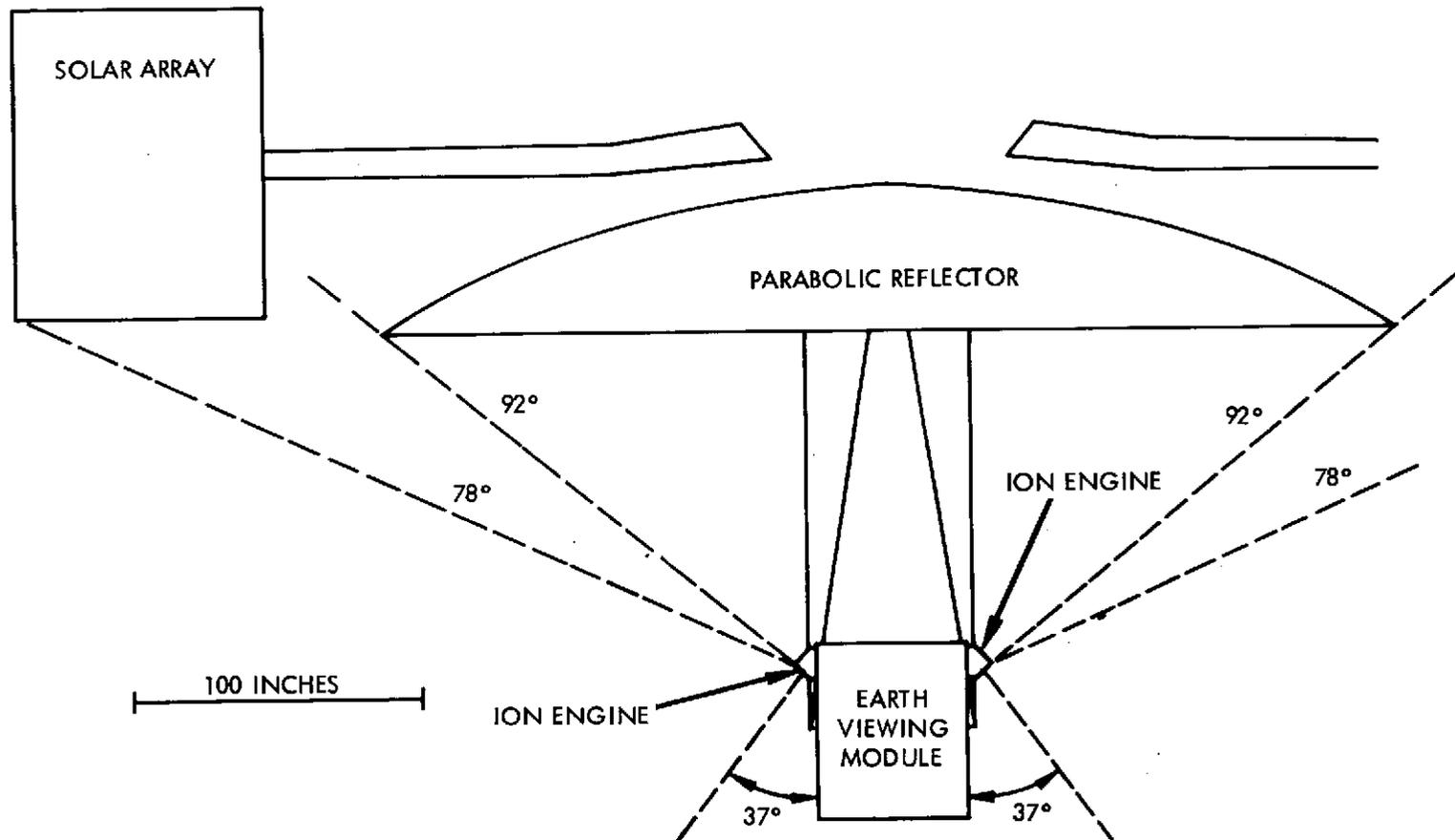
Figure 2-3. Diagram of ATS-F Spacecraft Showing Potential Interception of Ion Engine
Accelerator Grid Material or Charge-Exchange Ions on the (Curved) Solar Arrays

Sample	Material and Use on ATS-F	Section Where Test Reported
(A)	Polished Aluminum Thermal Control Louvers	4, 5
(G)	Aluminized Kapton Earth Viewing Module Thermal Blanket Surface	4, 5, 6
(KK)	Corning No. 7940 Quartz with Vapor-deposited Silver Under Vapor-deposited Inconel on Rear Surface Thermal control radiator	4, 5, 7, 8
(SS)	Vapor-deposited Aluminum on Carregen Nickel on Aluminum Base Radiometer cryogenic radiator	7, 8
(WW)	Antireflective Lens Coating Startracker lens	7
(AAA-1)	Solar Cell Panel Built for Test Using Same Materials as in ATS-F Solar Panel	7, 8
(MMM)	DC 92-007 Thermatrol White Paint Outer surfaces of radiometer cooler cone housing and startracker shade	4, 5, 7, 8

3. CESIUM ION SOURCE AND TESTING FACILITY

3.1 ION SOURCE

Experiments conducted on this program and reported in previous
volumes of the Final Report have emphasized mercury as the propellant
and have utilized a 15- or 20-centimeter diameter electron bombardment
electrostatic thruster. To provide ionic and atomic cesium beams required
in Phase IV, a 1-inch diameter porous tungsten type source has been
chosen.[12] Contact ionization type sources of this size have long been in
use at TRW. To obtain atomic beams, the potentials normally applied
to the source are removed.

The source has several attractive characteristics. It will conven-
iently operate over an acceleration potential range from a few volts to over
one thousand volts. The energy spectrum of the ions is very small and
the emitted neutral component is typically less than 1 percent of the
emitted ions. The maximum ion current density obtainable is dependent
upon ionizer quality, grid configuration and required grid life, but 5
ma/cm^2 is easily attainable in most instances and 1 ma/cm^2 is an
operating point commonly employed. For some experiments, much
lower ion current densities ($\sim 20 \mu a/cm^2$) were used.

One disadvantage of this type of ion source is that the fine accelerator
grid wires, positioned over the ionizer, intercept some of the ions and
erode by sputtering. This limits grid life and directs a small flux of
grid material (tungsten) at the sample area. The grids are replaceable
and, at the required current densities, lifetime was not expected to be
a serious problem. An evaluation of the contamination problem follows.

As with any other contaminant fluxes in these experiments, the
criteron for the maximum level tolerable is simply the level at which
the experimental results begin to be affected. In the present case
of a metallic contaminant flux in the ion beam, this flux must be low
enough so that foreign atoms are removed by sputtering as rapidly as
they arrive and without significantly protecting the sample itself from
sputtering or other forms of ion damage. Since the sputtering yield
of tungsten by Cs$^+$ is probably near unity (as it is for Xe$^+$, which

weighs ~2 percent more than cesium[3]), the permissible flux of W atoms is a few percent of the Cs^+ flux. The following analysis predicts the actual flux from the accelerator grid will be less than 1 percent, and hence quite tolerable.

The procedure is to wind 3-mil-diameter tungsten wire into a cross grid with 48 wires per inch in each direction. Such a grid has an optical transmission of ~75 percent. Its ion transmission, however, will be somewhat less than 75 percent because ions passing very near a (negatively biased) grid wire are attracted into it. Figure 3-1 illustrates three classes of ion trajectories terminating on the wire. One class consists of all of the ions which are emitted from the areas directly behind ("shadowed" by) the grid wire. They cause sputtering, but the grid atoms travel straight trajectories, and so intercept the ionizer, not the samples. Another class of ions emanate from outside the shadowed area but also terminate on the ionizer side of the wire. The third class, indicated by the heavily weighted curve, is the class of concern since grid atoms sputtered by these ions can reach the sample area. Note, however, how small an angle is subtended by the samples some 50 inches distant.

A knowledge of the magnitude of the third group would facilitate estimating the contaminant flux which arrives at the sample. It is known from past operation of these sources with various grid configurations that together the Class II and III ions are usually 50 percent of the Class I current; typically, the accelerator grid current is 50 percent greater than would be predicted on the basis of the optical density of the grid alone. Obviously, most of the extra current is Class II , but assume as a worst case that it is all Class III:

$$I_{g,T} = I_{g,I} + I_{g,III} = 1.5 \, G_d I_o \qquad (3-1)$$

where

G_d = optical density of grid

I_o = ion current emitted by source
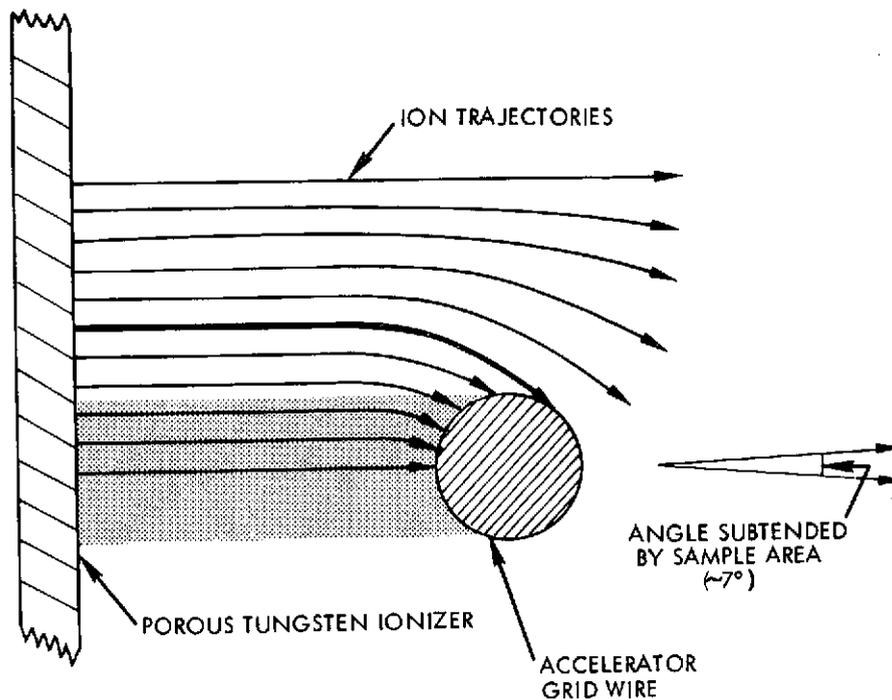
Figure 3-1. Diagram of Ion Trajectories in the Vicinity of Accelerator Grid Wires. Only trajectories of the class denoted by the heavy line contribute to contaminants in the ion beam.

The ion current in the beam, I_b, is then

$$I_b = I_o (1-1.5\ G_d)\qquad\qquad(3-2)$$

For simplicity, the flux of tungsten atoms sputtered into the downstream hemisphere is expressed as an equivalent current I_w, where

$$I_w = SI_{g,III}\qquad\qquad(3-3)$$

where

$\quad$ S = ion sputtering yield

and

$$\frac{I_w}{I_b} = \frac{0.5\ S\ G_d}{1-1.5\ G_d}\qquad\qquad(3-4)$$

3-3

It is now observed that the sputtered tungsten atom flux density will dilute much more rapidly than does the ion beam flux density. A simple conical expansion model of the ion beam leads to a current density dilution of $\sim 10^{-2}$. On the other hand, the flux of sputtered tungsten atoms has a cosine distribution and therefore dilutes as the square of the distance from the source, which is $\sim 10^{-4}$ at the sample plane. Thus, at the sample plane

$$\frac{J_w}{J_b} = \frac{0.5 \, S \, G_d}{1 - 1.5 \, G_d} \cdot \frac{10^{-4}}{10^{-2}} \qquad (3-5)$$

where J denotes current density

As discussed previously, $S \approx 1$ and $G_d = 0.25$ for the grid planned. Hence,

$$\frac{J_w}{J_b} = 2 \times 10^{-3} \qquad (3-6)$$

A tungsten atom flux which is 0.2 percent the ion flux is certainly acceptable. Furthermore, this estimate is based on worst case assumptions and the actual value will be even smaller.

Figures 3-2 and 3-3 show the 1-inch-diameter porous tungsten ionizer, adjustable 3-mil tungsten wire accelerator grid, and a tungsten wire neutralizer. Figure 3-4 shows the atmosphere side of the port plate. The grid spacing adjustment mechanism is above. At the center · is the water-cooled ionizer mounting fixture, which is insulated from ground by a Teflon gasket. Cesium vapor is supplied to the ionizer by crushing a glass ampoule within the tubular copper boiler, and passing current through the electrical heater. During operation the boiler and associated vapor feed tube are heat-insulated with glass wool.

Since the water-cooled ionizer mounting fixture is at source potential (550 volts) and microamp ion beam currents will be used, current leakage through the water supply is a potential source of error in ion beam current measurements. Therefore, a closed-loop system using deionized water and high voltage drop tubes was installed.
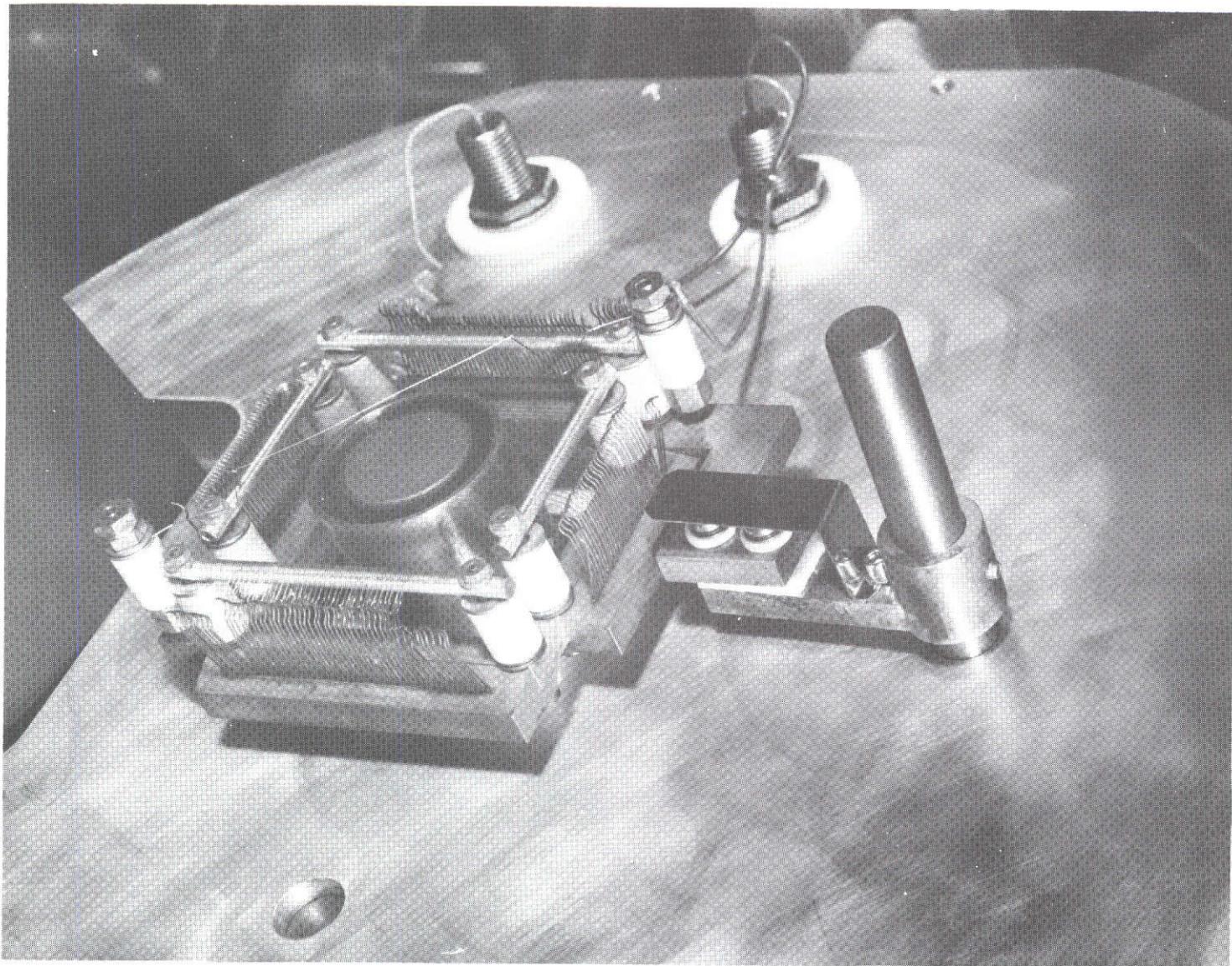
Figure 3-2. Photograph of Cesium Beam Source. One-inch-diameter porous tungsten ionizer is surrounded by heat shield. Diagonal W wire is neutralizer.
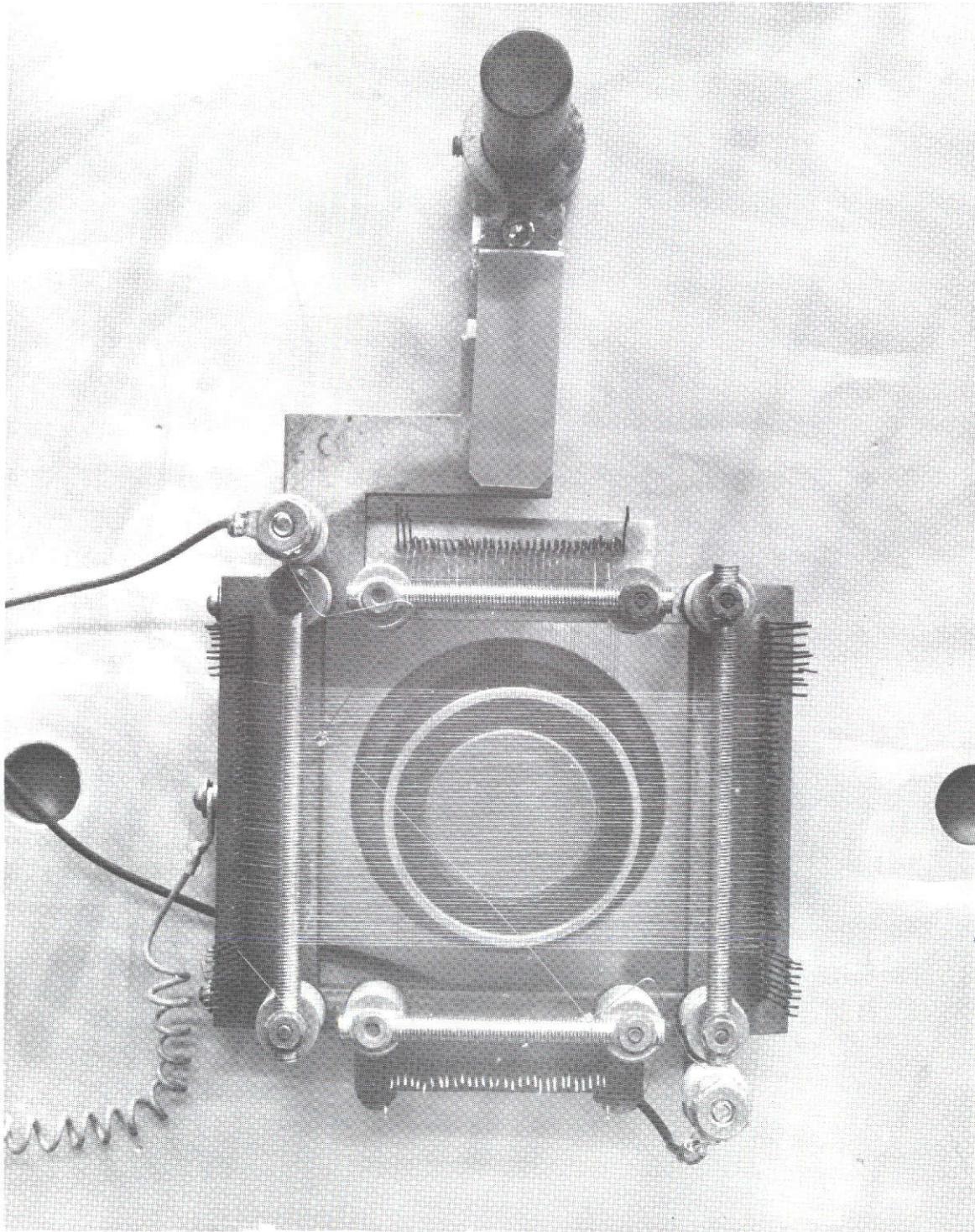
Figure 3-3. Head-On View of Beam Source with Adjustable
3-Mil W Wire Accel Grid Highlighted
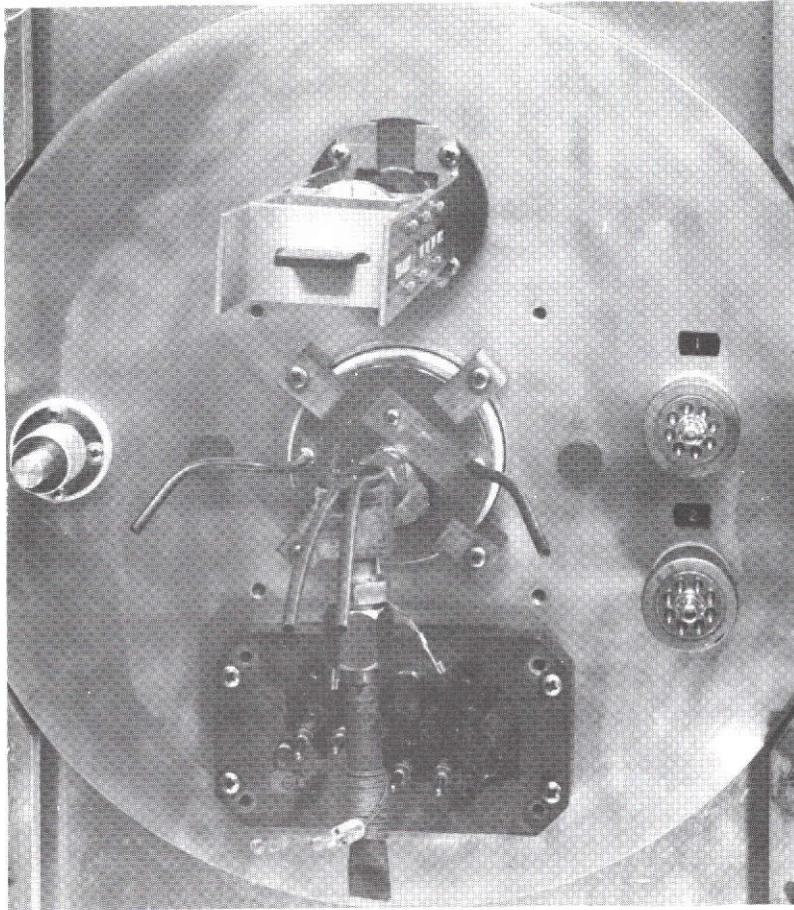
Figure 3-4. Atmosphere Side of Beam Source. Grid adjusting mechanism and electrically heated cesium boiler are visible.

Thirty 5-gram cesium ampoules were purchased from MSA Research Corporation of Evans City, Pennsylvania. The ampoules were prepared from their Lot D-446-929-6, which is the same lot used for Electro Optical Systems cesium order of September 1970. (EOS is the contractor supplying the Ion Engine Experiment hardware.)

Generally the cesium ion source operates most uniformly at a current density yielding 10^{10} to 10^{12} ions per square centimeter per second at the surface of the test samples. The beam is neutralized by means of a 0.005-inch-diameter tungsten filament immersed in the plasma. Two other neutralizers are located further downstream to insure complete neutralization of the beam.

3.2 EXPERIMENTAL FACILITIES

Experiments reported in this volume were conducted in one or the other of two facilities. The first is the Spacecraft Surface Contamination Experimental Facility described in Volume I and in Appendix A of Volume II. The second is a special cesium vapor exposure facility which is described in Section 6 of this volume. The thermophysics instrumentation described in Appendix B of Volume II was also used, and augmented as described in the relevant sections of this volume. Ion beam density is monitored in the principal facility as described below.

Ion Beam Density Monitors

The total ion beam current is best measured by the current delivered by the 550-volt supply to the ion source. Total neutralizer emission current should also be almost identical to this value to assure a neutralized plasma and minimize charging of insulator surfaces.

Beam uniformity is checked by a J_+ probe which can be moved across the beam at a position 27 inches downstream from the source. In general, a uniform beam is obtained by adjusting the accelerator grid to ion source spacing to approximately space charge limited flow.

Dose rate is calculated from the average reading of five J_+ probes, each with a 1/4-inch-diameter entrance aperture, mounted on a flapper shutter which can be placed in the beam at a distance of 45 inches downstream. Four of the probes form a 3.5-inch square; the fifth is located at the center of the square and along the center axis of the ion beam. This probe assembly is shown in Figure 7-9 (Section 7).

When the samples are positioned to intercept the beam their distance downstream from the source is 49.5 inches. Thus, if I_j represents the average of the 5 J_+ probes, the ion current density at the sample plate is $2.61 \, I_j$ amps/cm^2 or 1.63×10^{10} ions per cm^2 per second per nanoampere I_j.

4. CESIUM ION EFFECTS ON THERMOPHYSICAL PROPERTIES

4.1 INTRODUCTION

This section will discuss the cesium ion tests completed during January and February, 1972. Tests on various materials were performed at +220°, +120°, +32°, and -60°F. The tests to be discussed in this section are shown in Table 4-1.

Table 4-1. Cesium Ion/Thermal Coating Test Matrix

Material	Cesium Ion Energy	Sample Temperature	Table No.	Figure No.
(R) Z93 White Paint	550 ev	-60°F	4-3	4-2
	550 ev	220°F		
(NN) DC 92 007 Therma-trol White Paint	550 ev	-60°F	4-5	4-4
	550 ev	220°F		
	31 ev	32°F	—	4-10
	31 ev	120°F		
(G) Kapton, Aluminized Rear Surface	550 ev	-60°F	4-2	4-1
	550 ev	+220°F		
(A) "Polished" Aluminum (VDA?)	550 ev	-60°F	4-6	4-5
	550 ev	+220°F		
(--) GSFC MS74 White Paint	550 ev	-60°F	4-4	4-3
	550 ev	+220°F		
(MM) Silvered Teflon FEP	31 ev	32°F	4-8	4-7
	31 ev	120°F		
(KK) "OSR" Second Surface Mirrors	31 ev	32°F	4-9	4-8
	31 ev	120°F		
(--) $Al_2O_3/SiO_2/VDA$	31 ev	32°F	4-10	4-9
	31 ev	120°F		
(PPP) 3M 401 C 10 Velvet Black Paint	31 ev	32°F	4-7	4-6
	31 ev	120°F		

4.2 RESULTS

Tables 4-2 through 4-10 give complete data tabulations for each
sample reported herein. The xenon absorptance data have been plotted in
Figures 4-1 through 4-5 for the 550 ev Cs^+ exposures and Figures 4-6
through 4-10 for the 31 ev Cs^+ exposures. Occasional small discrep-
ancies between plotted and tabulated ion doses occur because the data
were originally plotted before refined values of doses were available.
Whenever the shape of the curve would be affected, the refined values
have been used.

4.3 DISCUSSION

The effects of cesium ions show small, if any, degradation to the
thermal coatings tested for total ion doses below 10^{15} ion/cm^2. At this
point in exposure, some changes begin to occur for several of the
coatings.

Kapton aluminized on the rear surface shows degradation beginning
to occur at an ion dose of 10^{15} ions/cm^2 (Figure 4-1). Degradation rate
increased significantly at higher temperature. It should be noted that the
ion arrival rate was increased approximately a factor of 10 for all tests
for the last one or two data points (Tables 4-2 through 4-10). The pur-
pose of this procedure was to obtain very large doses within reasonable
time periods. Similar tests previously conducted with mercury ions in
which ion arrival rate was varied showed relatively little sensitivity to
ion arrival rate[3]. Most of the tests were terminated by ion source accel-
erator grid failure.

In contrast to Kapton, Z93 showed increase in degradation for the
-60°F test case for ion doses of 10^{16} ions/cm^2 (Figure 4-2). This in-
creasing degradation at low temperatures is consistent with previous
tests on Z93 using mercury ions[3]. The DC 92-007 white paint showed a
very slight amount of degradation at all but the lowest temperature
(-60°F) where none at all was seen (Figure 4-4). There may be enough
of a trend to establish increasing degradation with increasing tempera-
ture, but the amount of degradation in all cases was small. MS 74 inor-
ganic white paint also exhibited greater degradation at 220°F than at
-60°F (Figure 4-3).

Table 4-2. Degradation of Second Surface Aluminized
Kapton Due to Cesium Ion Impingement

Date	Sample Temp. (°F)	Beam Energy (Kev)	Beam Flux (ions/cm²/sec)	Total Exp. Time (Hrs)	Dose (ions/cm²)	α_x	ε_H	Meas. Delay* (Hrs.)
12-23-71	62	0.55			0	.35	.82	0
12-27-71	214	"			"	.36	.81	0
"	"	"	$\sim4 \times 10^{10}$	0.01	1.3×10^{12}	.33	.80	1.8
12-28-71	"	"	$\sim5 \times 10^{10}$	0.11	2.4×10^{13}	.34	.79	0.8
"	213	"	"	1.11	2.3×10^{14}	.34	.80	0.7
12-29-71	"	"	"	16.1	2.9×10^{15}	.39	.82	0.8
"	"	"	"	16.1	2.9×10^{15}	.38	.80	1.5
12-30-71	214	"	"	43.1	7.3×10^{15}	.40	.79	0.8
"	212	"	"	43.1	7.3×10^{15}	.41	.81	1.8
1-3-72	232	"	"	123.9	2.1×10^{16}	.47	.78	0.7
"	233	"	"	123.9	2.1×10^{16}	.46	.79	6.7
1-4-72	235	"	9×10^{11}	124.5	2.7×10^{16}	.47	.79	11.7
"	64	"	"	124.5	2.7×10^{16}	.49	.78	
1-10-72	61	0.55	$\sim6 \times 10^{10}$	0		.35	.79	0
1-11-72	-60	"	"	0	0	.32	.79	0
"	"	"	"	0	0	.34	.81	0
"	"	"	"	0.01	2.2×10^{12}	.34	.81	0.8
"	-61	"	"	0.11	2.3×10^{13}	.37	.89	0.8
1-12-72	-57	"	"	0.11	2.3×10^{13}	.36	.87	22.
"	-58	"	"	1.11	2.3×10^{14}	.32	.83	0.8
1-13-72	-60	"	"	14.0	2.9×10^{15}	.34	.89	
1-17-72	+58	"	"	14.0	2.9×10^{15}	.35	.83	
1-18-72	-61	"	"	14.0	2.9×10^{15}	.51	1.02	
1-19-72	-54	"	"	14.0	2.9×10^{15}	.36	.82	
1-21-72	-58	"	"	58.0	1.2×10^{16}	.37	1.02	3.
1-24-72	-66	"	"	121.0	2.5×10^{16}	.44	.94	6.
1-25-72	-60	"	$\sim7 \times 10^{11}$	138.0	7.0×10^{16}	.29	.96	4.

*Time between end of exposure and measurement.

Date	Sample Temp. (°F)	Beam Energy (Kev)	Beam Flux (ions/cm²/sec)	Total Exp. Time (Hrs)	Dose (ions/cm²)	α_x	ε_H	Meas. Delay* (Hrs.)
12-23-71	62	0.55				.12	.86	0
12-27-71	214	"				.12	.85	0
"	"	"	$\sim 4 \times 10^{10}$	0.01	1.3×10^{12}	.10	.85	1.8
12-28-71	"	"	$\sim 5 \times 10^{10}$	0.11	2.4×10^{13}	.11	.84	0.8
"	213	"	"	1.11	2.3×10^{14}	.11	.85	0.7
12-29-71	"	"	"	16.1	2.9×10^{15}	.14	.87	0.8
12-30-71	"	"	"	43.1	7.3×10^{15}	.12	.84	0.8
"	212	"	"	43.1	7.3×10^{15}	.12	.86	1.8
1-3-72	232	"	"	123.9	2.1×10^{16}	.13	.84	0.7
"	233	"	"	123.9	2.1×10^{16}	.13	.84	6.7
1-4-72	234	"	$\sim 9 \times 10^{11}$	124.5	2.7×10^{16}	.12	.84	11.7
"	63	"	"	"	2.7×10^{16}	.11	.85	
1-10-72	60	0.55	$\sim 6 \times 10^{10}$	0	0	.14	.89	0
1-11-72	-60	"	"	"	"	.12	.85	0
"	"	"	"	0.1	2.2×10^{12}	.11	.86	0.8
"	-61	"	"	0.11	2.3×10^{13}	.15	.91	0.8
1-12-72	-57	"	"	0.11	2.3×10^{13}	.14	.89	22.
"	-58	"	"	1.11	2.3×10^{14}	.08	.84	0.8
1-13-72	-61	"	"	14.0	2.9×10^{15}	.11	.92	
1-17-72	+58	"	"	14.0	2.9×10^{15}	.13	.91	
1-18-72	-62	"	"	14.0	2.9×10^{15}	.1350	.95	
1-21-72	-58	"	"	58.0	1.2×10^{16}	.16	1.04	3.
1-24-72	-65	"	"	121.0	2.5×10^{16}	.18	1.01	6.
1-25-72	-59	"	$\sim 7 \times 10^{11}$	138.0	7.0×10^{16}	.22	1.12	4.

*Time between end of exposure and measurement.

Table 4-4. Degradation of MS74 (GSFC) White Paint Due to Cesium Ion Impingement

Date	Sample Temp. (°F)	Beam Energy (Kev)	Beam Flux (ions/cm²/sec)	Total Exp. Time (Hrs)	Dose (ions/cm²)	α_x	ε_H	Meas. Delay* (Hrs.)
12-23-71	62	0.55				.16	.89	0
12-27-71	211	"				.15	.88	0
"	"	"	"	0.01	1.3×10^{12}	.14	.88	1.8
12-28-71	"	"	"	0.11	2.4×10^{13}	.14	.87	0.8
"	210	"	"	1.11	2.3×10^{14}	.15	.89	0.7
12-29-71	"	"	"	1.1	2.9×10^{15}	.15	.88	0.8
12-30-71	"	"	"	43.1	7.3×10^{15}	.17	.88	0.8
1-3-72	229	"	"	123.9	2.1×10^{16}	.18	.87	0.7
"	230	"	"	123.9	2.1×10^{16}	.17	.88	6.7
1-4-72	"	"	$\sim 9 \times 10^{11}$	124.5	2.7×10^{16}	.19	.87	11.7
"	64	"	"	124.5	2.7×10^{16}	.17	.88	
1-10-72	60	0.55	$\sim 6 \times 10^{10}$	0	0	.16	.90	0
1-11-72	-61	"	"	"	"	.14	.86	0
"	-60	"	"	0.01	2.2×10^{12}	.15	.87	0.8
"	-61	"	"	0.11	2.3×10^{13}	.16	.87	0.8
1-12-72	-57	"	"	1.11	2.3×10^{14}	.12	.84	0.8
1-13-72	-60	"	"	14.0	2.9×10^{15}	.15	.86	
1-17-72	+58	"	"	14.0	2.9×10^{15}	.16	.90	
1-18-72	-62	"	"	14.0	2.9×10^{15}	.15	.98	
1-21-72	-59	"	"	58.0	1.2×10^{16}	.16	.88	3.
1-24-72	-65	"	"	121.0	2.5×10^{16}	.17	.87	6.
1-25-72	-60	"	$\sim 7 \times 10^{11}$	138.0	7.0×10^{16}	.15	.84	4.

* Time between end of exposure and measurement.

Table 4-5. Degradation of DC92-007 White Paint Due to Cesium Ion Impingement

Date	Sample Temp. (°F)	Beam Energy (Kev)	Beam Flux (ions/cm²/sec)	Total Exp. Time (Hrs)	Dose (ions/cm²)	α_s	ϵ_H	Meas. Delay* (Hrs.)
12-23-71	63	0.55				.18	.81	0
12-27-71	215	"				.16	.80	0
"	"	"	$\sim 4 \times 10^{10}$	0.01	1.3×10^{12}	.17	.80	1.8
12-28-71	214	"	$\sim 5 \times 10^{10}$	0.11	2.4×10^{13}	.16	.80	0.8
"	"	"	"	1.11	2.3×10^{14}	.19	.81	0.7
12-29-71	"	"	"	16.1	2.9×10^{15}	.18	.80	0.8
12-30-71	213	"	"	43.1	7.3×10^{15}	.17	.80	0.8
"	"	"	"	43.1	7.3×10^{15}	.18	.80	1.8
1-3-72	232	"	"	123.9	2.1×10^{16}	.19	.78	0.7
"	234	"	"	"	2.1×10^{16}	.19	.78	6.7
1-4-72	"	"	1×10^{12}	124.5	2.7×10^{16}	.18	.77	11.7
"	64	"	"	"	2.7×10^{16}	.18	.78	
1-10-72	61	0.55	$\sim 6 \times 10^{10}$	0	0	.15	.84	0
1-11-72	-60	"	"	"	"	.16	.83	0
"	-59	"	"	0.01	2.2×10^{12}	.16	.82	0.8
"	-61	"	"	0.11	2.3×10^{13}	.21	.82	0.8
1-12-72	-57	"	"	0.11	2.3×10^{13}	.13	.80	22.
"	-57	"	"	1.11	2.3×10^{14}	.16	.82	0.8
1-13-72	-60	"	"	14.0	2.9×10^{15}	.18	.82	
1-17-72	+59	"	"	14.0	2.9×10^{15}	.15	.84	
1-18-72	-61	"	"	14.0	2.9×10^{15}	.17	.83	
1-21-72	-58	"	"	58.0	1.2×10^{16}	.19	.85	3.
1-24-72	-64	"	"	121.0	2.5×10^{16}	.12	.80	6.
1-25-72	-60	"	$\sim 7 \times 10^{11}$	138.0	7.0×10^{16}	.16	.80	4.

*Time between end of exposure and measurement.

Table 4-5. Degradation of DC 92-007 White Paint
Due to Cesium Ion Impingement (Continued)

Date	Sample Temp. (°F)	Beam Energy (Kev)	Beam Flux (ions/cm²/sec)	Total Exp. Time (Hrs.)	Dose (ions/cm²)	α_x	ε_H	Meas. Delay* (Hrs.)
2-1-72	59	.550	$\sim 6 \times 10^{10}$	0	0	.16	.84	0
2-2-72	121	"	"	"	0	.16	.85	0
"	"	"	"	0.01	2.6×10^{12}	.16	.85	0.8
"	"	"	"	0.11	2.6×10^{13}	.16	.85	0.6
"	"	"	"	1.11	2.6×10^{14}	.16	.85	0.6
2-3-72	122	"	"	14.2	3.0×10^{15}	.16	.85	1.
2-4-72	"	.031	"	28.8	5.9×10^{15}	.16	.85	1.5
2-7-72	121	"	"	93.8	2.1×10^{16}	.15	.85	1.
2-9-72	128	"	$\sim 6 \times 10^{11}$	127.0	9.8×10^{16}	.17	.86	4.5
2-10-72	60					.18	.85	14.
2-14-72	26	.032	$\sim 6 \times 10^{10}$	0	0	.16	.82	0
2-15-72	21	"	"	"	0	.17	.83	0
2-17-72	30	"	"	0.1	2.3×10^{13}	.16	.85	2.
"	"	"	"	1.1	2.1×10^{14}	.16	.84	1.3
2-18-72	28	"	"	17.1	3.8×10^{15}	.17	.84	1.2
2-22-72	30	"	"	100.1	2.1×10^{16}	.19	.84	7.
2-23-72	29	"	$\sim 8 \times 10^{11}$	114.9	6.1×10^{16}	.19	.83	2.
"	59	"	"		6.1×10^{17}	.19	.84	7.3

*Time between end of exposure and measurement.

Table 4-6. Degradation of Polished Aluminum (VDA?)
Due to Cesium Ion Impingement

Date	Sample Temp. (°F)	Beam Energy (Kev)	Beam Flux (ions/cm²/sec)	Total Exp. Time (Hrs.)	Dose (ions/cm²)	α_x	ε_H	Meas. Delay * (Hrs.)
12-23-72	63	0.55				.17	.06	0
12-27-71	217	"				.12	.04	0
"	"	"	$\sim 4 \times 10^{10}$	0.01	1.3×10^{12}	.12	.04	1.8
12-28-71	216	"	$\sim 5 \times 10^{10}$	0.11	2.4×10^{13}	.15	.04	0.8
"	215	"	"	1.11	2.3×10^{14}	.25	.04	0.7
12-29-71	"	"	"	16.1	2.9×10^{15}	.16	.04	0.8
12-30-71	214	"	"	43.1	7.3×10^{15}	.15	.04	0.8
1-3-72	234	"	"	123.9	2.1×10^{16}	.21	.04	0.7
"	236	"	"	123.9	2.1×10^{16}	.10	.04	6.7
1-4-72	"	"	$\sim 9 \times 10^{11}$	124.5	2.7×10^{16}	.14	.04	11.7
"	64	"	"	124.5	2.7×10^{16}	.12	.03	
1-10-72	62	0.55	$\sim 6 \times 10^{10}$	0	0	.15	.05	0
1-11-72	-59	"	"	"	"	.20	.12	0
"	"	"	"	0.01	2.2×10^{12}	.17	.10	0.8
"	-60	"	"	0.11	2.3×10^{13}	.23	.14	0.8
1-12-72	-57	"	"	1.11	2.3×10^{14}	.16	.11	0.8
1-13-72	-59	"	"	14.0	2.9×10^{15}	.10	.12	
1-17-72	+60	"	"	14.0	0.2×11^{17}	.14	.07	
1-18-72	-61	"	"	14.0	0.2×11^{17}	.14	.16	
1-21-72	-57	"	"	58.0	1.2×10^{16}	.21	.17	3.
1-24-72	-64	"	"	121.0	2.5×10^{16}	.14	.15	6.
1-25-72	-60	"	7×10^{11}	138.0	7.0×10^{16}	.30	.25	4.

* Time between end of exposure and measurement.

Table 4-7. Degradation of 3M 401-C-10 Black Velvet Paint Due to Cesium Ion Impingement

Date	Sample Temp. (°F)	Beam Energy (Kev)	Beam Flux (ions/cm²/sec)	Total Exp. Time (Hrs.)	Dose (ions/cm²)	α_x	ε_H	Meas. Delay* (Hrs.)
2-1-72	59	.550	$\sim 6 \times 10^{10}$	0	0	.84	.88	0
"	60	"	"	"	0	.95	.91	0
2-2-72	122	"	"	"	0	.93	.89	0
"	"	"	"	0.01	2.6×10^{12}	.95	.89	0.8
"	"	"	"	0.11	2.6×10^{13}	.94	.89	0.6
"	"	"	"	1.11	2.6×10^{14}	.95	.89	0.6
2-3-72	123	"	"	14.2	3.0×10^{15}	.94	.88	1.
2-4-72	122	.031	"	28.8	5.9×10^{15}	.93	.88	1.5
2-7-72	121	"	"	93.8	2.1×10^{16}	.92	.90	1.
"	"	"	"	93.8	2.1×10^{16}	.91	.90	2.
2-9-72	128	"	$\sim 6 \times 10^{11}$	127.0	9.8×10^{16}	.96	.93	4.5
"	"	"	"		9.8×10^{16}	.87	.89	5.5
2-10-72	59					.93	.94	14.
"	"	"				.91	.95	15.
2-14-72	26	.032	$\sim 6 \times 10^{10}$	0	0	.98	.95	0
2-15-72	21	"	"	"	0	1.05	.89	0
2-16-72	29	"	"	"	0	.93	.92	0
"	"	"	"	"	0	.94	.92	0
"	"	"	"	"	0	.86	.92	0
"	"	"	"	"	0	.90	.91	0
2-17-72	"	"	"	0.1	2.3×10^{13}	.97	.94	2.
"	"	"	"	1.1	2.1×10^{14}	.92	.92	1.3
2-18-72	27	"	"	19.1	3.8×10^{15}	1.16	1.04	1.2
2-22-72	28	"	"	100.1	2.1×10^{16}	.93	1.00	7.
2-23-72	"	"	$\sim 8 \times 10^{11}$	114.9	6.1×10^{16}	1.09	.98	2.
"	58	"	"		6.1×10^{17}	.94	.94	7.3

*Time between end of exposure and measurement.

Table 4-8. Degradation of Second Surface Silvered Teflon FEP
Due to Cesium Ion Impingement

Date	Sample Temp. (°F)	Beam Energy (Kev)	Beam Flux (ions/cm²/sec)	Total Exp. Time (Hrs.)	Dose (ions/cm²)	α_x	ε_H	Meas. Delay (Hrs.)
2-1-72	59	.550	$\sim 6\times10^{10}$	0	0	.07	.79	0
2-2-72	121	"	"	"	$\cap$	.09	.81	0
"	"	"	"	0.01	2.6×10^{12}	.09	.81	0.8
"	122	"	"	0.11	2.6×10^{13}	.09	.81	0.6
"	121	"	"	1.11	2.6×10^{14}	.09	.81	0.6
2-3-72	123	"	"	14.2	3.0×10^{15}	.09	.80	1.
2-4-72	122	.031	"	28.8	5.9×10^{15}	.09	.81	1.5
2-7-72	121	"	"	93.8	2.1×10^{16}	.10	.82	1.
"	"	"	"	11.0	2.1×10^{16}	.12	.82	2.
2-9-72	129	"	$\sim 6\times10^{11}$	127.0	9.8×10^{16}	.20	.83	4.5
"	"	"	"	"	"	.18	.83	5.5
2-10-72	60					.18	.84	14.
2-14-72	27	.032	$\sim 6\times10^{10}$	0	0	.08	.86	0
2-15-72	22	"	"	"	0	.08	.87	0
2-16-72	30	"	"	"	0	.09	.92	0
"	"	"	"	"	0	.08	.89	0
"	"	"	"	"	0	.09	.89	0
"	"	"	"	"	0	.09	.89	0
2-17-72	31	"	"	0.1	2.3×10^{13}	.09	.92	2.
"	"	"	"	1.1	2.1×10^{14}	.08	.90	1.3
2-18-72	30	"	"	19.1	3.8×10^{15}	.09	.88	1.2
2-22-72	"	"	"	100.1	2.1×10^{16}	.12	.94	7.
2-23-72	29	"	$\sim 8\times10^{11}$	114.9	6.1×10^{16}	.15	.87	2.
"	59	"	"		6.1×10^{17}	.15	.88	7.3

*Time between end of exposure and measurement.

Table 4-9.   Degradation of 7940 Quartz Second Surface Silvered OSR Due to Cesium Ion Impingement

Date	Sample Temp. (°F)	Beam Energy (Kev)	Beam Flux (ions/cm²/sec)	Total Exp. Time (Hrs.)	Dose (ions/cm²)	α_x	ϵ_H	Meas. Delay* (Hrs.)
2-1-72	59	.550	$\sim 6 \times 10^{10}$	0	0	.07	.76	0
2-2-72	122	"	"	"	0	.07	.77	0
"	"	"	"	0.01	2.6×10^{12}	.07	.76	0.8
"	"	"	"	0.11	2.6×10^{13}	.07	.76	0.6
"	"	"	"	1.11	2.6×10^{14}	.07	.76	0.6
2-3-72	"	"	"	14.2	3.0×10^{15}	.07	.76	1.
2-4-72	"	.031	"	28.8	5.9×10^{15}	.07	.76	1.5
2-7-72	121	"	"	93.8	2.1×10^{16}	.07	.77	1.
2-9-72	128	"	$\sim 6 \times 10^{11}$	127.0	9.8×10^{16}	.07	.78	4.5
2-10-72	60					.08	.80	14.
"	"					.07	.78	15.
2-14-72	28	.032	$\sim 6 \times 10^{10}$	0	0	.05	.72	0
2-15-72	21	"	"	"	0	.07	.79	0
2-17-72	30	"	"	0.1	2.3×10^{13}	.07	.81	2.
"	"	"	"	1.1	2.1×10^{14}	.06	.80	1.3
2-18-72	29	"	"	19.1	3.8×10^{15}	.06	.79	1.2
2-22-72	"	"	"	100.1	2.1×10^{16}	.07	.79	7.
2-23-72	"	"	$\sim 8 \times 10^{11}$	114.9	6.1×10^{16}	.07	.78	2.
"	58	"	"		6.1×10^{17}	.07	.78	7.3

*Time between end of exposure and measurement.

Table 4-10. Degradation of $Al_2O_3/SiO_2/VDA/$Buffed Aluminum Due to Cesium Ion Impingement

Date	Sample Temp. (°F)	Beam Energy (Kev)	Beam Flux (ions/cm²/sec)	Total Exp. Time (Hrs.)	Dose (ions/cm²)	α_x	ϵ_H	Meas. Delay* (Hrs.)
2-1-72	60	.550	$\sim6\times10^{10}$	0	0	.16	.68	0
2-2-72	122	"	"	"	0	.16	.66	0
"	"	"	"	0.01	2.6×10^{12}	.16	.67	0.8
"	123	"	"	0.11	2.6×10^{13}	.16	.67	0.6
"	"	"	"	1.11	2.6×10^{14}	.16	.66	0.6
2-3-72	"	"	"	14.2	3.0×10^{15}	.16	.66	1.
2-4-72	"	.031	"	28.8	5.9×10^{15}	.16	.66	1.5
2-7-72	121	"	"	93.8	2.1×10^{16}	.16	.66	1.
2-9-72	129	"	$\sim6\times10^{11}$	127.0	9.8×10^{16}	.16	.67	4.5
2-10-72	60					.15	.69	14.
2-14-72	26	.032	$\sim6\times10^{10}$	0	0	.14	.61	0
2-15-72	22	"	"	"	0	.16	.66	0
2-17-72	31	"	"	0.1	2.3×10^{13}	.15	.65	2.
"	"	"	"	1.1	2.1×10^{14}	.15	.65	1.3
2-18-72	29	"	"	19.1	3.8×10^{15}	.15	.64	1.2
2-22-72	"	"	"	100.1	2.1×10^{16}	.15	.65	7.
2-23-72	"	"	$\sim8\times10^{11}$	114.9	6.1×10^{16}	.16	.66	2.
"	59	"	"	"	5.6×11^{17}	.15	.64	7.3

*Time between end of exposure and measurement.

Figure 4-1. Kapton Xenon Absorptance Degradation at +100°C and -50°C by Energetic Cesium Ions
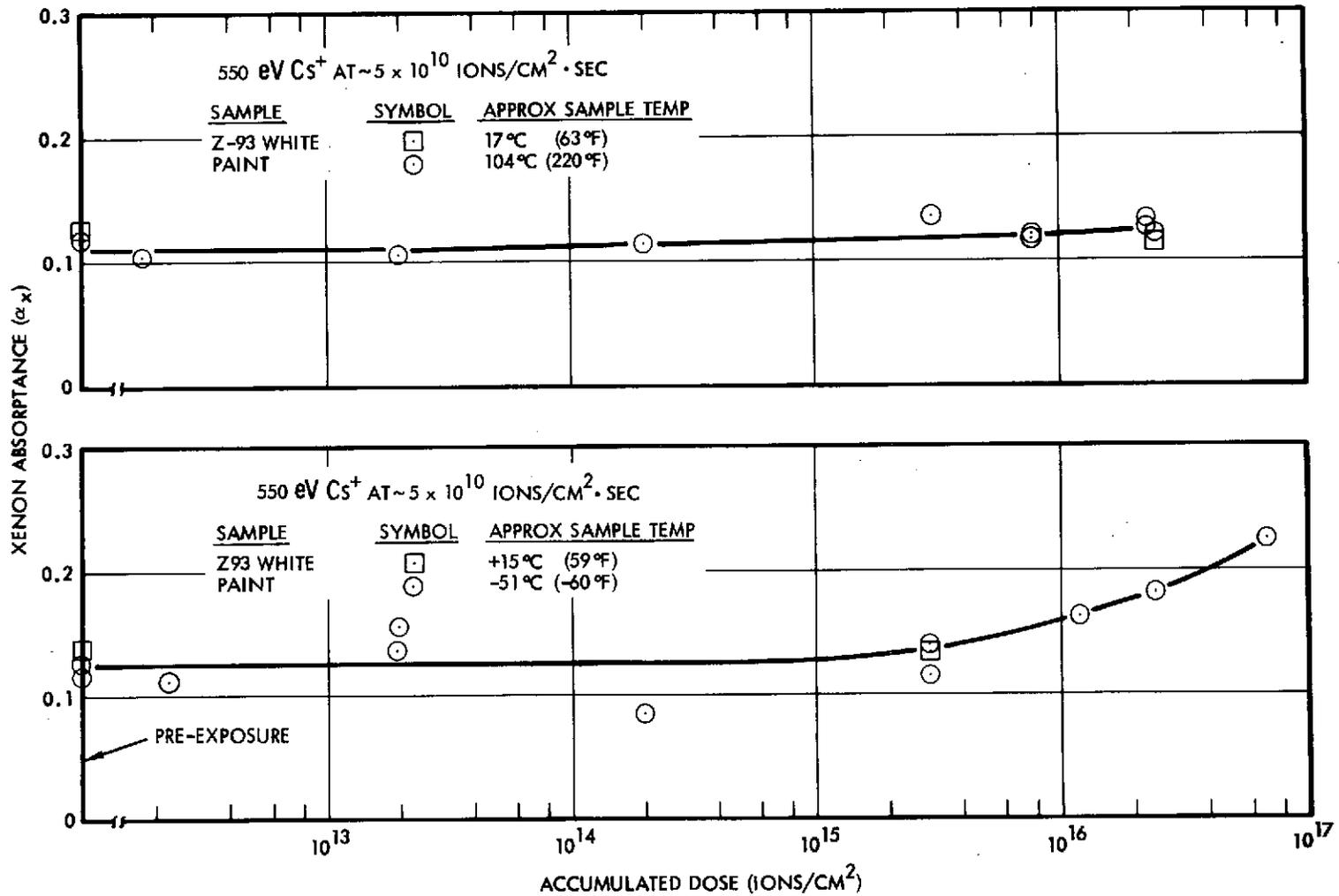
Figure 4-2. Z93 White Paint Xenon Absorptance Degradation at 100°C and -50°C by Energetic Cesium Ions
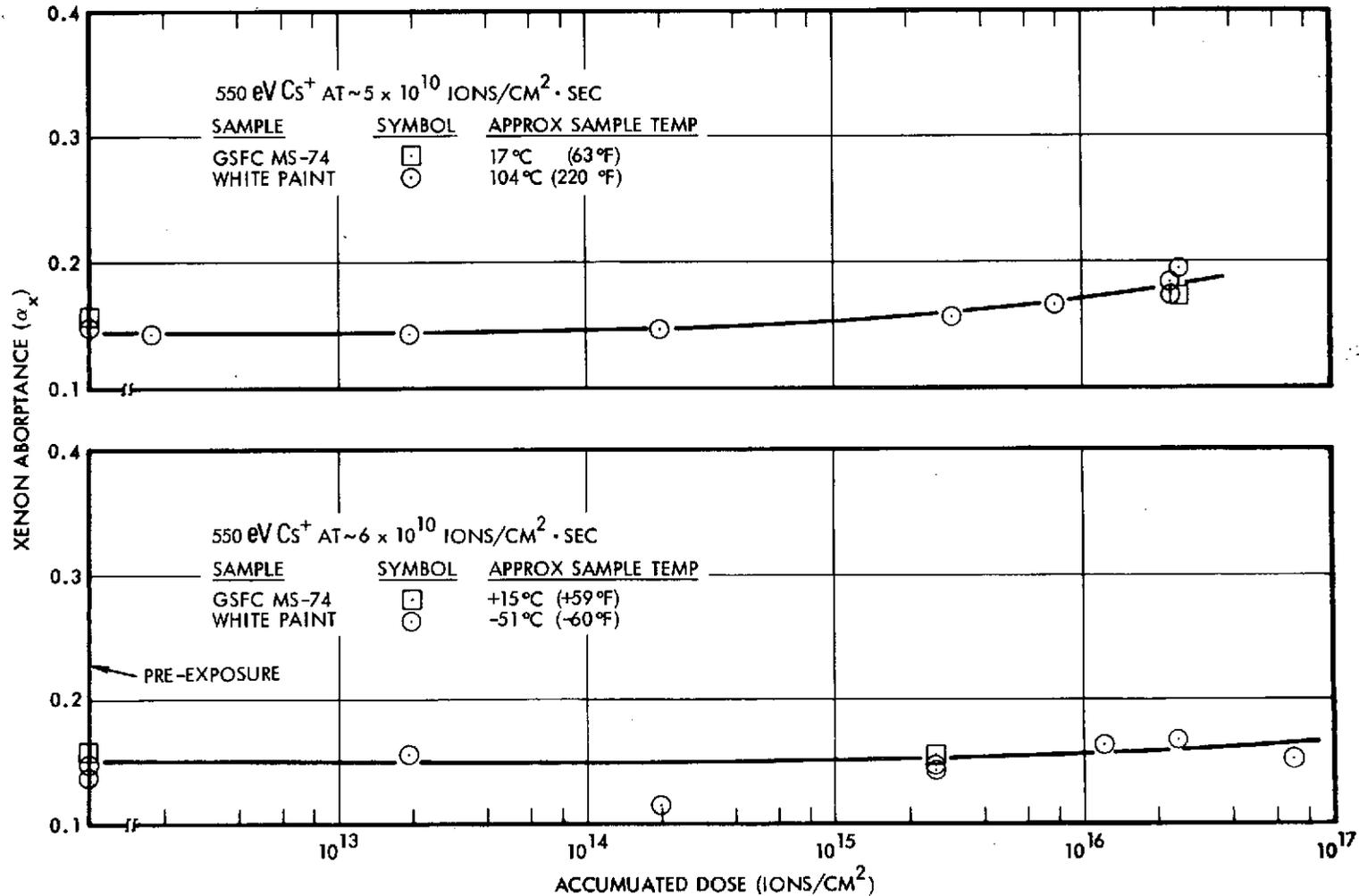
Figure 4-3.   GSFC MS-74 White Paint Xenon Absorptance Degradation at +100°C and -50°C by Energetic Cesium Ions
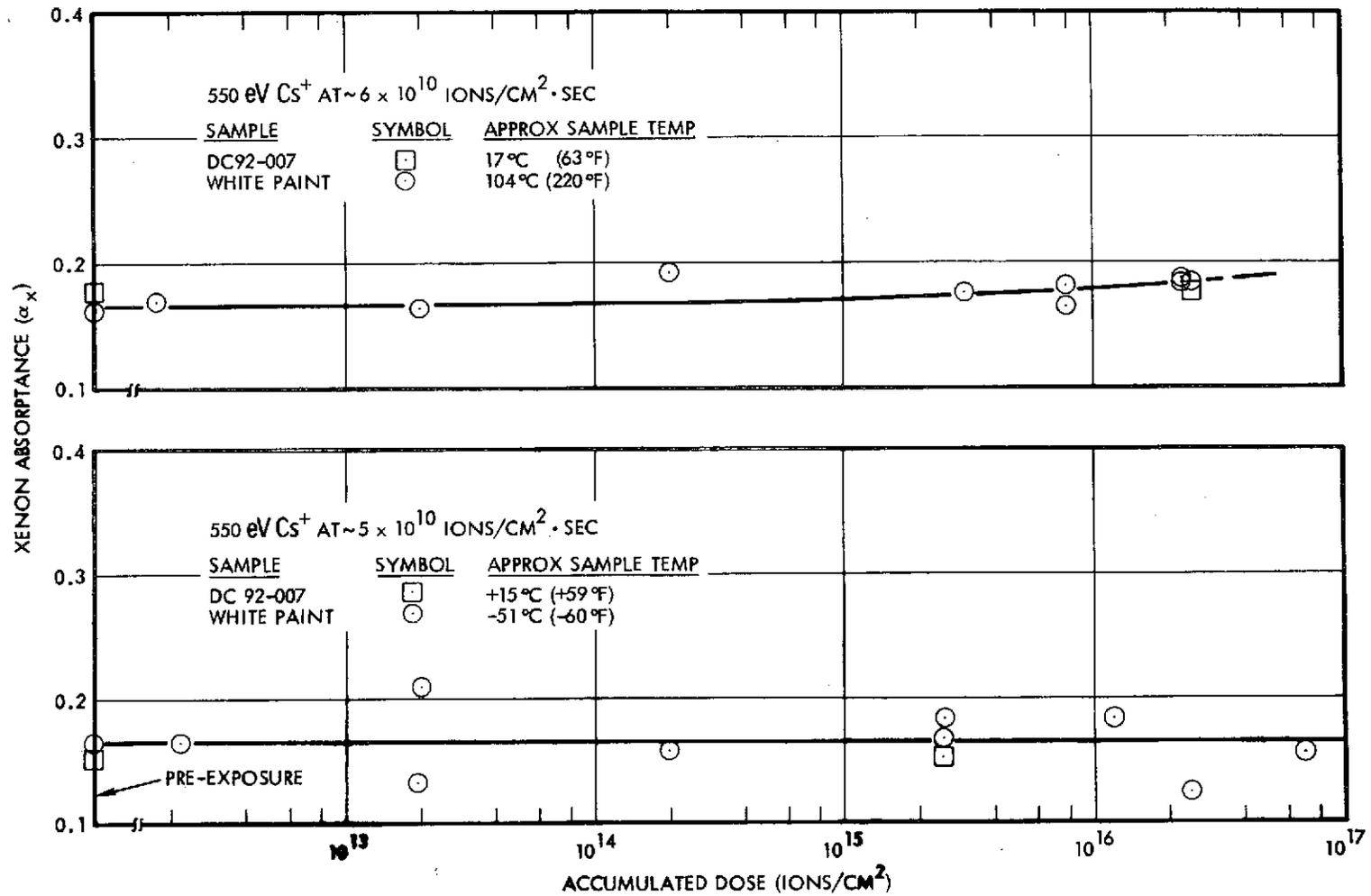
Figure 4-4. DC 92-007 White Paint Xenon Absorptance Degradation at 100°C and
-50°C by Energetic Cesium Ions
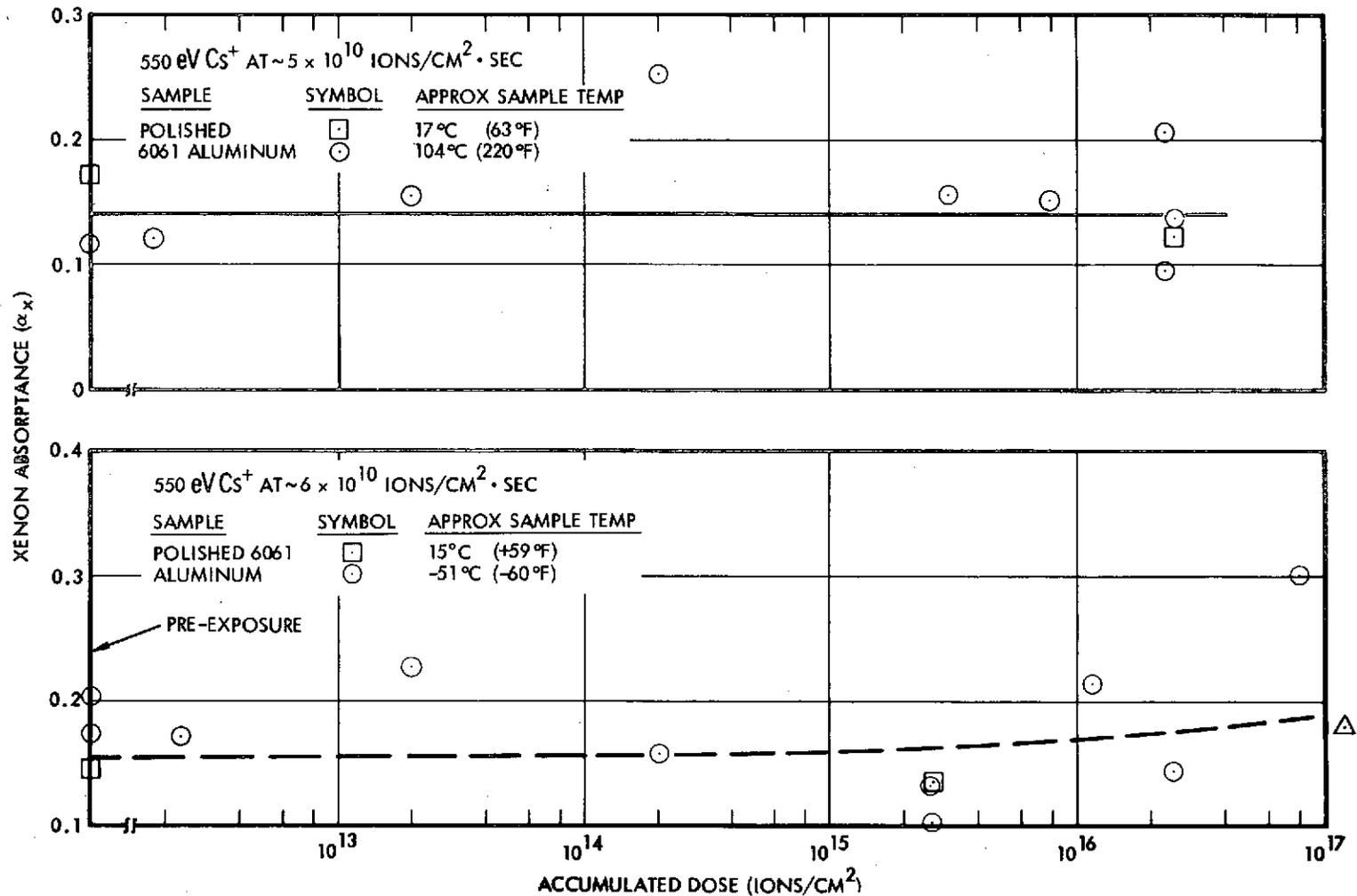
Figure 4-5. Polished Aluminum Xenon Absorptance Degradation at 100°C and -50°C by Energetic Cesium Ions
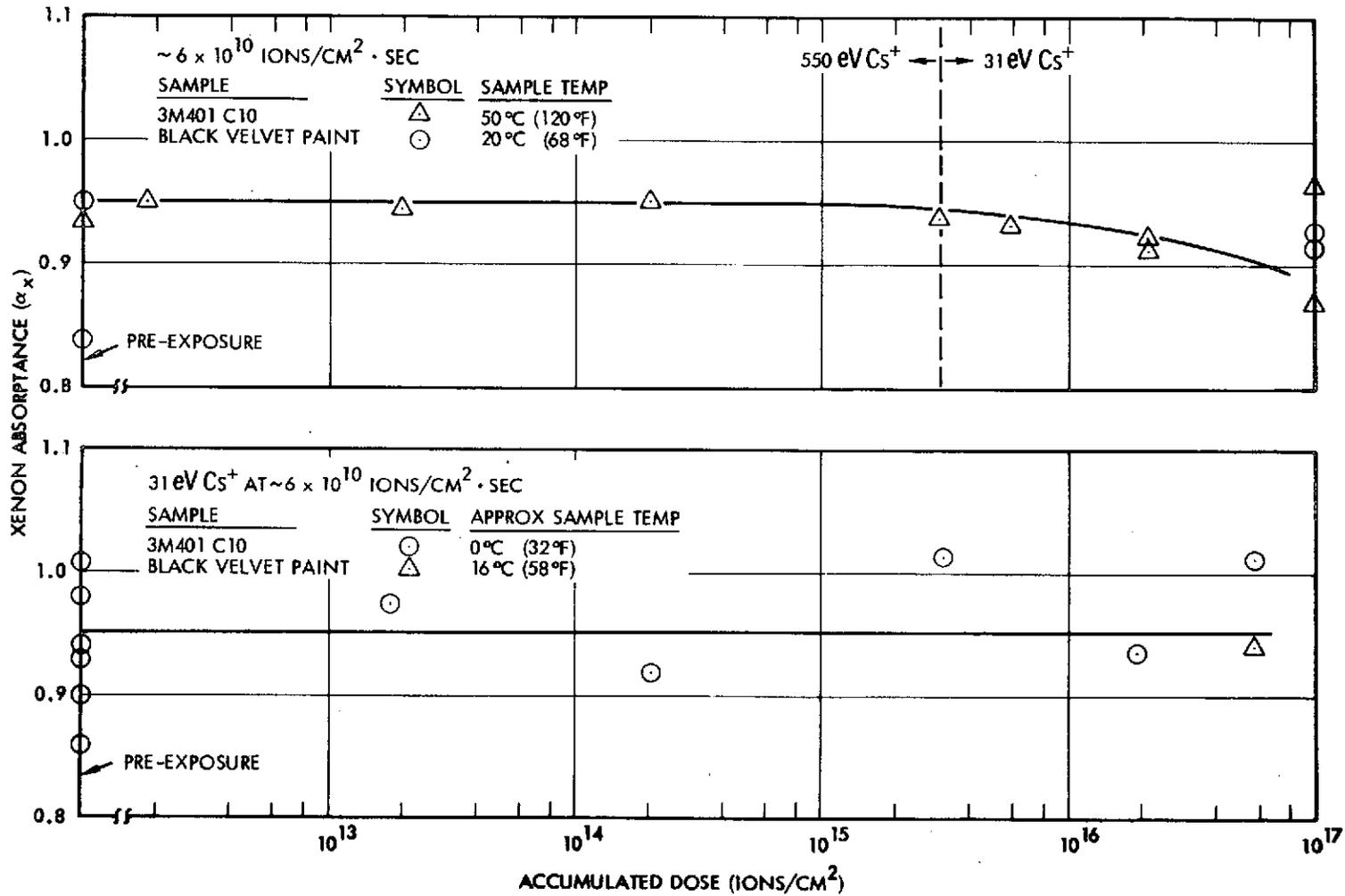
Figure 4-6.   3M 401-C-10 Black Velvet Paint Xenon Absorptance Degradation at 50°C and
0°C by Low Energy Cesium Ions
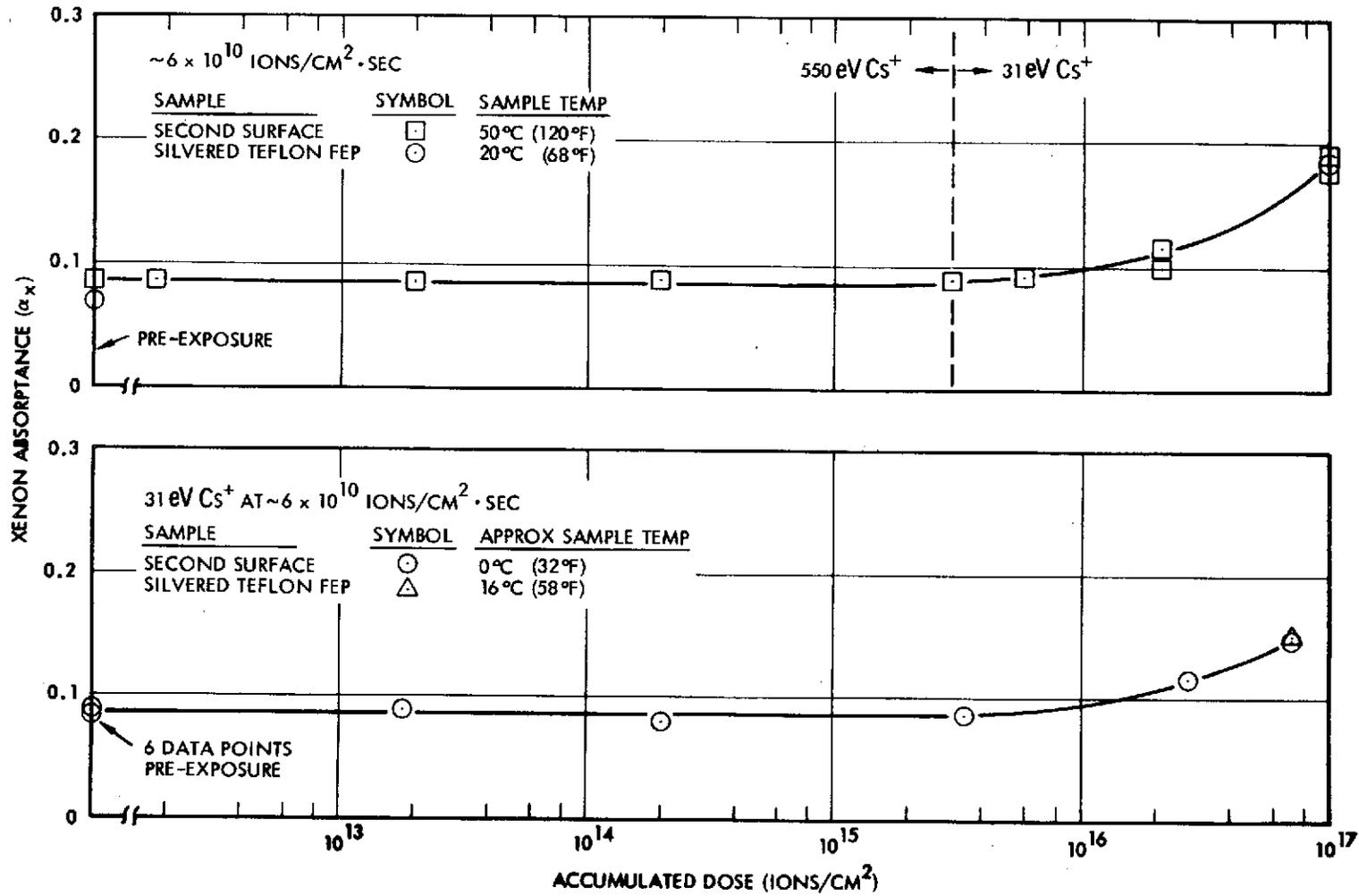
Figure 4-7. Silvered Teflon FEP Xenon Absorptance Degradation at 50°C and
0°C by Low Energy Cesium Ions
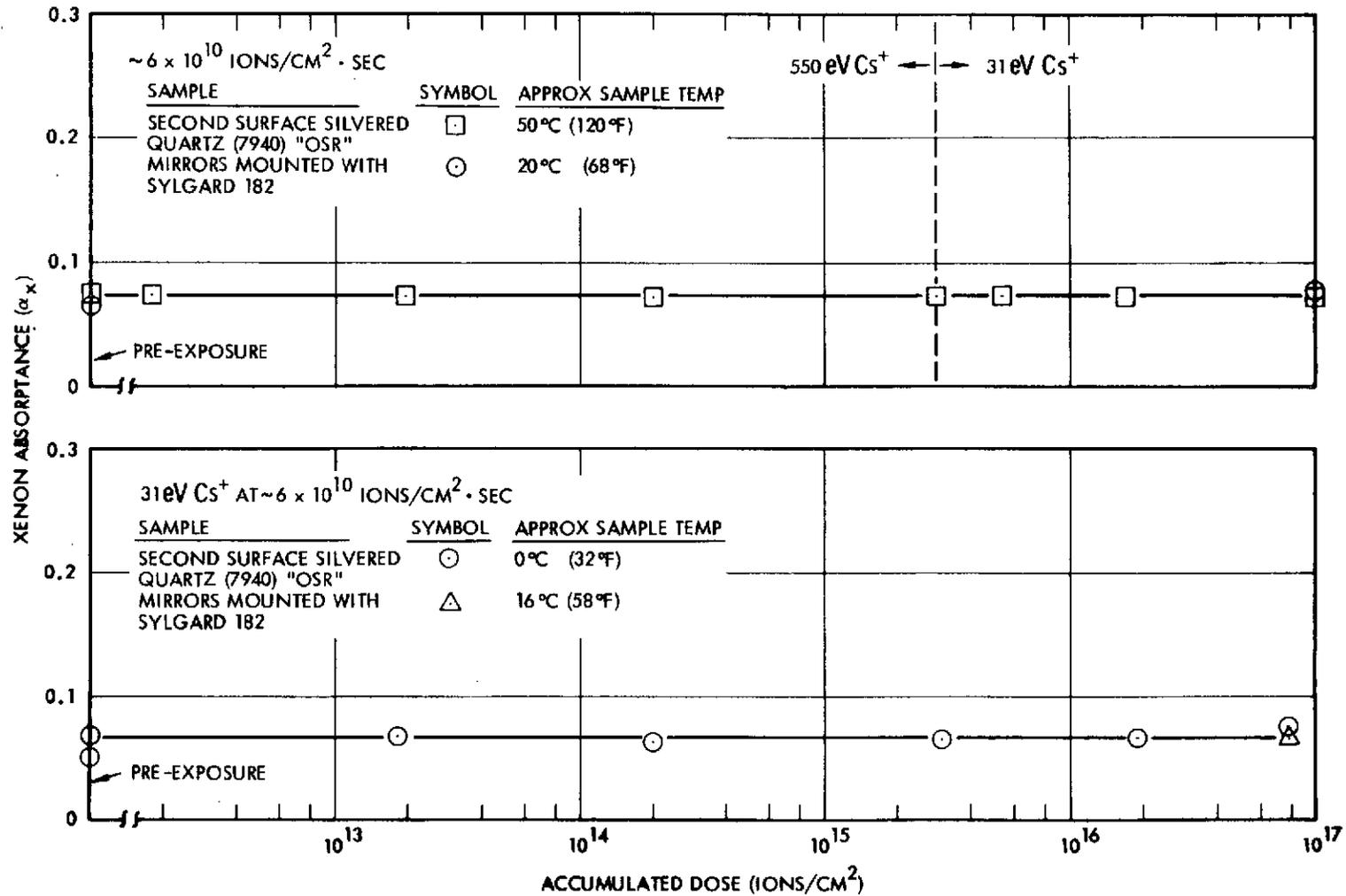
Figure 4-8.   OSR Xenon Absorptance Degradation at 50°C and 0°C by Low Energy Cesium Ions
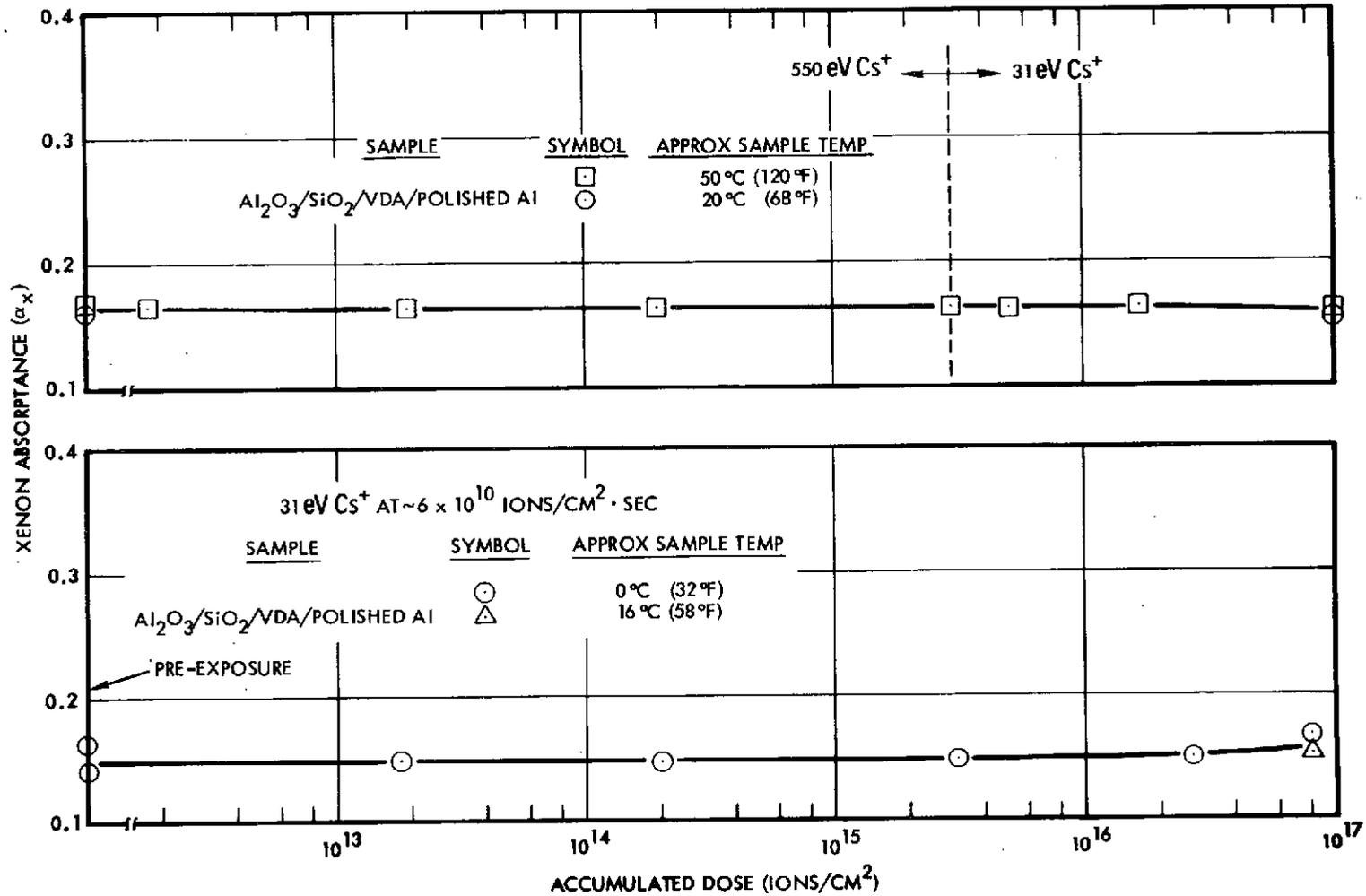
Figure 4-9.   Multilayer Coated VDA Xenon Absorptance Degradation at 50°C and 0°C by Low Energy Cesium Ions
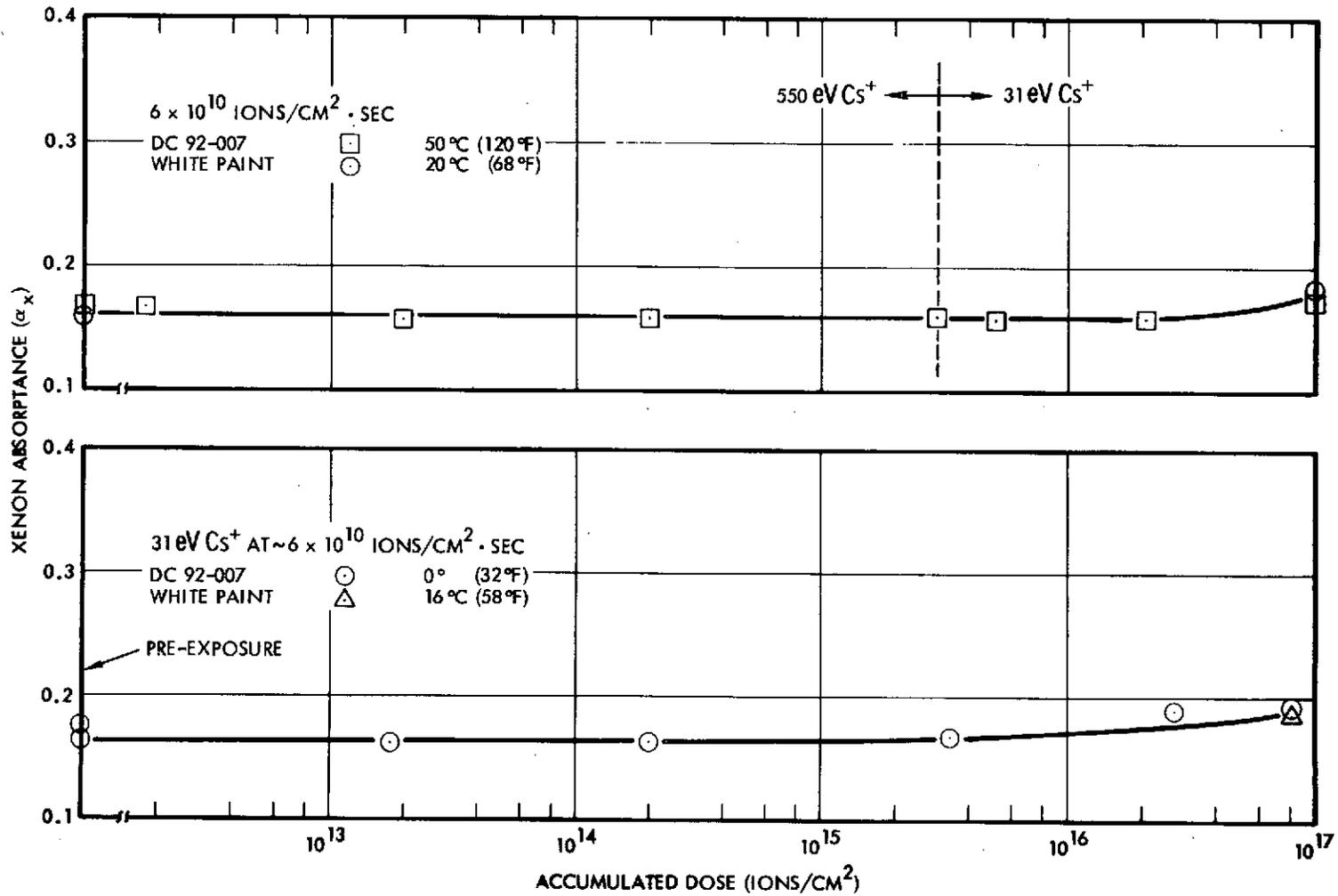
Figure 4-10. DC 92-007 White Paint Xenon Absorptance Degradation at 50°C and 0°C by Low Energy Cesium Ions

3M Velvet Black Paint, which is stable at 30°F up to 6×10^{16} ions/ cm^2, begins to show decreasing absorptance when exposed to 8×10^{16} ions/cm^2 at +120°F (Figure 4-6). This apparent change is fairly small but could become significant for spacecraft design purposes if high ion doses occur at high coating temperatures.

Silvered Teflon degradation began at ion doses near 10^{16} ions/cm^2 and appeared to be insensitive to temperature variations in the range 32° to 120°F (Figure 4-7). The multi-layer $Al_2O_3/SiO_2/VDA$ coating (24 quarter wavelengths of Al_2O_3 and eight of SiO) exhibited essentially no degradation (Figure 4-9), as did the coating identified as polished aluminum, but which appeared to be vacuum deposited aluminum (VDA) on a polished aluminum substrate (Figure 4-5). Second surface mirrors remained stable after exposures up to 8×10^{17} ions/cm^2 for both 32° and 120°F exposures (Figure 4-10). These samples were cemented to an aluminum substrate with Sylgard 182 as shown in Figure 4-11. The gap between mirrors was 10 to 20 mils.

The emittance measurements during the tests reported here have shown more variation than in previous tests. While increased scatter in the data has been noted in previous experiments at temperatures below 0°F (and is to be expected from the attendant lowering of heat flux values), this problem appeared more frequently during 32° and -60°F tests reported here. When test results appear questionable, the runs are repeated and in most cases more consistent data are obtained. The results of multiple data taking are shown in the plotted and tabulated data.

In three instances emittance values become eroneously high near the end of the test. This problem is believed to be the result of a thermal short or heat leak between the sample or sample heater and the ion shield or base plate. Such a heat leak would have very little effect on the α_x value since α_x is obtained by subtracting electrical heat required with sun OFF from electrical heat required with sun ON, and since the sample temperature is approximately the same under both sun conditions. Examination of the samples and sample holders after removal from vacuum (both before and after the samples were taken off) showed no apparent cause for the postulated heat leak. Thus, if thermal shorting
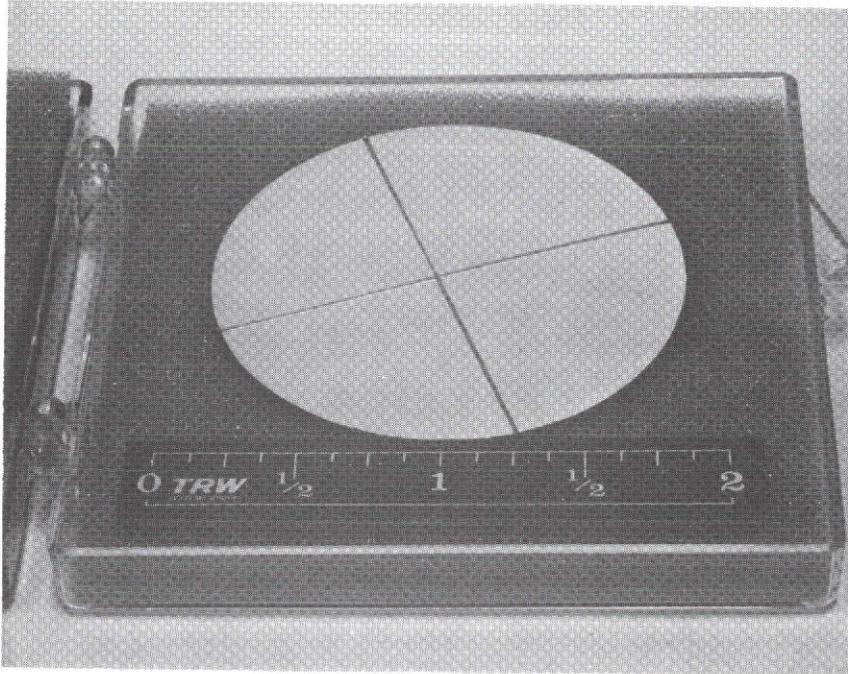
Figure 4-11. Photograph of OSR Mirror Sample. Square mirrors were cemented to circular aluminum substrate and then trimmed with miniature sandblaster.

did occur, the foreign material that caused it must have oxidized and/or evaporated when returned to the atmosphere.

4.4 CONCLUSIONS

1) Xenon absorptance (α_x) of Kapton, Z93 and silvered Teflon FEP begin to show the onset of rapid increases when the total dose reaches a level of 1×10^{16} ions/cm^2.

2) For Kapton, the rate of α_x degradation appears to be retarded by low sample temperatures. The degradation rate for Z93 is apparently affected in just the opposite way; i.e., the rate is accelerated by low sample temperature. This is not entirely surprising; Reference 3 shows that Z93 and several other coatings displayed similar acceleration of mercury ion degradation rates for reduced sample temperature.

3) The other sample materials (MS 74, DC 92 007, OSR second surface mirrors, multi-layer Al$_2$O$_3$/SiO$_2$/VDA, 3M Velvet Black, and VDA) show only slight α_x degradation after a total dose of approximately 1×10^{16} cesium ions/cm^2 at both low and high sample temperatures.

4)   Hemispherical emittance (ϵ_H) for each sample material tended to remain essentially constant during the high temperature series. Apparent increases in ϵ_H for some of the samples during the low temperature series are believed to be in error due to temporarily increased heat leakage from the sample or sample heater to the ion shield of base plate. Such heat leaks would have little effect on α_X.

5)   Data for the DC 92-007 sample, even though exposed at different temperatures, did not indicate any strong ion energy effect in degradation data.

5. CESIUM ATOM EFFECTS ON
THERMOPHYSICAL PROPERTIES

5.1 INTRODUCTION

This section will present the results of cesium atom exposures on selected thermal control surfaces. The cesium atom test matrix is shown in Table 5-1.

Table 5-1. Cesium Atom Thermal Coating
Test Matrix

Material	Temperature	Figure No.	Table No.
(R) Z93 White Paint	-50°C +100°C	5-1	5-2
(NN) DC 92-007 White Paint	-50°C +50°C +100°C	5-2	5-3
(G) Kapton, Rear Surface Aluminized	-50°C +50°C	5-3	5-4
(A) "Polished" Aluminum (VDA?)	-50°C +100°C	5-4	5-5
(--) GSFC MS74 White Paint	-50°C -50°C	5-5	5-6
	+50°C +100°C	5-6	
(MM) Rear Surface Silvered FEP Teflon	-50°C +50°C	5-7	5-7
(KK) "OSR" Second Surface Mirrors	-50°C +50°C	5-8	5-8
(--) Al_2O_3/SiO_2/VDA	-50°C +100°C	5-9	5-9
(PPP) 3M 401 C 10 Velvet Black Paint	-50°C	5-10	5-10

5.2 RESULTS

Tables 5-2 through 5-10 give complete data tabulations for each sample. The last column in these tables is the elapsed time between the end of the last exposure and the measurement of the sample properties. This information is useful in assessing the time dependence of sample properties. In some cases, "healing" of absorptance damage was observed. The xenon absorptance data has been plotted in Figures 5-1 through 5-10 and grouped by material as shown in Table 5-1. The cesium arrival rates were approximately 10^{12} atoms/cm^2 sec. The actual values are shown in the tabulations for each material.

5.3 DISCUSSION

In general, exposure to cesium atoms produced greater absorptance degradation to thermal coatings than exposure to cesium ions. As in the ion exposures, sample temperature was an important parameter but strongly material dependent. Due to the variations in material performance, each material will be discussed separately and the results compared to earlier test data. The second item of major significance was the strong time-temperature interrelationship found during thermophysical property measurements of the white paint and silvered Teflon FEP samples.

As with previous mercury and cesium ion tests, no changes were induced in the infrared emittance of the samples. Experimental difficulties were experienced in low temperature emittance measurements on two of the five sample positions. Sample position No. 1, which held Polished Aluminum and 3M Black, respectively, on the two -50°C exposures, yielded scattered ϵ_H values. It has been "noisy" throughout all of the test series. At low temperature, where measured quantities are small, the effects of noise become more pronounced. The absorptance measurements of these two samples at -50°C also show more than average scatter. In contrast, sample position No. 2, which held Z93 and Silvered Teflon, respectively, on the two -50°C exposures, yielded emittance values which were consistently high. In fact, this low temperature behavior began near the end of the -50°C cesium ion exposure series (following a thermal cycle to room temperature) and has persisted thereafter. Position No. 2 failed in 1971 and was rebuilt just prior to

Table 5-2. Degradation of Z93 White Paint
Due to Cesium Atom Impingement

DATE	TEMP. (°F)	ENERGY (°K)	FLUX $\left(\frac{ATOMS}{CM^2 \cdot SEC}\right)$	TOTAL EXP.TIME (HRS.)	DOSE (ATOMS/CM²)	α_x	ε_H	MEAS* DELAY (HRS.)
3-17-72	+59	~1000	0	0	0	.14	.88	----
3-20-72	-64	"	0	0	0	.11	1.07	----
"	"	"	1 x 10¹²	0.1	4.0 x 10¹⁴	.13	1.09	1.5
3-21-72	"	"	"	1.1	4.3 x 10¹⁵	.12	1.10	16.5
3-22-72	-63	"	"	7.1	2.7 x 10¹⁶	.15	1.15	16.5
3-23-72	"	"	"	27.6	1.0 x 10¹⁷	.66	1.15	2.5
"	"	"	"	"	"	.72	1.20	3.5
3-24-72	-62	"	"	46.2	1.7 x 10¹⁷	.70	1.14	2.0
3-28-72	-59	"	"	72.5	2.6 x 10¹⁷	.78	1.03	69.0
"	-57	"	"	"	"	.76	1.03	70.0
"	+59	"	"	"	"	.46	.96	74.0
3-29-72	"	"	"	"	"	.21	.91	92.0
4-14-72	+62	~1000	0	0	0	.12	.89	----
4-18-72	+207	"	0	0	0	.12	.91	----
4-19-72	+213	"	1 x 10¹²	0.1	3.6 x 10¹⁴	.14	.93	17.8
"	+210	"	"	1.1	4.0 x 10¹⁵	.13	.92	1.2
4-20-72	"	"	"	6.1	2.2 x 10¹⁶	.16	.93	0.8
4-21-72	+208	"	8 x 10¹¹	21.1	6.6 x 10¹⁶	.16	.92	1.4
4-24-72	+213	"	9 x 10¹¹	91.1	2.9 x 10¹⁷	.22	.96	1.0
"	"	"	"	"	"	.17	.92	2.6
"	+211	"	1 x 10¹²	92.4	3.0 x 10¹⁷	.15	.90	1.2
4-25-72	+209	"	"	"	"	.15	.91	19.8
"	+64	"	"	"	"	.15	.92	26.0
"	"	"	"	"	"	.15	.92	27.4

*Time From End of Exposure to α_x Measurement.

Table 5-3. Degradation of DC 92-007 White Paint Due to Cesium Atom Impingement

DATE	TEMP. (°F)	ENERGY (°K)	FLUX $\left(\frac{\text{ATOMS}}{\text{CM}^2 \cdot \text{SEC}}\right)$	TOTAL EXP.TIME (HRS.)	DOSE (ATOMS/CM²)	α_x	ε_H	MEAS.* DELAY (HRS.)
2-28-72	-58	~1000	0	0	0	.19	.92	---
"	"	"	"	"	"	.14	.85	---
3-3-72	"	"	2×10^{10}	0.1	6.8×10^{12}	.15	.89	3.0
3-7-72	-59	"	9×10^{11}	0.2	3.2×10^{14}	.16	.88	3.0
3-8-72	-61	"	7×10^{11}	1.2	2.9×10^{15}	.16	.86	20.0
3-9-72	-56	"	8×10^{11}	19.2	5.8×10^{16}	.14	.86	6.0
3-10-72	"	"	1×10^{12}	34.2	1.4×10^{17}	.20	.91	3.0
3-13-72	-55	"	"	61.5	2.4×10^{17}	.24	.96	39.0
"	+59	"	"	"	"	.16	.86	45.0
3-31-72	+61	~1000	0	0	0	.16	.81	---
4-3-72	+121	"	0	0	0	.16	.82	---
"	"	"	1×10^{12}	0.1	3.6×10^{14}	.16	.82	1.0
4-4-72	"	"	"	1.1	4.3×10^{15}	.16	.82	16.0
"	"	"	"	6.6	2.4×10^{16}	.16	.82	0.6
4-5-72	"	"	"	"	"	.16	.82	18.1
4-6-72	+122	"	"	21.6	7.8×10^{16}	.17	.82	1.8
4-7-72	"	"	"	48.3	1.9×10^{17}	.17	.82	1.4
4-10-72	"	"	"	79.9	3.1×10^{17}	.18	.80	34.3
"	+62	"	"	"	"	.18	.80	38.7
4-11-72	+63	"	"	"	"	.18	.80	58.6
4-14-72	+62	~1000	0	0	0	.16	.81	---
4-18-72	+209	"	0	0	0	.17	.83	---
4-19-72	+216	"	1×10^{12}	0.1	3.6×10^{14}	.15	.82	17.7
"	+213	"	"	1.1	4.0×10^{15}	.16	.82	1.1
4-20-72	+214	"	"	6.1	2.2×10^{16}	.16	.82	0.8
4-21-72	+209	"	8×10^{11}	21.1	6.6×10^{16}	.16	.81	1.3
4-24-72	+217	"	9×10^{11}	91.1	2.9×10^{17}	.16	.80	0.9
"	+213	"	1×10^{12}	92.4	3.0×10^{17}	.18	.82	1.0
4-25-72	+65	"	"	"	"	.18	.82	25.8

*Time From End of Exposure to α_x Measurement.

Table 5-4. Degradation of 3 Mil Kapton, Aluminized on Rear Surface, Due to Cesium Atom Exposure

DATE	TEMP. (°F)	ENERGY (°K)	FLUX $\left(\frac{ATOMS}{CM^2 \cdot SEC}\right)$	TOTAL EXP.TIME (HRS.)	DOSE (ATOMS/CM²)	α_x	ϵ_H	MEAS. DELAY (HRS.)*
2-28-72	-58	~1000	0	0	0	.34	.80	---
3-3-72	-59	"	2×10^{10}	0.1	6.8×10^{12}	.29	.80	3.0
3-7-72	"	"	9×10^{11}	0.2	3.2×10^{14}	.40	.87	3.0
3-8-72	-58	"	7×10^{11}	1.2	2.9×10^{15}	.37	.82	20.0
3-9-72	-56	"	8×10^{11}	19.2	5.8×10^{16}	.35	.81	6.0
3-10-72	"	"	1×10^{12}	34.2	1.4×10^{17}	.36	.81	3.0
3-13-72	-55	"	"	61.5	2.4×10^{17}	.32	.80	39.0
"	+58	"	"	"	"	.35	.83	45.0
3-31-72	+60	~1000	0	0	0	.33	.80	---
4-3-72	+121	"	0	0	0	.33	.82	---
"	"	"	1×10^{12}	0.1	3.6×10^{14}	.34	.82	1.0
4-4-72	"	"	"	1.1	4.3×10^{15}	.38	.82	16.0
"	+120	"	"	6.6	2.4×10^{16}	.46	.82	1.1
4-5-72	"	"	"	"	"	.50	.81	18.5
"	"	"	"	"	"	.50	.81	19.3
4-6-72	"	"	"	21.6	7.8×10^{16}	.53	.81	1.2
4-7-72	+121	"	"	48.3	1.9×10^{17}	.58	.81	0.8
4-10-72	"	"	"	79.9	3.1×10^{17}	.70	.79	33.9
"	+61	"	"	"	"	.67	.79	38.6
4-11-72	+62	"	"	"	"	.67	.78	58.1

*Time From End of Exposure to α_x Measurement.

Table 5-5. Degradation of Polished Aluminum (VDA?)
Due to Cesium Atom Impingement

DATE	TEMP. (°F)	ENERGY (°K)	FLUX $\left(\frac{\text{ATOMS}}{\text{CM}^2\cdot\text{SEC}}\right)$	TOTAL EXP.TIME (HRS.)	DOSE (ATOMS/CM²)	α_x	ε_H	MEAS.* DELAY (HRS.)
2-28-72	-56	~1000	0	0	0	.31	.44	---
3-3-72	-58	"	2×10^{10}	0.1	6.8×10^{12}	.20	.29	3.0
3-7-72	"	"	9×10^{11}	0.2	3.2×10^{14}	.28	.21	3.0
3-8-72	-57	"	7×10^{11}	1.2	2.9×10^{15}	.31	.30	20.0
3-9-72	-55	"	8×10^{11}	19.2	5.8×10^{16}	.20	.23	6.0
3-10-72	"	"	1×10^{12}	34.2	1.4×10^{17}	.08	.31	3.0
3-13-72	"	"	"	61.5	2.4×10^{17}	.28	.31	39.0
3-13-72	+60	"	"	"	"	.26	.15	45.0
4-14-72	+63	~1000	0	0	0	.15	.08	---
4-18-72	+212	"	0	0	0	.22	.09	---
4-19-72	+215	"	1×10^{12}	0.1	3.6×10^{14}	.19	.07	18.1
"	"	"	"	1.1	4.0×10^{15}	.19	.07	1.5
4-20-72	+214	"	"	6.1	2.2×10^{16}	.18	.07	1.1
4-21-72	"	"	8×10^{11}	21.1	6.6×10^{16}	.20	.08	1.7
4-24-72	+215	"	9×10^{11}	91.1	2.9×10^{17}	.21	.09	1.4
"	+217	"	1×10^{12}	92.4	3.0×10^{17}	.18	.07	1.6

*Time From End of Exposure to α_x Measurement.

5-6

Table 5-6. Degradation of GSFC MS74 White Paint Due to Cesium Atom Impingement

DATE	TEMP. (°F)	ENERGY (°K)	FLUX ($\frac{ATOMS}{CM^2 \cdot SEC}$)	TOTAL EXP.TIME (HRS.)	DOSE (ATOMS/CM²)	α_x	ε_H	MEAS.* DELAY (HRS.)
2-28-72	-58	∿1000	0	0	0	.17	.89	---
3-3-72	-59	"	2×10^{10}	0.1	6.8×10^{12}	.13	.89	3.0
3-7-72	"	"	9×10^{11}	0.2	3.2×10^{14}	.16	.89	3.0
3-8-72	-58	"	7×10^{11}	1.2	2.9×10^{15}	.16	.89	20.0
3-9-72	-56	"	8×10^{11}	19.2	5.8×10^{16}	.68	.90	6.0
"	"	"	"	"	"	.67	.91	8.0
3-10-72	"	"	1×10^{12}	34.2	1.4×10^{17}	.75	.90	3.0
"	"	"	"	"	"	.73	.90	3.5
3-13-72	-55	"	"	61.5	2.4×10^{17}	.76	.91	39.0
"	+59	"	"	"	"	.57	.87	45.0
3-17-72	59	∿1000	0	0	0	.14	.86	---
3-20-72	-65	"	0	0	0	.19	1.00	---
"	-64	"	0	0	0	.13	.92	---
"	"	"	1×10^{12}	0.1	4.0×10^{14}	.13	.91	1.5
3-21-72	"	"	"	1.1	4.3×10^{15}	.14	.92	16.5
3-22-72	-63	"	"	7.1	2.7×10^{16}	.15	.92	16.5
3-23-72	"	"	"	27.6	1.0×10^{17}	.82	.93	2.5
"	"	"	"	"	"	.76	.86	3.5
3-24-72	-62	"	"	46.2	1.7×10^{17}	.75	.82	2.0
3-28-72	-59	"	"	72.5	2.6×10^{17}	.94	.92	69.0
"	-57	"	"	"	"	.79	.80	70.0
"	+59	"	"	"	"	.51	.88	74.0
"	"	"	"	"	"	.43	.88	75.0
3-29-72	"	"	"	"	"	.37	.88	92.0

*Time From End of Exposure to α_x Measurement.

Table 5-6. Degradation of GSFC MS74 White Paint Due to Cesium Atom Impingement (Continued)

DATE	TEMP. ($^\circ$F)	ENERGY ($^\circ$K)	FLUX $\left(\frac{\text{ATOMS}}{\text{CM}^2 \cdot \text{SEC}}\right)$	TOTAL EXP.TIME (HRS.)	DOSE (ATOMS/CM^2)	α_x	ϵ_H	MEAS.* DELAY (HRS.)
3-31-72	+61	$\sim$1000	0	0	0	.14	.87	---
4-3-72	+120	"	0	0	0	.14	.88	---
"	"	"	1×10^{12}	0.1	3.6×10^{14}	.14	.88	1.0
4-4-72	"	"	"	1.1	4.3×10^{15}	.18	.88	16.0
"	+121	"	"	6.6	2.4×10^{16}	.34	.88	0.6
4-5-72	"	"	"	"	"	.32	.88	18.0
4-6-72	+120	"	"	21.6	7.8×10^{16}	.46	.88	1.2
4-7-72	+121	"	"	48.3	1.9×10^{17}	.54	.88	0.8
4-10-72	"	"	"	79.9	3.1×10^{17}	.58	.87	33.8
"	+61	"	"	"	"	.56	.89	38.3
4-11-72	"	"	"	"	"	.57	.88	57.9
4-14-72	+62	$\sim$1000	0	0	0	.14	.87	---
4-18-72	+207	"	0	0	0	.13	.88	---
4-19-72	+213	"	1×10^{12}	0.1	3.6×10^{14}	.12	.87	17.6
"	+210	"	"	1.1	4.0×10^{15}	.16	.84	1.0
"	+209	"	"	"	"	.17	.87	1.6
4-20-72	+212	"	"	6.1	2.2×10^{16}	.35	.87	0.7
4-21-72	+208	"	8×10^{16}	21.1	6.6×10^{16}	.48	.88	1.2
4-24-72	+216	"	9×10^{17}	91.1	2.9×10^{17}	.55	.87	0.8
"	"	"	"	"	"	.54	.87	1.7
"	+212	"	1×10^{12}	92.4	3.0×10^{17}	.54	.88	0.9
4-25-72	+210	"	"	"	"	.47	.87	19.8
"	+64	"	"	"	"	.44	.88	25.6
"	"	"	"	"	"	.44	.87	27.2

*Time From End of Exposure to α_x Measurement.

Table 5-7. Degradation of Silvered Teflon Due to Cesium Atom Impingement

DATE	TEMP. (°F)	ENERGY (°K)	FLUX $\left(\frac{\text{ATOMS}}{\text{CM}^2 \cdot \text{SEC}}\right)$	TOTAL EXP.TIME (HRS.)	DOSE (ATOMS/CM²)	α_x	ϵ_H	MEAS. * DELAY (HRS.)
2-28-72	-57	∿1000	0	0	0	.05	1.04	---
"	-58	"	"	"	"	.09	1.01	---
3-3-72	-59	"	2×10^{10}	0.1	6.8×10^{12}	.04	1.02	3.0
3-7-72	"	"	9×10^{11}	0.2	3.2×10^{14}	.06	1.11	3.0
3-8-72	-58	"	7×10^{11}	1.2	2.9×10^{15}	.14	1.13	20.0
3-9-72	-56	"	8×10^{11}	19.2	5.8×10^{16}	.31	1.16	6.0
3-10-72	-55	"	1×10^{12}	34.2	1.4×10^{17}	.51	1.05	3.0
"	"	"	"	"	"	.51	1.05	3.5
3-13-72	-56	"	"	61.5	2.4×10^{17}	.46	.78	39.0
"	+59	"	"	"	"	.38	.89	45.0
3-31-72	+61	∿1000	0	0	0	.07	.81	---
4-3-72	+120	"	0	0	0	.07	.83	---
"	"	"	1×10^{12}	0.1	3.6×10^{14}	.07	.81	1.0
4-4-72	"	"	"	1.1	4.3×10^{15}	.09	.81	16.0
"	"	"	"	6.6	2.4×10^{16}	.17	.81	1.0
4-5-72	"	"	"	"	"	.17	.81	18.4
4-6-72	+121	"	"	21.6	7.8×10^{16}	.29	.81	1.7
4-7-72	+122	"	"	48.3	1.9×10^{17}	.37	.81	1.3
4-10-72	+120	"	"	79.9	3.1×10^{17}	.46	.83	34.4
"	+60	"	"	"	"	.41	.82	38.4
4-11-72	+61	"	"	"	"	.41	.83	58.0

*Time From End of Exposure to α_x Measurement.

Table 5-8. Degradation of Second Surface-Silvered Mirrors (OSR) Due to Cesium Atom Impingement

DATE	TEMP. (°F)	ENERGY (°K)	FLUX $\left(\frac{ATOMS}{CM^2 \cdot SEC}\right)$	TOTAL EXP.TIME (HRS.)	DOSE (ATOMS/CM²)	α_x	ε_H	MEAS* DELAY (HRS.)
3-17-72	+59	∿1000	0	0	0	.08	.76	---
3-20-72	-65	"	0	0	0	.05	.75	---
"	-64	"	1×10^{12}	0.1	4.0×10^{14}	.07	.77	1.5
3-21-72	"	"	"	1.1	4.3×10^{15}	.07	.77	16.5
3-22-72	-63	"	"	7.1	2.7×10^{16}	.07	.78	16.5
3-23-72	"	"	"	27.6	1.0×10^{17}	.07	.78	2.5
3-24-72	-62	"	"	46.2	1.7×10^{17}	.07	.77	2.0
3-28-72	-59	"	"	72.5	2.6×10^{17}	.07	.78	69.0
"	+59	"	"	"	"	.08	.78	74.0
3-29-72	"	"	"	"	"	.08	.78	92.0
3-31-72	+61	∿1000	0	0	0	.11	.76	---
"	"	"	0	0	0	.11	.75	---
4-3-72	+121	"	0	0	0	.13	.80	---
"	"	"	1×10^{12}	0.1	3.6×10^{14}	.12	.79	1.0
4-4-72	"	"	"	1.1	4.3×10^{15}	.12	.79	16.0
"	"	"	"	6.6	2.4×10^{16}	.12	.79	1.0
4-5-72	"	"	"	"	"	.12	.78	18.3
4-6-72	"	"	"	21.6	7.8×10^{16}	.12	.78	1.6
4-7-72	+122	"	"	48.3	1.9×10^{17}	.12	.79	1.2
4-10-72	+121	"	"	79.9	3.1×10^{17}	.13	.80	34.1
"	+62	"	"	"	"	.12	.78	38.9
4-11-72	"	"	"	"	"	.11	.77	58.4

*Time From End of Exposure to α_x Measurement.

Table 5-9. Degradation of $Al_2O_3/SiO_2/VDA$ Due to Cesium Atom Impingement

DATE	TEMP. (°F)	ENERGY (°K)	FLUX $\left(\frac{ATOMS}{CM^2 \cdot SEC}\right)$	TOTAL EXP.TIME (HRS.)	DOSE (ATOMS/CM^2)	α_x	ϵ_H	MEAS.* DELAY (HRS.)
3-17-72	59	∿1000	0	0	0	.16	.66	---
3-20-72	-64	"	0	0	0	.14	.71	---
"	"	"	1×10^{12}	0.1	4.0×10^{14}	.15	.71	1.5
3-21-72	"	"	"	1.1	4.3×10^{15}	.15	.71	16.5
3-22-72	-63	"	"	7.1	2.7×10^{16}	.15	.71	16.5
3-23-72	-62	"	"	27.6	1.0×10^{17}	.15	.72	2.5
3-24-72	-61	"	"	46.2	1.7×10^{17}	.15	.70	2.0
3-28-72	-58	"	"	72.5	2.6×10^{17}	.16	.74	69.0
"	+60	"	"	"	"	.16	.68	74.0
3-29-72	"	"	"	"	"	.16	.68	92.0
4-14-72	+63	∿1000	0	0	0	.19	.68	---
4-18-72	+209	"	0	0	0	.18	.62	---
4-19-72	+212	"	1×10^{12}	0.1	3.6×10^{14}	.18	.62	17.9
"	"	"	"	1.1	4.0×10^{15}	.18	.62	1.3
4-20-72	"	"	"	6.1	2.2×10^{16}	.19	.62	0.9
4-21-72	+211	"	8×10^{11}	21.1	6.6×10^{16}	.18	.62	1.6
4-24-72	+212	"	9×10^{11}	91.1	2.9×10^{17}	.19	.62	1.1
"	+214	"	1×10^{12}	92.4	3.0×10^{17}	.19	.62	1.3
4-25-72	+65	"	"	"	"	.18	.68	25.9

*Time From End of Exposure to α_x Measurement.

Table 5-10. Degradation of 3M 401 C10 Velvet Black Paint
Due to Cesium Atom Impingement

DATE	TEMP. (°F)	ENERGY (°K)	FLUX $\left(\frac{ATOMS}{CM^2 \cdot SEC}\right)$	TOTAL EXP.TIME (HRS.)	DOSE (ATOMS/CM^2)	α_x	ε_H	MEAS.* DELAY (HRS.)
3-17-72	+59	∿1000	0	0	0	1.04	.93	---
3-20-72	-63	"	0	0	0	.78	.95	---
"	-64	"	1 x 10^{12}	0.1	4.0 x 10^{14}	.91	.96	1.5
3-21-72	"	"	"	1.1	4.3 x 10^{15}	.90	1.00	16.5
3-22-72	-63	"	"	7.1	2.7 x 10^{16}	1.01	1.08	16.5
3-23-72	"	"	"	27.6	1.0 x 10^{17}	.87	.96	2.5
3-24-72	-62	"	"	46.2	1.7 x 10^{17}	.90	.97	2.0
3-28-72	-59	"	"	72.5	2.6 x 10^{17}	.94	1.09	69.0
"	+59	"	"	"	"	.92	.93	74.0
3-29-72	"	"	"	"	"	.99	.96	92.0

*Time From End of Exposure to α_x Measurement.

Figure 5-1. Z93 White Paint Xenon Absorptance Degradation at +100°C and -50°C by Cesium Atoms
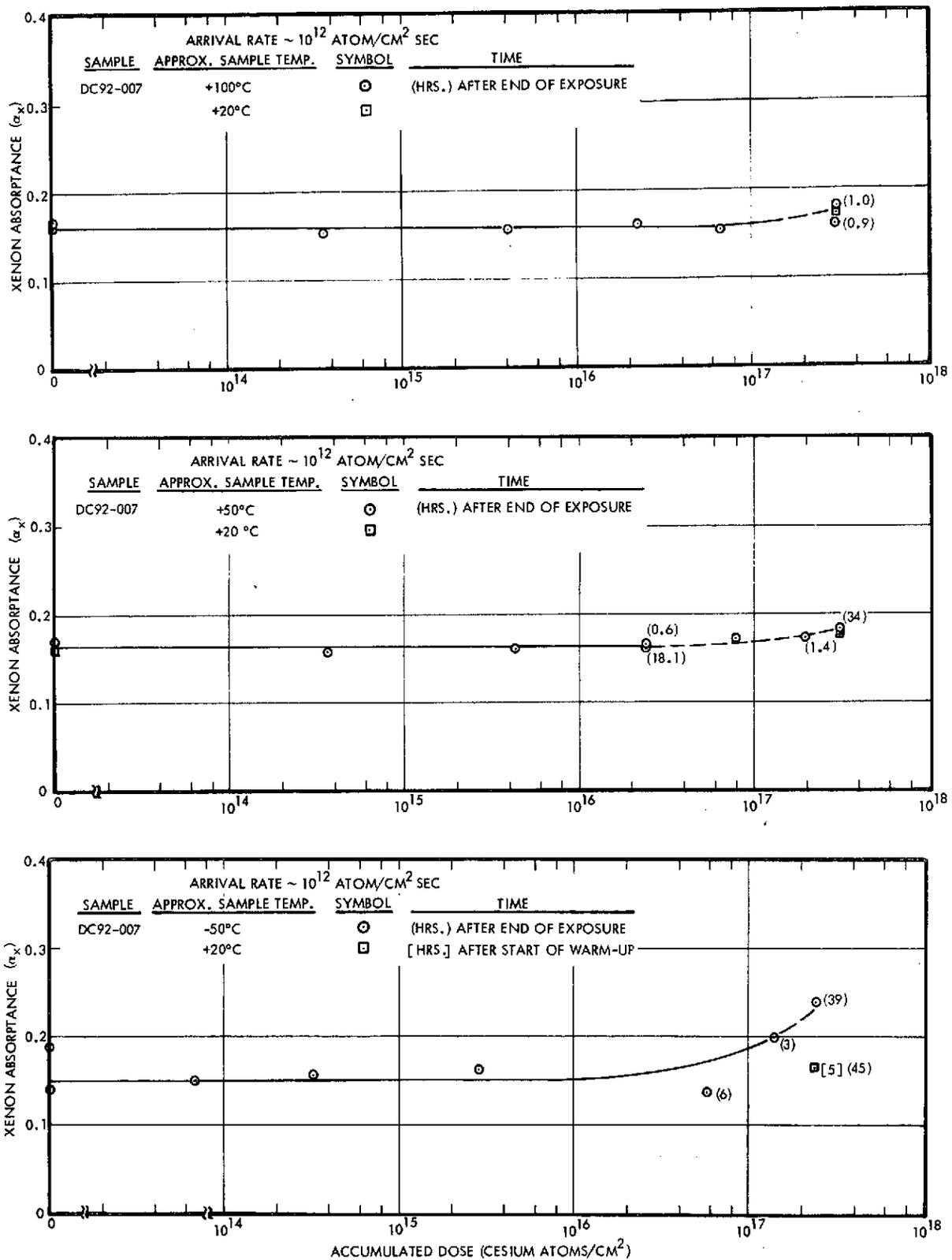
Figure 5-2. DC 92-007 White Paint Xenon Absorptance Degradation at -50°C, +50°C, and +100°C by Cesium Atoms
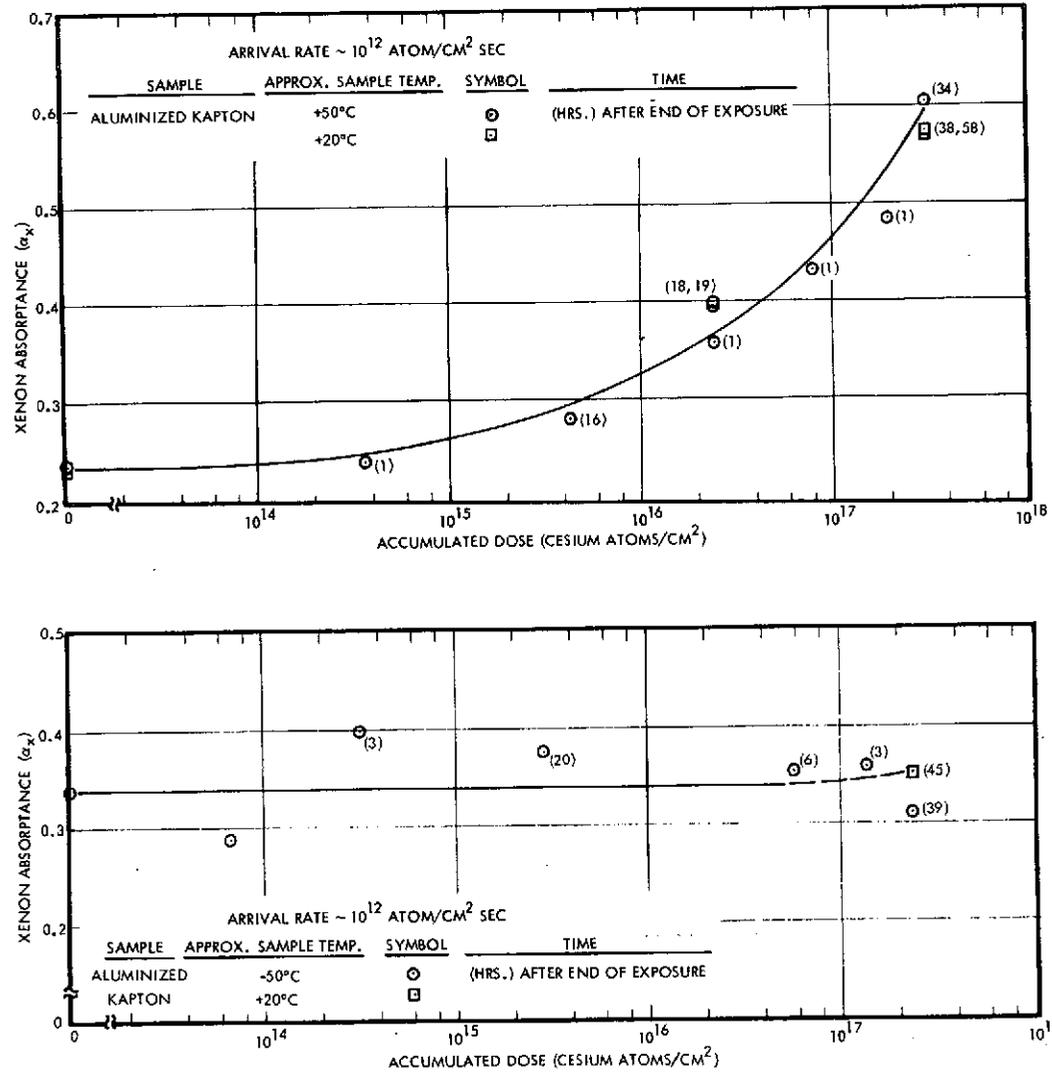
Figure 5-3. Aluminized Kapton Xenon Absorptance Degradation at -50°C and +50°C by Cesium Atoms
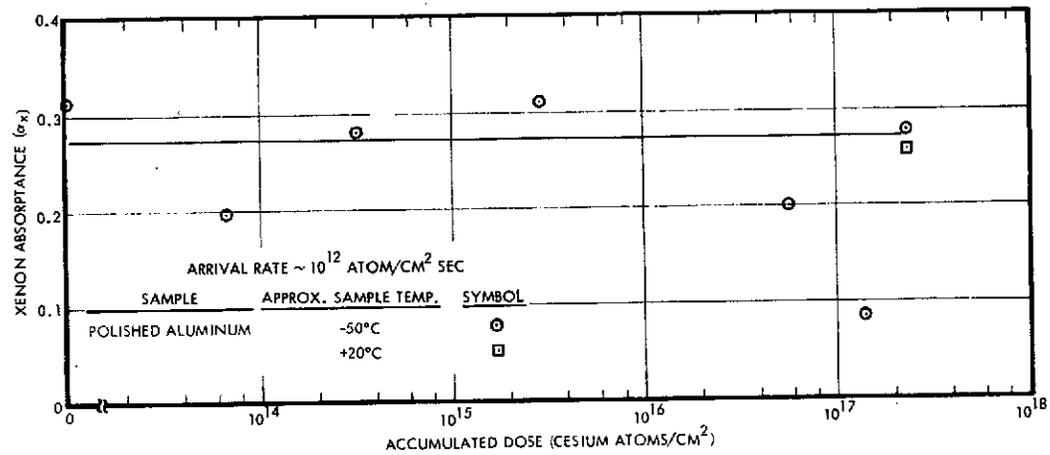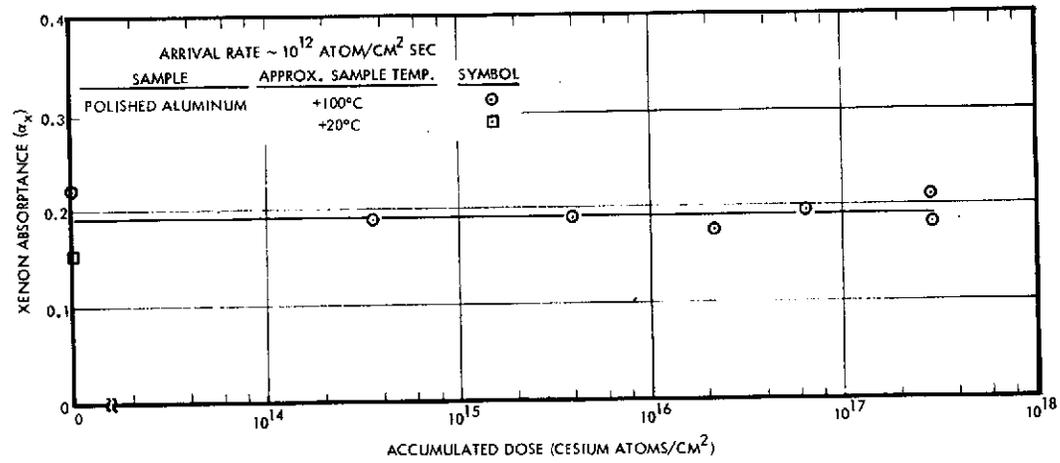
Figure 5-4. "Polished" Aluminum (VDA?) Xenon Absorptance Degradation at -50°C and +100°C by Cesium Atoms

ARRIVAL RATE ~ 10^{12} ATOM/CM^2 SEC

SAMPLE	APPROX. SAMPLE TEMP.	SYMBOL	TIME
GSFC	-50°C	⊙	(HRS.) AFTER END OF EXPOSURE
MS-74	+20°C	⊡	[HRS.] AFTER START OF WARM-UP

XENON ABSORPTANCE (α_x)

ACCUMULATED DOSE (CESIUM ATOMS/CM^2)

ARRIVAL RATE ~ 10^{12} ATOM/CM^2 SEC

SAMPLE	APPROX. SAMPLE TEMP.	SYMBOL	TIME
GSFC	-50°C	⊙	(HRS.) AFTER END OF EXPOSURE
MS-74	+20°C	⊡	[HRS.] AFTER START OF WARM-UP

XENON ABSORPTANCE (α_x)

ACCUMULATED DOSE (CESIUM ATOMS/CM^2)
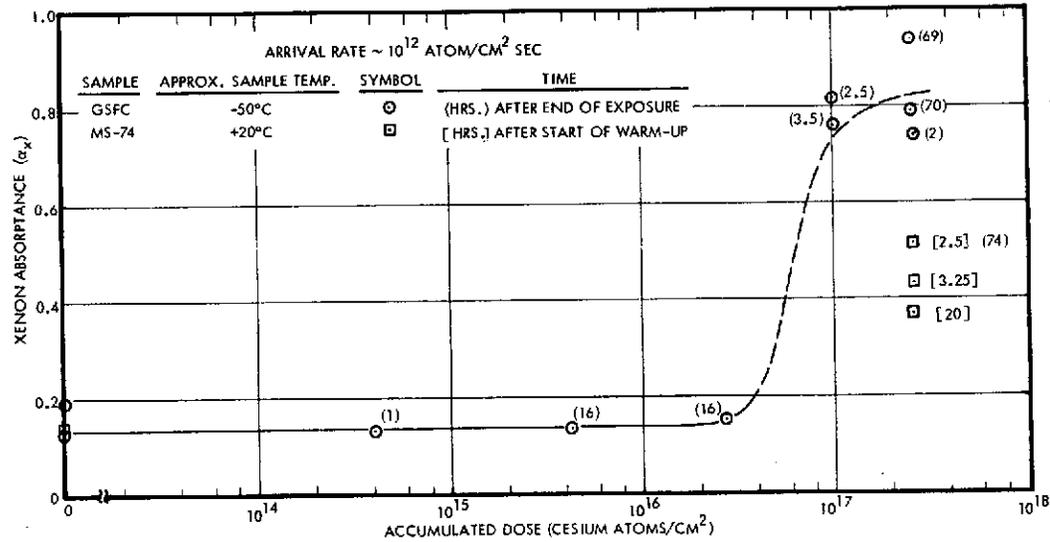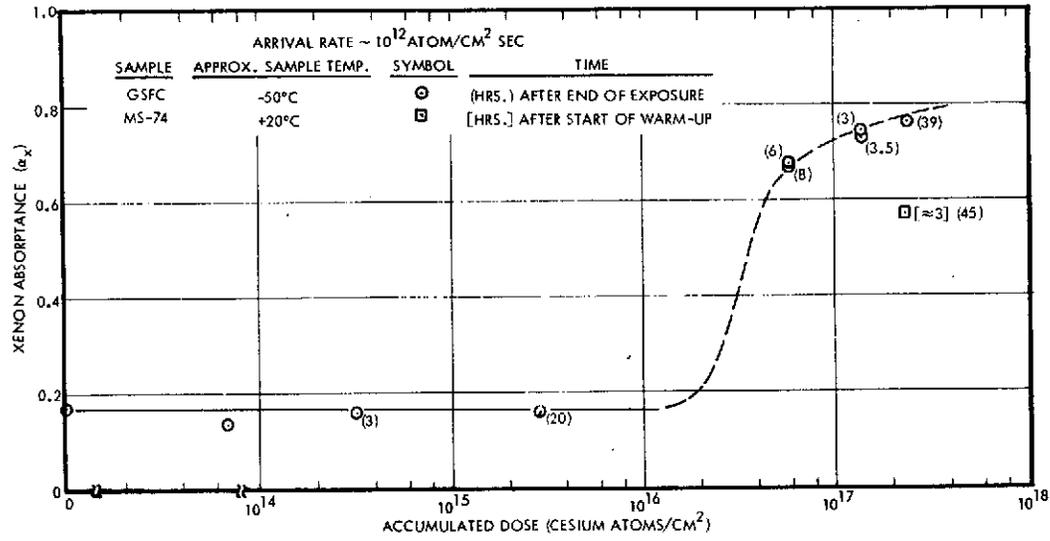
Figure 5-5.   GSFC MS74 White Paint Xenon Absorptance Degradation
at -50°C and at -50°C (Repeat Run)
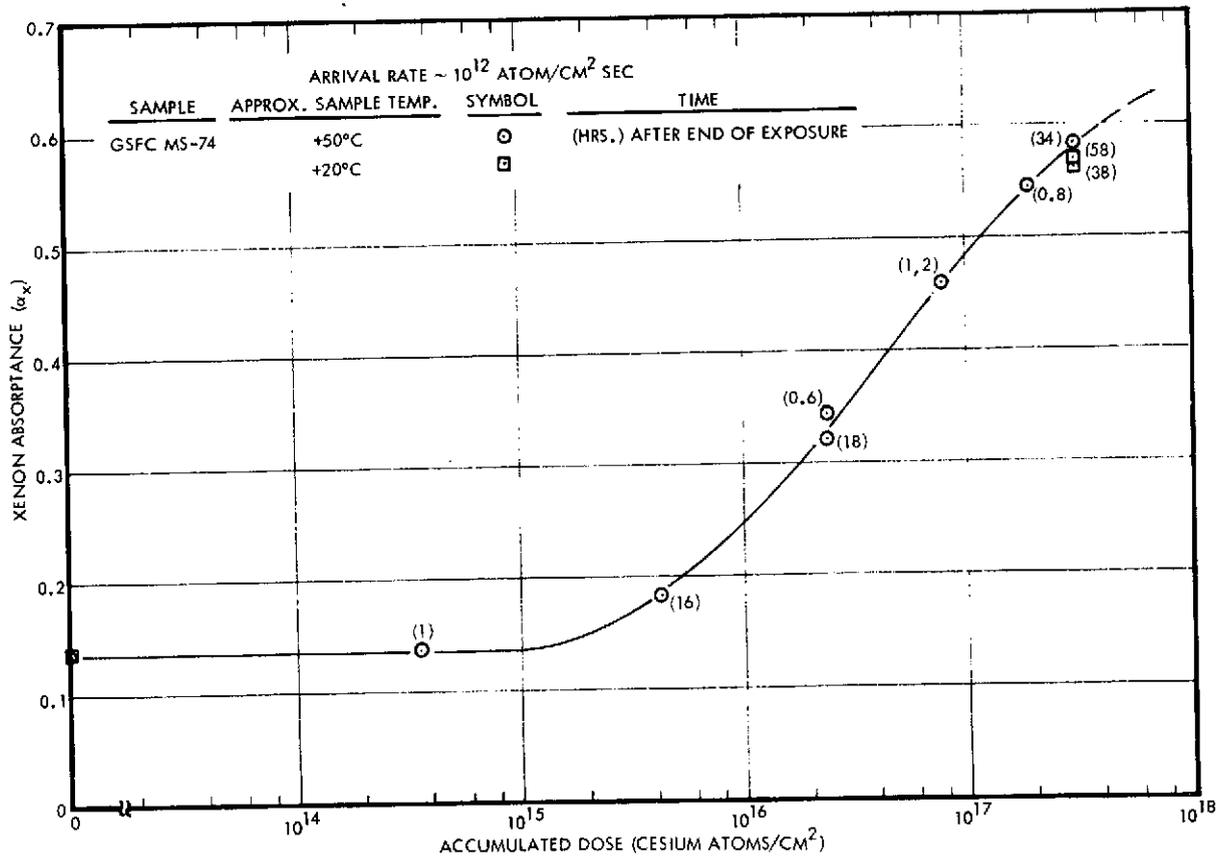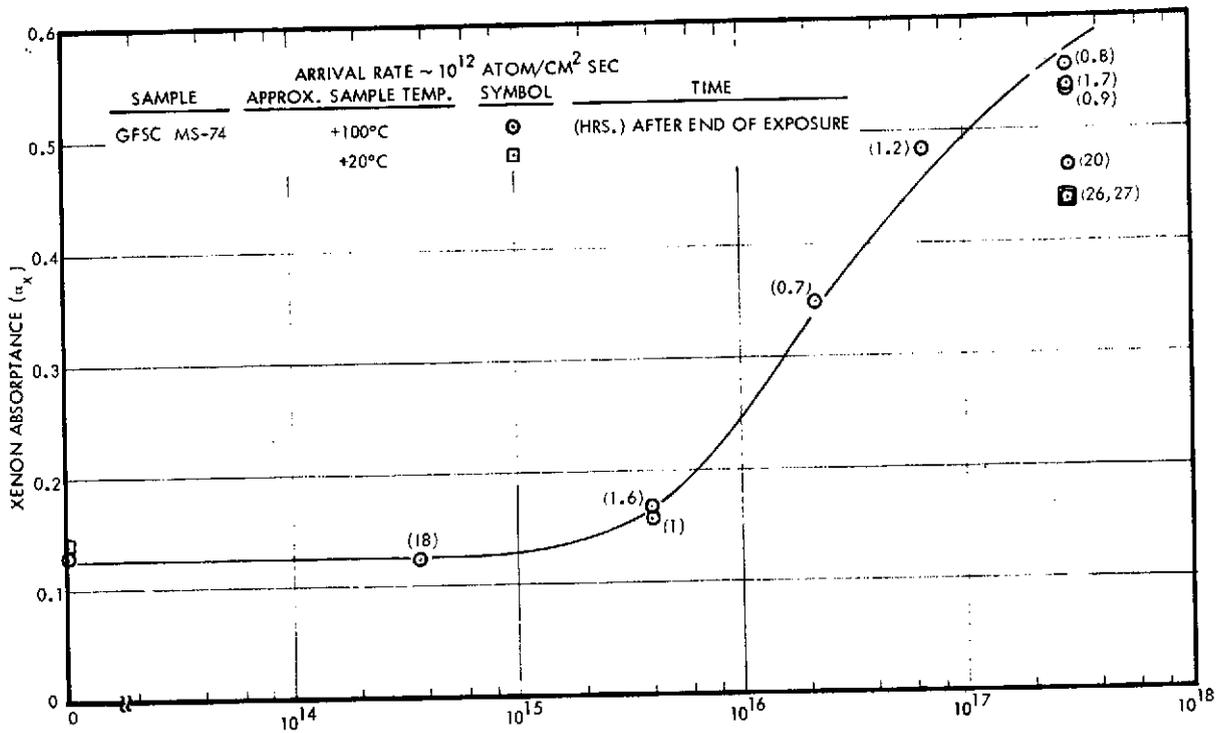
Figure 5-6. GSFC MS74 White Paint Xenon Absorptance Degradation at +50°C and +100°C by Cesium Atoms
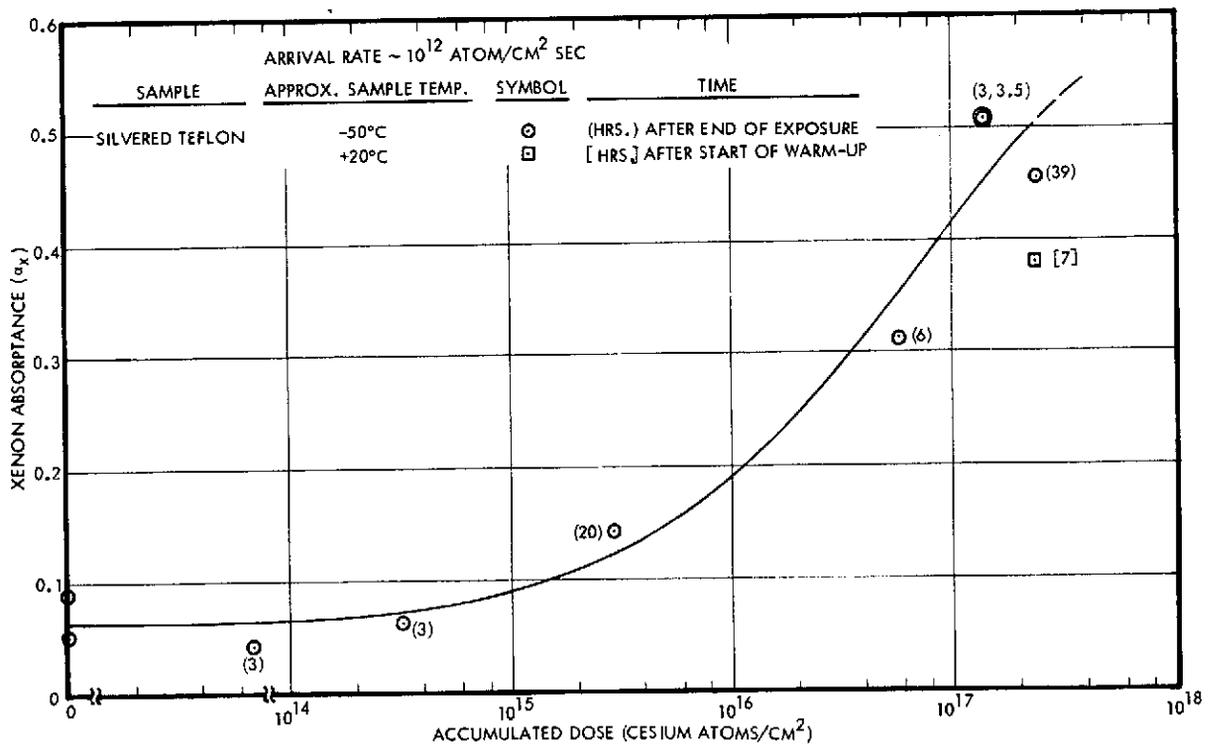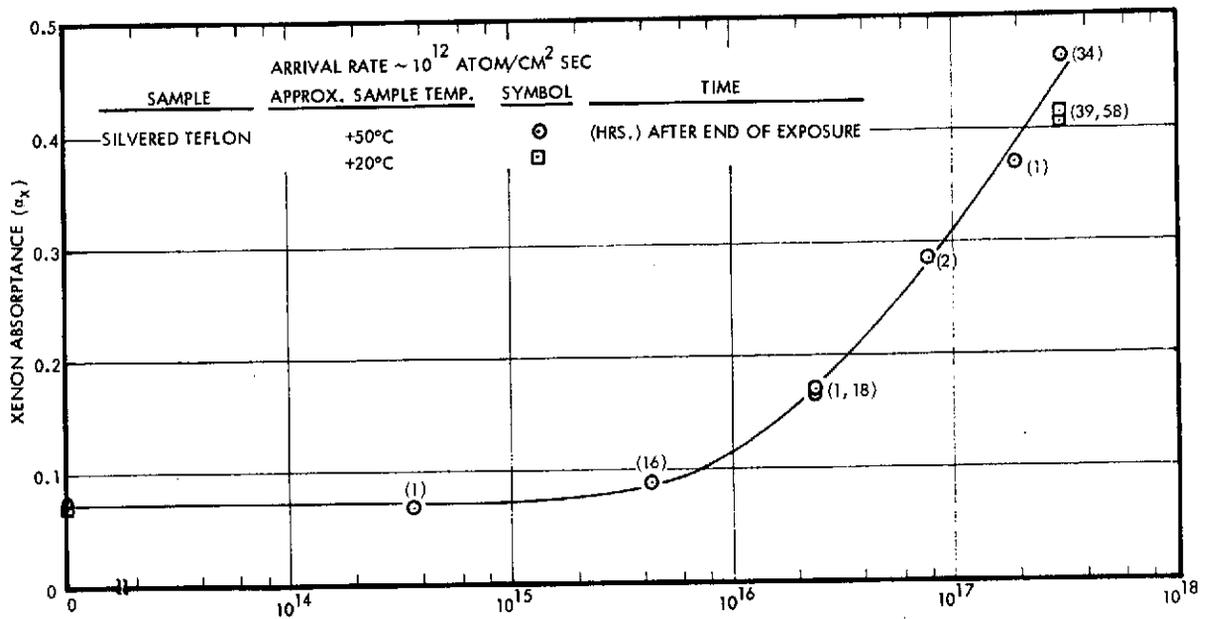
Figure 5-7. Five Mil Silvered Teflon FEP Xenon Absorptance
Degradation at -50°C and +50°C by Cesium Atoms
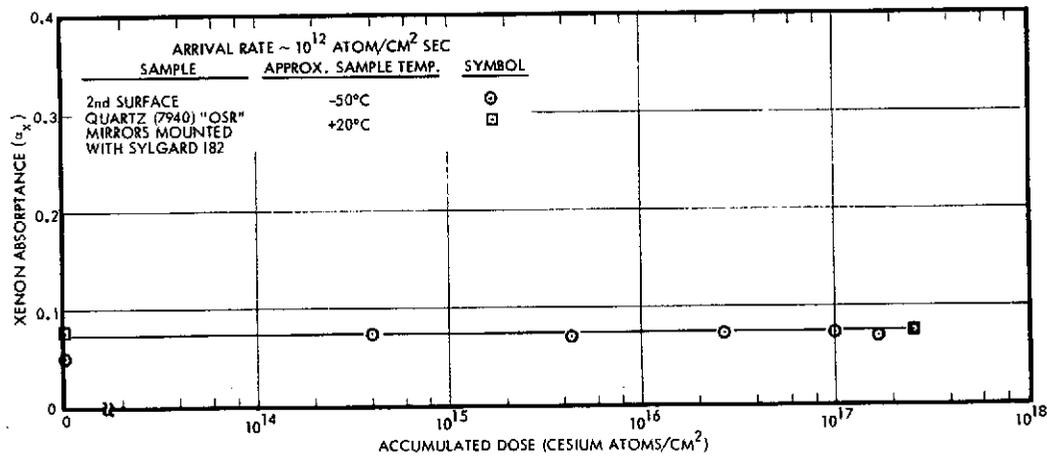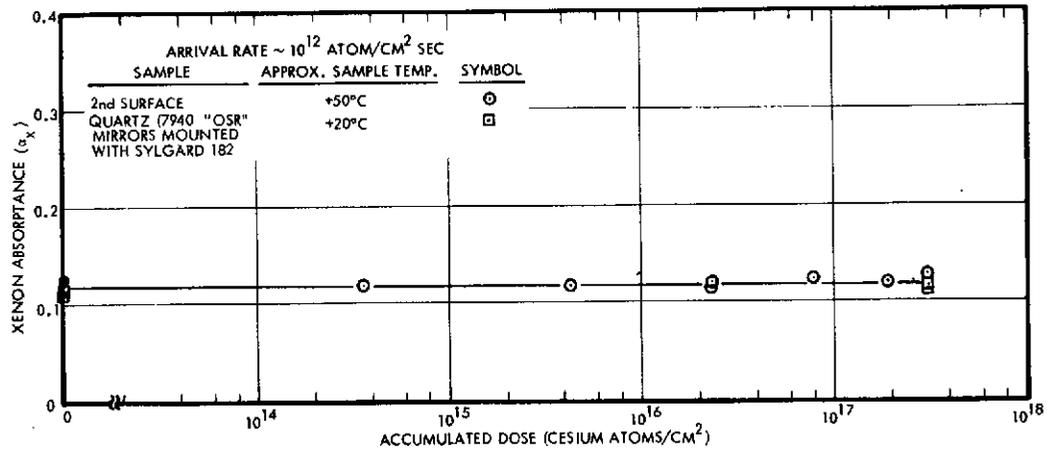
Figure 5-8.   OSR Xenon Absorptance Degradation
at -50°C and +50°C by Cesium Atoms
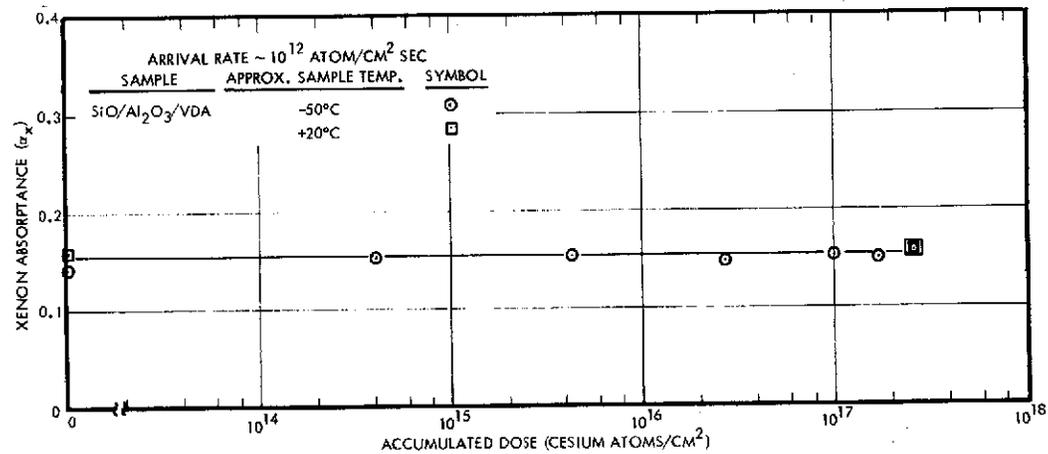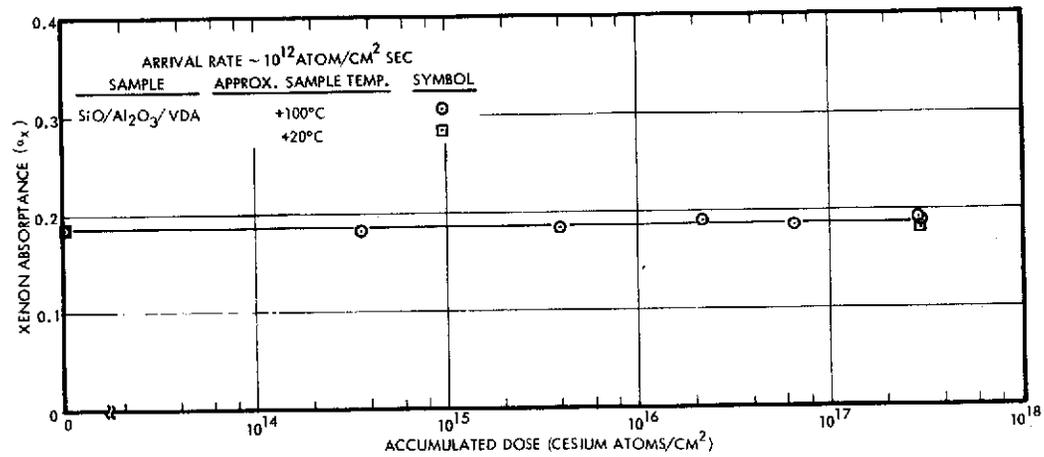
Figure 5-9. Al$_2$O$_3$/SiO$_2$/VDA Xenon Absorptance Degradation
at -50°C and +100°C by Cesium Atoms
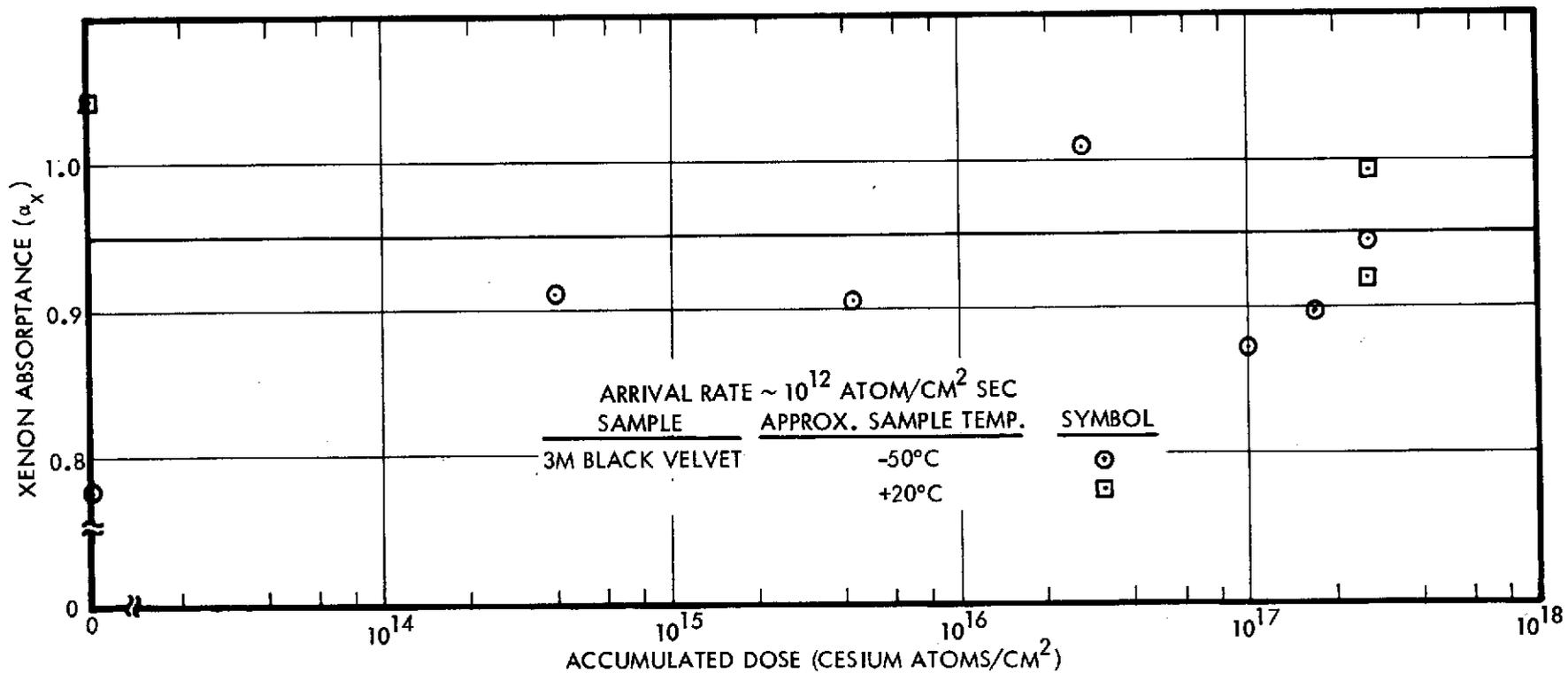
Figure 5-10. 3M 401 C10 Black Velvet Paint Xenon Absorptance Degradation
at -50°C by Cesium Atoms

the cesium tests. From the data, it is apparent that there is a consistent heat leak for this position which is significant at low temperatures. As explained in Section 4, a fixed heat leak does not affect the α_x values measured.

These difficulties with the low temperature emittance data are not of major concern, since never in the course of this work has emittance of a sample been affected by exposure to ion or atom beams.

5.3.1 Z93 White Paint

Samples were exposed to cesium atoms at -50° and at +100°C. There was a dramatic difference in degradation at the two temperatures, as seen in Figure 5-1. The general trend agrees with cesium ion degradation; i.e., greater degradation and onset of degradation at lower accumulated doses with lower sample temperatures. The cesium atom exposures were continued to accumulated doses nearly an order of magnitude higher than the cesium ions. The results of the cesium atom exposure on Z93 absorptance have also been plotted on Figure 5-11 which was extracted from previous work (Reference 3) with mercury ions. For reasons unknown, the quantitative degradation values agree quite favorably with the Hg^+ tests when temperature variations are considered.

The Z93 paint exhibited a significant annealing of degradation at the ends of the two exposure sequences. This effect was particularly evident at -50°C (Figure 5-1). The numbers in parentheses beside data points are the times, in hours, that the data were taken after a cesium exposure was stopped. The numbers in brackets are the elapsed time from start of sample warm-up until the data were taken. The -50°C sample registered a very high absorptance value ~70 hours following the end of its final exposure while it was still at low temperature. It appeared black to the eye when viewed through the lamp-sighting telescope. However, after the Z93 sample was returned to ambient temperature ($\simeq$20°C), the absorptance rapidly decreased and had nearly returned to its initial value 20.6 hours after warm-up was initiated. When the samples were removed from the vacuum chamber they appeared slightly yellowed.
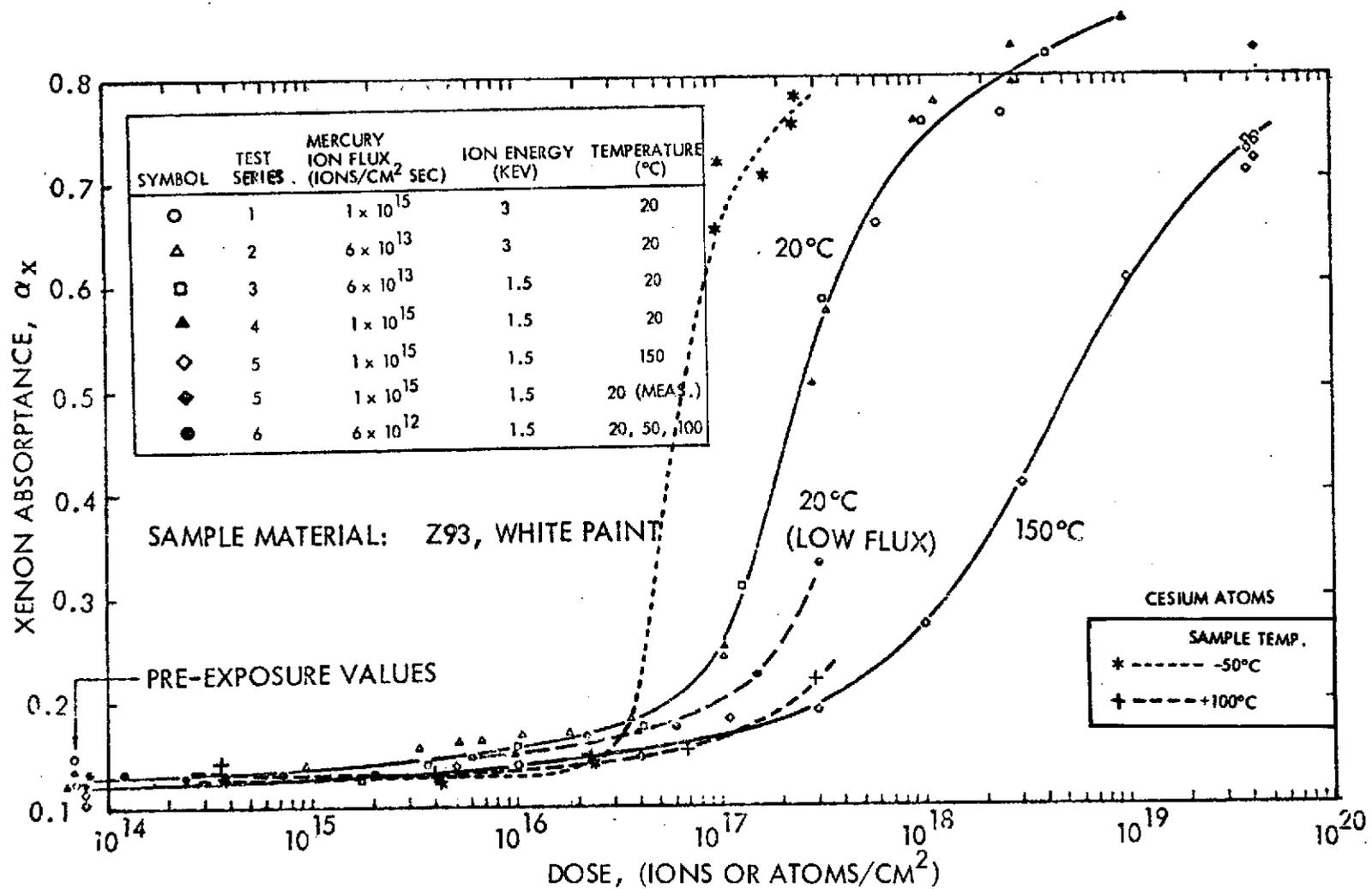
Figure 5-11. Comparison of Z93 Absorptance Degradation by Mercury
Ions (Reference 3) and Cesium Atoms

5.3.2 DC 92-007 White Paint

This Dow Corning silicone rubber base paint was exposed at -50°, +50°, and +100°C. The data appear in Table 5-3 and Figure 5-2. The -50°C sample began to show significant degradation at 2×10^{17} atoms/cm^2. This damage was completely healed within 5 hours after start of sample warm-up to 20°C. The +50° and +100°C samples did not exhibit degradation with atom doses up to 3×10^{17} atoms/cm^2.

5.3.3 Aluminized Kapton

Second surface aluminized 5 mil Kapton exhibits strongly temperature-dependent degradation characteristics as shown in Figure 5-3. The cesium atom results are in good quantitative agreement with the cesium ion results with respect to temperature and dose dependence, but greater degradation occurred since higher accumulated doses were achieved. No significant degradation occurred at -50°C even at doses of 2×10^{17} atoms/cm^2, while measurable degradation was first noted at doses of $\simeq 4 \times 10^{15}$ atoms/cm^2 for the sample at +50°C. The damage to the 50°C sample did not heal; on the contrary, absorptance values seemed to have increased slightly with "soak" time following an exposure. When removed from the vacuum chamber the sample had a lighter, more gold appearance than the amber color of unexposed samples.

5.3.4 Polished 6061 Aluminum

The "polished" aluminum samples (suspected to be Vacuum Deposited Aluminum (VDA) on an aluminum substrate) appeared to be unaffected in xenon absorptance after exposure to cesium atoms (Figure 5-4). The data for the 100°C exposure is very consistent and agrees quantitatively with previous measurements. The -50°C data, however, are widely scattered and higher than previously measured. This sample was placed on the one sample holder position which is "noisy" especially at low temperatures and low supplied heat fluxes. The -50°C sample was seen (through the telescope) to condense cesium on a spot ~1/9 the total sample area. However, its presence did not appear to affect measured thermophysical properties. In light of all other data taken to date, it is felt that the material remained unchanged after exposure to cesium atoms.

5.3.5 MS74 White Paint

The GSFC MS74 white paint exhibited greater degradation from cesium atoms than from cesium ions at all test temperatures. At -50°C, significant degradation occurs at about 5×10^{16} atoms/cm^2 as shown in Figure 5-5. These plots represent separate samples tested in two different test series, both at -50°C. This duplication of nominal test conditions provided a rather satisfying similarity in the test results. The exact onset of major degradation is not well defined in the earlier of the two -50°C tests, because such a marked change in degradation rate was not anticipated. Therefore, artistic license was used to generate the shape of the upper curve in Figure 5-5. Accumulated doses of more than 10^{17} atoms/cm^2 seem to result in absorptance values which are saturating in the range 0.8 to 0.9. At this point internal multiple reflections approach zero, and Fresnel reflectance occurs at the interface between air or vacuum (n=1) and the coating (n≈2).

At temperatures of +50° and +100°C, the MS74 begins to show degradation at lower doses (~5×10^{15} atoms/cm^2), but the apparent rate of degradation is less than at low temperatures (see Figure 5-6). This temperature dependence is probably related to thermal annealing which occurs within the material. It appears that there is little or no annealing occurring as long as the samples remain at -50 C. When the sample is returned to room temperature, however, rapid annealing occurs, as shown in the rectangular data points of Figure 5-5. By the time the samples were removed from the chamber, they had reverted to a near white appearance from the near black appearance immediately after cessation of cesium exposure. The high temperature data did not exhibit such a dramatic change in properties after cessation of exposure since the samples had been at elevated temperatures during exposure. All of the MS74 samples appeared slightly grey after the samples were removed from the vacuum chamber.

5.3.6 Silvered Teflon

The 5 mil Teflon FEP, silvered on the rear surface, begins to degrade at lower doses at -50°C than at +50°C (see Figure 5-7). However, this judgment of earlier degradation at low temperature is based upon a

single data point and may not be conclusive. In general, the degradation was greater after cesium atom exposure than after comparable cesium ion doses. There was some evidence of annealing as a function of time. While the samples were in vacuum at test temperature, there was a visible "gold" appearance which was fairly uniform in coverage across the sample. After return to atmospheric pressure, the sample returned to its original appearance, but there appeared to be an "oily" residue on the surface of the sample which could be removed with alcohol.

5.3.7 OSR Mirrors

The quartz second surface silvered (OSR) mirrors once again proved completely stable during the test exposures. The samples used for cesium atom exposure were fabricated from 3/4-inch by 3/4-inch square mirrors and were cemented to an aluminum substrate with Sylgard 182. They had significant cracks and gaps between mirrors, which accounts for the unusually high absorptance (for SSM's) obtained in the +50°C test. The data for the mirrors are plotted in Figure 5-8.

5.3.8 $Al_2O_3/SiO_2/VDA/Polished Aluminum$

The multilayer deposited coating $Al_2O_3/SiO_2/Vacuum$ Deposited Aluminum data are presented in Figure 5-9 for sample temperatures of -50° and +100°C. This material was very stable on exposure to cesium atoms as it was to cesium ions.

5.3.9 3M Black Paint

The 3M 401 C 10 Black Velvet Paint showed wide scatter in the data due to its placement on the sample holder at the "noisy" channel (see Figure 5-10). There are sufficient data, and visual observation, to conclude that no change occurred in the 3M Velvet Black Paint sample after exposure to cesium atoms.

5.4 SUMMARY AND CONCLUSIONS

The low α/ϵ thermal coatings exposed to cesium atoms all exhibited significant degradation of xenon absorptance with two exceptions: quartz second surface silvered mirrors and the multilayered $Al_2O_3/SiO_2/VDA$. Z93, DC 92-007 and MS74 white paints and second surface mirrors made from Kapton and Teflon degraded more after exposure to atoms than after

comparable doses of cesium ions. This particular conclusion should be de-emphasized somewhat, since the previous cesium ion exposures were not carried out to doses as large as in the present investigation. It was the very large doses of cesium atoms which caused significant degradation. Quartz second surface silvered mirrors, multilayered $Al_2O_3/SiO_2/$ VDA, "Polished" aluminum and 3M 401 C 10 Velvet Black paint did not measurably change due to cesium atom exposure.

Temperature effects were significant for the coatings which did degrade. Z93 degraded at lower doses when held at -50°C than when held at +100°C. Early onset of degradation at lower doses occurring at lower temperatures was also true for DC 92-007 white paint, MS74 white paint and silvered Teflon. Only the second surface aluminized Kapton sustained greater degradation at the higher test temperatures.

It is not obvious why Kapton has the opposite temperature dependence from the other four samples. Kapton has been shown to react chemically with bulk quantities of cesium when immersed in the liquid metal[2], but so has Teflon FEP. In contrast, Z93 and materials similar to DC 92-007 and MS74 did not show evidence of reaction in the immersion tests. Perhaps cesium has a greater desorption energy from Kapton than from the other samples, so increased temperature still permits long desorption times while decreasing the average time required for a cesium atom to react with the absorbent.

The exact nature of the degradation mechanism in the white paints is not clear. Tests to evaluate thermal annealing effects definitely showed that degradation which was time-stable at -50°C (within test times used) was annealed by returning the samples to +20°C while still in vacuo.

In summary, the cesium atom exposure tests have shown that certain thermal control coatings exhibit significant degradation of absorptance when exposed to large doses of cesium atoms. It also appears that any thermal control materials considered for use where they may be impinged by cesium atoms or ions should be tested to determine degradation effects. In situ property determination was a critical feature of these tests, as they permitted detection of temperature-related healing.

6. CESIUM VAPOR EXPOSURE

6.1 INTRODUCTION

Section 5, above, reports on experiments in which cesium atom beams were generated by evaporation from the surface of the porous tungsten ionizer. The tungsten surface was heated to operating temperature (about 1500°K), but no voltages were applied to the accelerator grid, and cesium vapor was supplied to the tungsten as for the generation of ion beams. In those experiments, the thermophysical properties of selected spacecraft samples were measured while the samples remained in the vacuum environment, and some measureable changes were detected in some samples after threshold dosages of cesium had been received. In another set of experiments reported in this section, additional cesium vapor exposure tests were performed on samples of other spacecraft materials which do not lend themselves readily to installation in the usual test facility or to measurements of thermophysical properties in the usual way. The objective of these tests was to obtain at least qualitative observations of the effects of cesium vapor on these materials to ascertain, in particular, if unexpected chemical reactions would occur which might change the mechanical or electrical properties of these materials.

A special cesium vapor chamber which was designed and constructed for this study is described below. The list of sample materials used in this task is also given along with an account of the tests and results.

6.2 CESIUM VAPOR EXPOSURE CHAMBER

The cesium vapor exposure chamber is shown schematically in Figure 6-1. It comprises a small sample-holding chamber to which cesium vapor is supplied from an electrically heated boiler. The chamber is connected through valves and suitable plumbing to vacuum pumps as shown, and is enclosed in a controlled-atmosphere dry box which is normally maintained at one atmosphere pressure of dry nitrogen. A major design consideration for this system is that of allowing individual samples to be either put in the system or removed for inspection without disturbing other samples being tested or exposing them to air. The exposure chamber can be either evacuated or back filled with dry nitrogen through a stainless steel bellows valve. When access is desired, the exposure
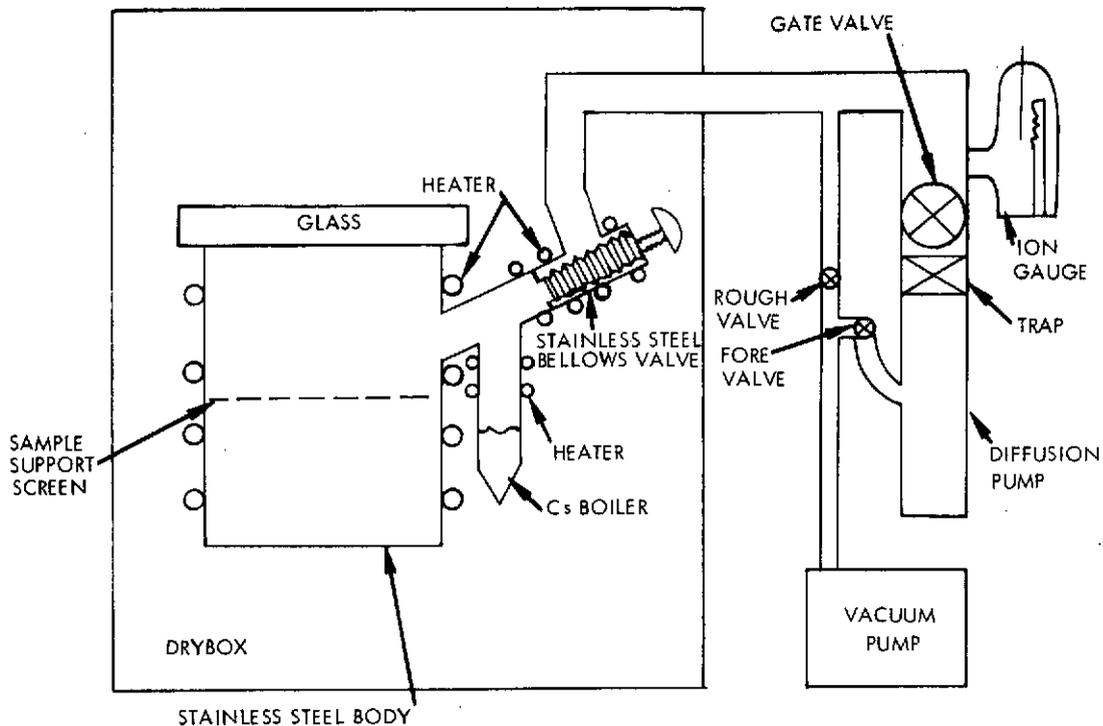
Figure 6-1.   Cesium Vapor Chamber Design

chamber is filled with dry nitrogen and the cover plate removed manually using rubber glove feedthroughs.   The samples can then be manipulated in a nitrogen atmosphere.

The cover plate is made of glass in order to allow visual observation of the samples.   The system is designed to be operated so that the cesium boiler is the coldest part of the system, and thus the cesium vapor pressure and arrival rate will be controlled by the boiler temperature.   A metal heater plate can be placed over the glass cover to maintain a high glass temperature.   Small sight holes in the heater plate allow visual observation during operation.   The samples and chamber are maintained at approximately 100°C.   The boiler temperature is varied between 50° and 95°C depending on the desired cesium arrival rate.   A nominal boiler temperature of 50°C can be obtained by using house hot water.   If this is inadequate, additional heating is added to the line.   The main advantage of controlling boiler temperature in this manner is the ability to adjust boiler temperature rapidly and precisely.   In switching from hot to cold water or vice versa, this boiler temperature readjusts at an initial rate of 1°C per second and is almost at equilibrium in 1 minute.

Figure 6-2 is a view of the cesium vapor chamber. The cesium boiler is shown lying alongside and just below the flare fitting to which it mounts. Before it was installed in the dry box, the chamber was wound with heating tape. The entire assembly was then wrapped with an insulating blanket about 1-inch thick. Construction of the vapor chamber and all high-vacuum lines uses stainless steel and heliarc welding. Figure 6-3 is a photograph of the stainless steel dry box used for this experiment. Visible in this photo are:

    a)   The rubber gloves for internal manipulation of the vapor changer and samples

    b)   Electrical heater, water line, and thermocouple connector plate

    c)   Viewports

    d)   Stereo microscope for close observation of samples

    e)   Pressure gauges for the drybox and air interlock

    f)   Air interlock for access to the drybox
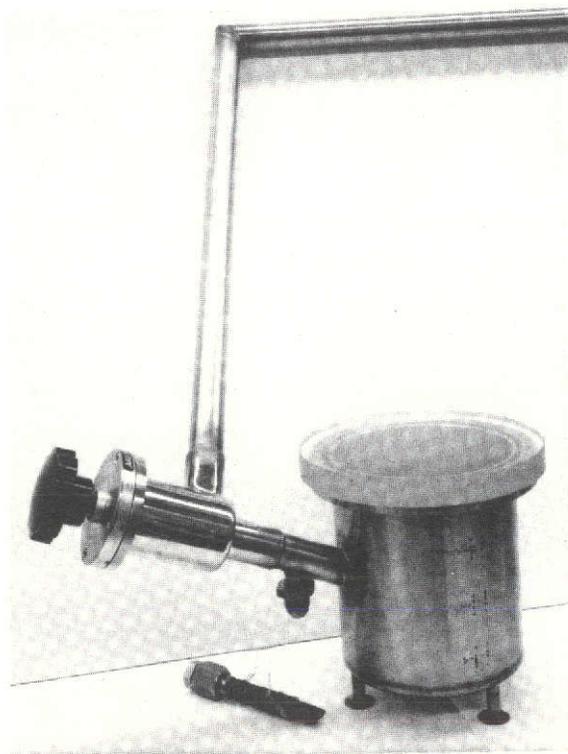
Figure 6-2. Cesium Vapor Chamber and Boiler
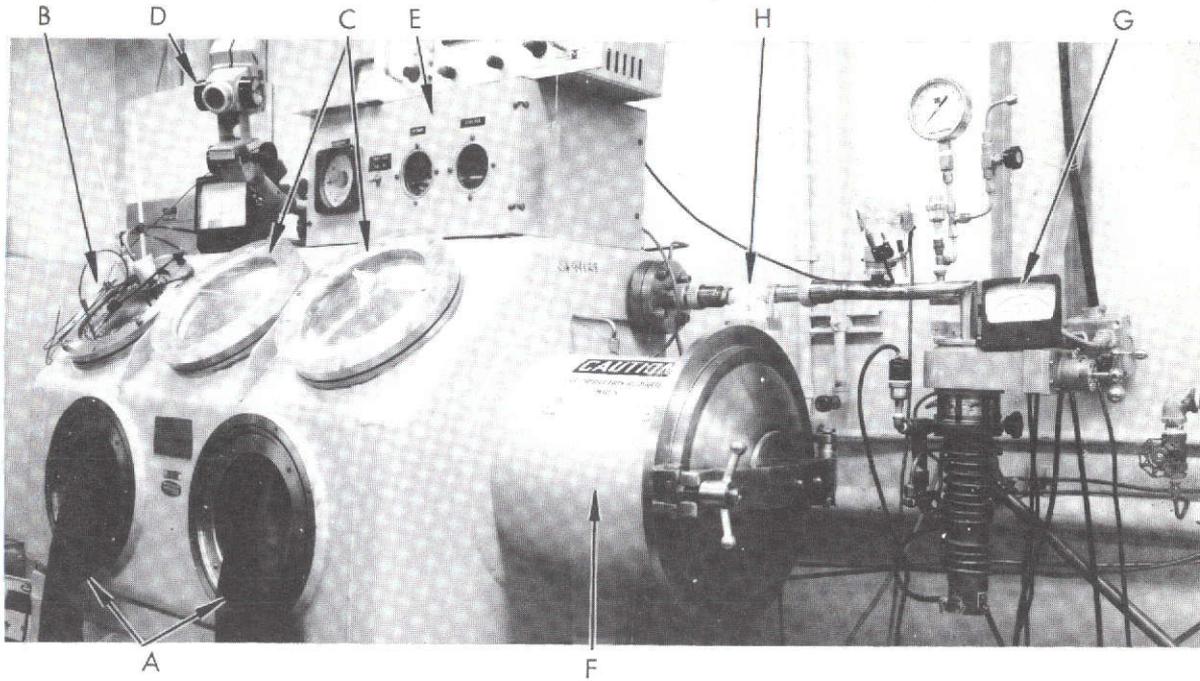
Figure 6-3.   Dry Box with Auxiliary Vacuum Pumps and
Instrumentation for Cesium Vapor Exposures

g)   Diffusion pump with gauges

h)   Liquid nitrogen trap

At the right side of the figure are the vacuum diffusion pump and associated plumbing into the vapor chamber. The liquid nitrogen trap is partially visible behind the top of the air interlock door. Pumping speed of the diffusion pump is 100 liters per second. Typical vacuum pressure as measured on the ion gauge between the trap and the pump is in the 10^{-6} torr range.

6.3 CESIUM VAPOR EXPERIMENTS

The cesium vapor chamber was checked in a preliminary test run using samples of Teflon, nylon and metalized Mylar. After a rather prolonged exposure to cesium, only the metalized Mylar was noticeably different, showing some signs of embrittlement.

In these experiments, the cesium vapor is approximately in equilibrium with a liquid cesium interface in the boiler. Hence, the exposure condition differs somewhat from that in the cesium atom beam exposures of Section 5. Atom number density is likely to be greater in the vapor

chamber than in the atom beams, but the "rms" atomic velocity is less than half of that of the "hot" atom beam, and the velocities of arriving atoms are randomly directed, rather than being directed normal to the sample surfaces. Also, inasmuch as the sample temperatures will be in equilibrium with the chamber walls and therefore hotter than the cesium boiler, the assumption is made that cesium will not condense on the sample, but can only be retained through chemical reaction with the sample material. Since cesium compounds are relatively stable, exposure to dry nitrogen should not change the properties of the reacted material.

Sufficient sample material was found to make six packages of space-craft materials of interest. Each package included the materials listed in Table 6-1. One set served as reference for the other five.

Table 6-1. Cesium Vapor Exposure Sample Set

Sample Identification	Material
(G)	Kapton H Film
(N)	Solder, 60-40
(III)	Kapton Tape, Mystick
(GGG)	Nylon, "Ty-Rap"
(FFF)	Teflon, "Ty-Rap"
(Z)	Sylgard #182 (clear in color)
(MM)	Aluminized Teflon #45
(UU)	Aluminized Mylar (thermal blanket) 1/4-mil thick
(BBB)	Nylon Net #48 (0.007-inch nylon mesh)
(HHH)	Silastic 140 (yellowish in color)
(QQ)	Dacron Mesh (copper coated)
(EEE)	Coaxial Cable, Teflon Insulator (tan outside)
(DDD)	Wire, Polyalkene Insulation (small white wire and bent in V-shape)
(CCC-1)	Insulating Wire (about 14 gauge) Fluorocarbon/ Polyimide (white in color) solid copper shield around strands
(CCC-2)	Insulating Wire, Polyimide Insulation (copper color with white tracer)
(CCC-3)	Insulating Wire, Polyimide Insulation (two conductor shielded coaxial)
(XX)	Fiberglas reinforced epoxy (black in color)

One set of samples was placed in the chamber and exposed to cesium vapor for a duration of 114 hours. Four temperatures were monitored during this time: (1) boiler temperature, (2) chamber lid temperature, (3) chamber wall temperature, and (4) chamber bottom temperature. Boiler temperature was typically 83°C; the others were 96° to 105° for the lid, 127° to 138°C for the wall, and 120° to 130°C for the chamber bottom. At the end of this run, the following samples exhibited no visible damage:

> Kapton H-Film
> Solder 63/37 (except for loss of flux)
> Kapton Tape
> Teflon Ty-Rap
> Nylon Net
> Silastic 140
> Dacron Mesh (copper coated)
> Fiberglas Reinforced Epoxy (black)

The aluminized Teflon appeared to have melted in the area of contact with the stainless steel screen upon which it was resting. After exposure, it also contained some black spots. (Maximum temperature was 138°C.)

All other samples exhibited a slight yellowing which may have been due to vaporization of the 63/37 solder flux.

In a retest of affected cesium vapor exposure samples, the following materials from a new set of samples were exposed to cesium vapor for 117 hours at a flux density (equilibrium flux density across a cesium liquid-vapor interface) estimated to be on the order of 2×10^{16} atoms/(cm^2 sec):

Sample	Material
GGG	Nylon Ty-rap
Z	Sylgard #182
MM	Aluminized Teflon
UU	Aluminized Mylar
EEE	Coax Cable - 303/U
DDD	Insulated Wire

Sample	Material
CCC-1	Insulated Wire
CCC-2	Insulated Wire
CCC-3	Cable, 2-conductor Shielded

As before, the MM sample quickly curled up into a cylinder upon application of heat (maximum temperature less than 100°C) and partially uncurled on cooling, and was somewhat stiffer than originally. There was a light brownish tinge to the white insulation of sample DDD. All other samples appeared normal. As a check on this result, corresponding samples from sample set 5 were heated in a laboratory oven at atmosphere for 98 hours at 100°C. After this exposure, sample MM had been affected as above, and slight yellowing was observable on some of the wire insulations; otherwise all samples were unaffected. Accordingly, it would seem that the effects observed after the 117-hour exposure to cesium had, in fact, been the result of high sample temperatures. Also, the identity of sample MM is called into question, inasmuch as Teflon should not have melted at the temperatures to which the sample had been raised.

In view of the relatively low cesium boiler temperature (90°C) used in these experiments, confirmation was sought that the actual vapor pressure of cesium during exposures was as expected. Three attempts were made to seek this confirmation.

Cold Tongue

An aluminum plate cover was made for the cesium vapor chamber. A glass window was provided for the cover and a loop of small copper tubing was located under the cover so that it would be visible through the window and so that it could be chilled with running water during an exposure. With the chamber held at the usual temperature (about 90°C) and with tap water at about 20°C in the tube, no cesium condensation could be seen on the tube at boiler temperatures below 125°C, although condensed cesium was readily observed for boiler temperatures at or above 130°C.

Sample Exposures during Condensation

This result suggested that samples should be exposed at the same time as cesium condensation was observed on the copper tube. A set of samples was installed and left to warm up overnight. By the next day,

the chamber temperature had reached 128°C, although the boiler was kept chilled. The chamber was cooled to 95°C and the boiler heated. Again, condensation was observed on the copper tube at a boiler temperature of 140°C. The experiment was left in this state over the next night. The following morning, the boiler was cooled, hot water (40° to 45°C) was put through the condensation loop, and the experiment was left until the next morning. By this time very little cesium had been evaporated from the copper tube. The appearance of all samples as viewed through the window was normal. When the chamber was opened, there was some smoke generated as oxygen reached the condensed cesium, and at this point the samples darkened in appearance. The samples were removed, and the chamber and cooper loop were cleaned.

Ionization Gauge Check

A nude ionization gauge was installed on the chamber cover so that the pressure inside the vapor chamber could be measured during a run. With the boiler chilled, the chamber was heated to about 140°C, then cooled to about 90°C and left overnight. On the next day, with the chamber temperature stabilized at 90° ± 2°C, a plot was made of chamber pressure as a function of boiler temperature. This result is shown in Figure 6-4. Also sketched in the figure is the vapor pressure curve for cesium in this temperature range. This is, admittedly, not a carefully controlled cesium vapor measurement (the gauge constant for cesium has not even been taken into account), but the result indicates that a measurable quantity of cesium vapor is being introduced into the chamber at temperatures below those at which a visible condensation occurs on the copper tube. This result, taken together with the lack of unusual effect on samples at the higher boiler temperature, helps to confirm the following conclusion relative to the cesium vapor experiments as a whole.

6.4 CONCLUSION

Selected samples of spacecraft structural materials have been exposed to cesium vapor for periods of time extending to the order of 100 hours, at vapor pressures on the order of 1×10^{-4} torr (and higher) and at sample temperatures on the order of 100°C (and higher). The
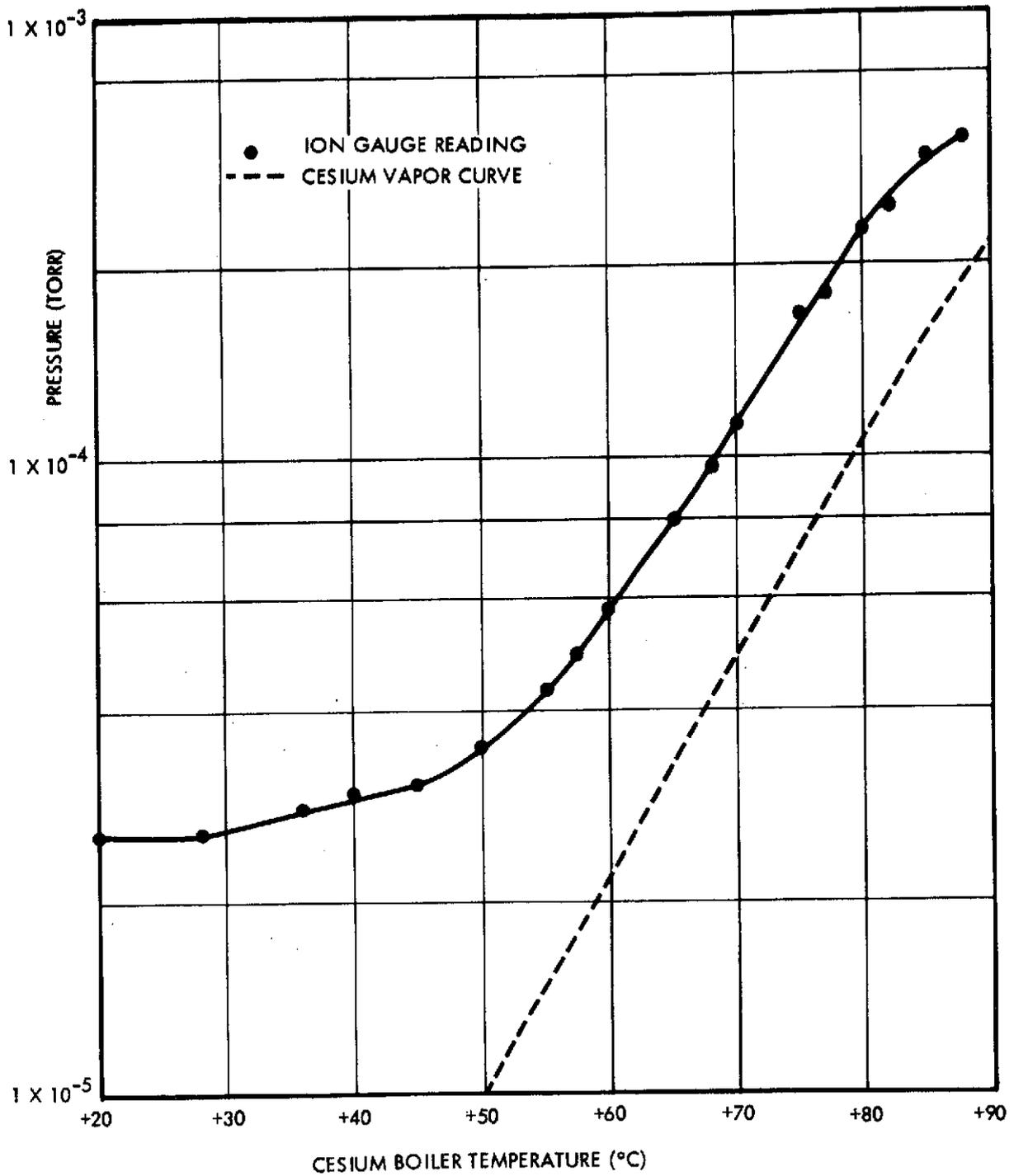
Figure 6-4. Vapor Chamber Pressure Versus Cesium Boiler Temperature With Chamber Temperature Held Constant

effects observed were only: (1) those which were predictable from considerations of chemistry (and were confirmed in cesium immersion tests or in cesium atom beam tests), or (2) those which were the result of the elevated temperature itself.

7. SIMULATED CHARGE-EXCHANGE ION EXPOSURE

7.1 TASK OBJECTIVES

The objective of the experimental work described in this section underwent an evolutionary process during preparations leading to the performance of experiments. Technical and contractual flexibility of all agencies concerned enabled this to proceed so that the principal objective of the ATS program could be served. Initially, the goal of this effort was to expose sample materials which were candidates for bombardment by the ion thruster beam to ion beams having the maximum energy (550 ev per charge) to determine possible degradation during the lifetime of the thruster experiment. Three candidate materials were chosen: (1) solar cells (to represent those on the solar panels), (2) a low reflectance lens coating sample (as used for anti-reflectance coating of the startracker lens), and (3) an aluminum spectral reflector (representing the radiometer cooler cone material). Inasmuch as one ion energy was to be used in these tests, the 550-volt value would correctly simulate ion impingement energy on the solar cells. The cooler cone and OSR surfaces will be shielded from direct view of the thruster. These two items would, at worst receive charge-exchange ion bombardment which would, in any case, do no more damage than predicted by a scaling of the high-energy ion bombardment results.

With respect to spacecraft design, it was thought possible to repel low-energy charge-exchange ions by biasing the thruster neutralizer so that the ion beam potential would be negative with respect to these surfaces. Hence, ions formed within the beam would be energetically prevented from reaching spacecraft surfaces. It seemed, therefore, inappropriate to test for the effects of these ions separately. When it became apparent that this biasing scheme would not work in the ATS-F case because of the short distance between the thruster exhaust plane and the nearest spacecraft surface, the emphasis of this task changed. An analysis, reported in the appendix to this report, had shown that 550-ev ion bombardment on the solar panels was likely to have negligible effects on the solar cells in any case. Inasmuch as low energy ions could not be prevented from impinging on spacecraft surfaces, it now became of primary

importance to evaluate the possible effects of these ions on the radiometer cooler cone, in particular.

7.2   TEST PROCEDURES

The ion source used in these experiments is the same unit described in Section 3.   Generally this source operates most uniformly at a current density yielding 10^{10} to 10^{12} ions per square centimeter per second at the surface of the test samples.   According to the original plan, samples of the three candidate materials were to be characterized as well as possible prior to the ion beam exposures.   They were then to be mounted on the sample holder for exposure to the ion beam.   Properties of the samples were to be measured at intervals during the exposure, with final characterization measurements to be made following the test.   Except for the change in ion energy which was required to simulate charge-exchange ions rather than primary beam ions, the tests proceeded as planned.

An essential difference between these tests and those reported in Sections 5 and 6 is that the properties to be measured were not the usual thermophysical properties, but rather what could be loosely termed the "transmittance" of the sample materials.   With respect to the solar cells, this was to relate directly to the electrical conversion efficiency for solar illumination; for the lens coating sample, it related to the ability of the startracker to sense the light from Polaris; and for the specular reflector sample, the relevant property was the ability to reflect far-infrared light into the north sky without scattering any of this heat energy back into the radiometer cold patch.   New measuring techniques were called for.   The following paragraphs describe, for each type of material, the specimens selected, pre-test measurements and results, and the instrumentation and test procedures used for measurements of significant properties during the course of ion beam exposures. Sample mounting is then described.   This is followed by a summary of the ion beam exposure runs, and the final results.

7.2.1 Solar Cell Samples

Following a study of the spectral quality of both solar illumination and light from Polaris, it was decided that the appropriate lamp to use for measurements of both the solar cell samples and the lens coating

sample during ion beam exposures would be a GE Type DXK "Uniflood" 650-watt lamp operated at a color temperature of 3400°K. The uniformity of the illumination provided at the sample holder position in the vacuum chamber was measured. With the intensity of illumination maximized at the center of the sample holder, the intensity was found to be down by 3.3 percent at ±3 inches in one axis, and by 1.4 percent at ±3 inches in the other axis. Accordingly, it was not deemed sufficiently uniform to illuminate all samples at once. However, the illumination was within 0.5 percent of peak value over an area of about 4 inches by 3 inches, which is larger than any individual sample. The lamp mounting provided for aiming the lamp at each sample in turn as measurements were made. Short-term stability of the lamp intensity was found to be adequate when the lamp was supplied from a constant-voltage ac regulator.

Several samples of individual solar cells and of sets of cells utilizing different types of solar panel construction were tested. After the samples were mounted to the sample holder, the electrical characteristics of all samples were measured by personnel of the TRW Solar Systems Department, Space Vehicles Division, using standard test equipment and procedures for characterization of solar cells as outlined in Figure 7-1. For each sample a curve was generated such as that shown in Figure 7-2. As a typical volt-ampere curve, it may be characterized by eight numbers: short-circuit (zero-voltage) current, open-circuit voltage, voltage and current at the point of maximum power, maximum power level, and the dynamic impedance (slope of volts/amps) at the three specified points. Generally, the small (2- by 2-cm) cells have open circuit impedances near 0.4 to 0.5 ohm and short-circuit impedances near 300 ohms, whereas the 2- by 4-cm cells have values of about 0.25 (OC) and 200 to 300 ohms (SS), respectively. Table 7-1 shows the list of samples tested and measured values for the more important characteristics of these samples.

During ion beam exposure, the measured property of the solar cell samples was the ratio of short-circuit current to that of a reference cell which was not exposed to the ion beam.

7-3

TEST EQUIPMENT

a) Light source: X-25 Solar Simulator (Spectrolab)

b) Digital Voltmeters, Model 3440, (HP)

c) X-Y Recorder, Model 7035 (Mosely)

d) Load, automatic (TRW)

e) Water Bath, Model 3210A (Blue M)

f) Std. solar cell, INT-HF-135 (TRW)

TEST PROCEDURE

a) Place calibrated standard cell into most uniform illuminated target area and adjust light intensity to 139.6 mw/cm^2.

b) Replace standard cell with test specimen assembly.

c) Using a level, assure that the specimen copper plate is perpendicular to the light rays.

d) Record the position of the specimen assembly with respect to the overall illuminated area.

e) Place the standard cell next to the specimen assembly.

f) Connect the pipes of the water-cooled copper plate assembly in series with existing cooling system.

g) Attach a thermocouple underneath the copper plate and adjust the water-bath temperature until the thermocouple reads 27°C.

h) Zero and calibrate digital voltmeters.

i) Connect first specimen and read and record the short circuit current, (I_{sc}) and open circuit voltage, (V_{oc}) as displayed on digital voltmeters, (DVM).

j) With the aid of the DVM, calibrate the X-Y recorders X- and Y- axis.

k) Plot I-V characteristic of specimen.

l) Repeat steps (i) through (k) for specimens #2 through #7, maintaining copper plate temperature and light intensity constant.

Figure 7-1. Equipment and Procedure for Pre-Test
Measurement of Solar Cell Samples
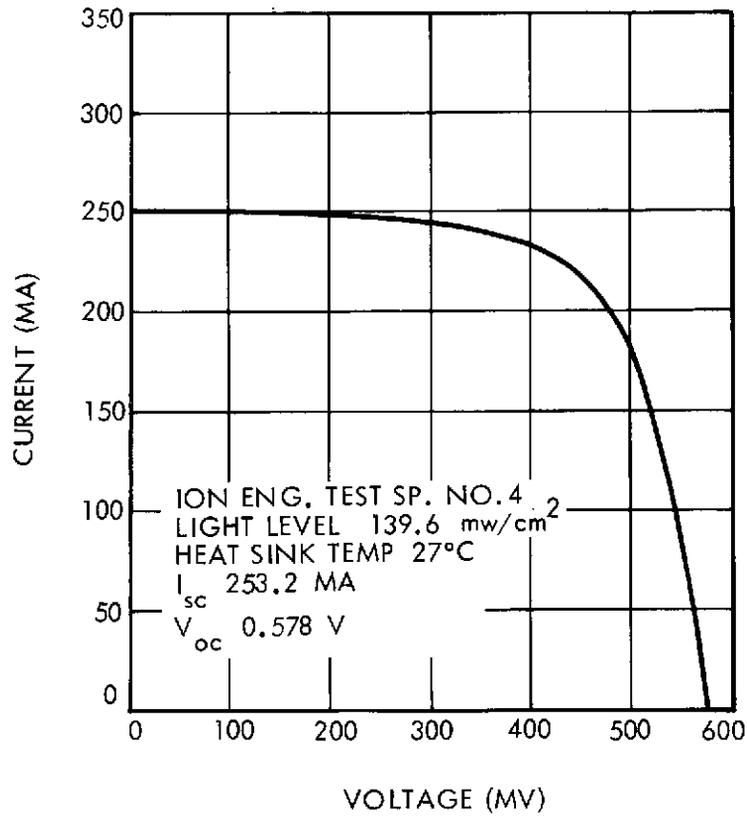
Figure 7-2.   Typical Solar Cell Volt-Ampere Curve

ION ENG. TEST SP. NO. 4
LIGHT LEVEL   139.6 mw/cm^2
HEAT SINK TEMP 27°C
I_{sc} 253.2 MA
V_{oc} 0.578 V

No.	Type	Cells	Size(cm)	Connection	V_{oc}(V)	I_{sc}(A)	P_m(W)	V_{mp}(V)	I_{mp}(A)	R_{mp}(Ω)
1	ATS-F Panel	4	2 x 4	series	2.311	0.2650	0.4440	1.850	0.240	8.33
2	Cell		2 x 2		0.590	0.1335	0.0572	0.477	0.120	4.17
3	FRUSA** Panel	6	2 x 2	3S2P*	1.719	0.2465	0.3020	1.340	0.225	5.41
4	Cell		2 x 4		0.578	0.2532	0.0984	0.460	0.214	2.12
5	Cell		2 x 2		0.595	0.1316	0.0572	0.485	0.118	3.79
6	Cell		2 x 2		0.586	0.1313	0.0561	0.480	0.117	3.96
7	Cell		2 x 4		0.590	0.2600	0.1058	0.460	0.230	1.89

*3-series, 2-parallel
**Flexible Roll-Up Solar Array

Table 7-1.   Solar Cell Samples: Solar Simulator at 139.6
mw/cm^2, Cells at 27°C

7.2.2. Startracker Lens Coating Sample

The startracker lens coating samples consist of two "witness plates" with coating numbers as follows:

Sample	Numbers
A	1109-6651, 1109-6648
B	1109-6656, 1109-6657

For each sample, both the transmittance and the sum of transmittance and reflectance were measured, before ion beam exposures, using a Beckman DK2A Integrating Spectrophotometer. The resulting chart records were then read to derive the ratios which are plotted as functions of wavelength in Figures 7-3 and 7-4. The results of these measurements necessarily include the effects of reflectance from the back surface of the plate. Since the witness plate is flat, it was impractical to devise an experiment for measuring the reflectance of the front surface, while at the same time discriminating between front and back surface reflections. It will be noted that, while the reflectance (difference between ρ and τ curves) is small for both samples, the absorptance is much higher in one sample than in the other. Accordingly, the sample designated "B" above was selected for the ion beam tests.

During ion beam exposures, the test specimen was mounted on the sample holder in such a way that it could be exposed to the cesium ion beam or moved into one of two positions for optical measurements. In the first of these positions, light from the illuminating source passed through the plate and into an integrating sphere, the illumination of which was measured by a photomultiplier tube. The function of the integrating sphere was to eliminate the effects of variations in sensitivity over the photodetector surface, and also to average light transmittance over the window surface. In the second measurement position, the plate was moved aside far enough that light from the illuminating source passed directly into the integrating sphere. The measured quantity was the ratio of illumination through the window to that received directly. Measurement of light intensity in the integrating sphere was made using an RCA Type 7767 photomultiplier tube having a 3/4 inch-diameter photocathode (end-on) with S-11 response and sensitivity of 13,000 amperes per watt at 1500 volts. The near ultra-violet emission of the
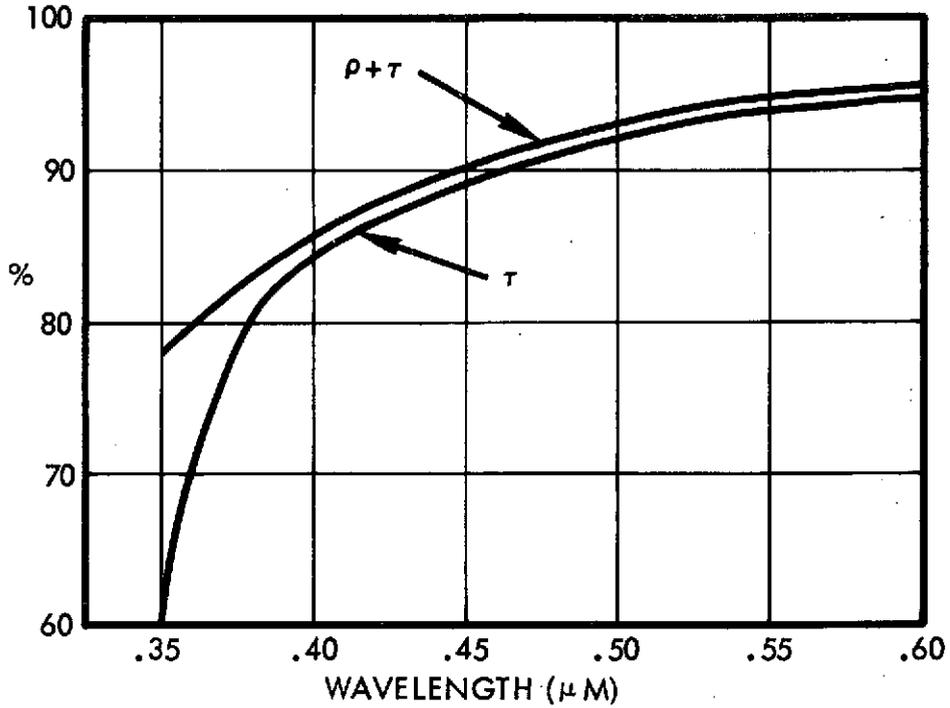
Figure 7-3.   Transmittance and Transmittance Plus
Reflectance for Witness Plate No.
1109-6651, 1109-6648
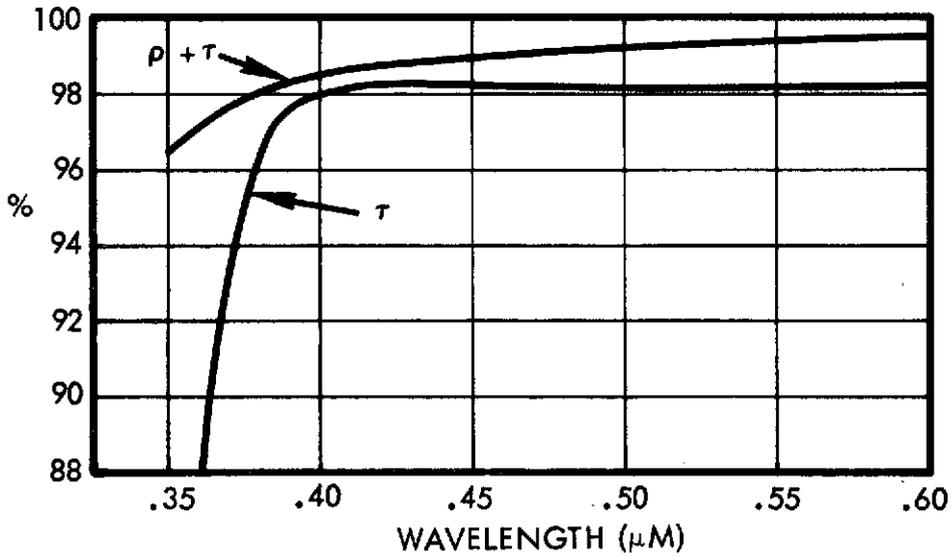
Figure 7-4.   Transmittance and Transmittance Plus
Reflectance for Witness Plate No.
1109-6656, 1109-6657

3400°K quartz-iodine lamp is sufficient at this temperature that the photo-tube response dominates the spectral range of the measurement, and adequately simulates the operational performance of the flight lens.

7.2.3 Specular Reflector Sample

The test specimen used for this measurement was the specular reflector No. QQQ supplied as one of five VHRR samples from the ATS-F program. Prior to ion beam exposures, initial total reflectance measurements were made of the specular reflector (radiometer cooler cone) sample in the wavelength range of 0.35 to 0.6μ m. In this range, the total reflectance is about 0.91. However, inasmuch as the working range of wavelengths for this surface is in the far infra-red, measurements were separately made of the specular and diffuse components of reflectivity in the infra-red band. Specular reflectance was measured at both 12 and 15 microns wavelength using a reflecting goniometer with tungsten lamp, KBr prism, and PbS detector. At a 15-degree angle of incidence, reflectance was 0.990 for both wavelengths. The diffuse component of reflectance was measured using the Gier-Dunkle Integrating sphere, with results as shown below for four typical wavelengths:

λ(m)	ρ (diffuse)
0.814	0.0058
1.002	0.0044
1.471	0.0023
2.168	0.0011

As with all the samples in this series, the reflector was mounted so that it could be exposed to the ion beam or moved into position for in situ reflectance measurement.

Measurement of the specular quality of reflectance of this sample, while it was still in the vacuum system, posed an unique problem which was approached as follows:

Helium-Neon Laser

The beam from a Spectra-Physics model 124A helium-neon laser was first passed through a spatial filter and collimating telescope from which it emerged with a diameter of about 2 inches. The telescope was focused so that the beam converged to a second focus at about 11 feet

from the laser. The beam initially was aimed at a first-surface mirror which could direct it either through a second spatial filter aperture at the second focal point outside the vacuum system, or through the vacuum window, toward the cooler cone sample. After reflecting from the sample, the beam emerged through the vacuum window and passed through an alternative aperture, again at the second focal point distance. Diameter of the second spatial filter apertures was 2.27 millimeters. In either case, the amount of light passing through an aperture was measured with a laser power meter located immediately behind whichever aperture was illuminated. With this geometry, light was reflected from a large fraction of the surface of the sample reflector so that the measurement was made insensitive to localized effects. A reduction in the reflectivity of the surface or an increase in scattering properties of the surface would both result in a decrease in the amount of light reflected from the sample through the second pinhole and into the power meter. For each measurement, the ratio was taken of laser light reflected from the sample into the power meter to that which traversed an equivalent distance of room air. A possible source of error in this measurement was, of course, the scattering and reflections from the surfaces of the vacuum window, if these effects did not remain constant in the series of measurements. A pair of readings could be taken in less than 5 minutes. Laser power stability was monitored separately and maintained within ±0.8 percent per hour by cooling the laser tube and mounting with an electric fan.

7.3 SAMPLE MOUNTING

The samples were mounted on a water-cooled copper plate which (as with earlier sample holders), could be rotated 180 degrees. In one position the samples faced the ion source; in the other they faced the quartz-iodine lamp and the laser beam.

Figure 7-5 is a photograph of the sample plate facing the light sources. The samples are identified as follows:

At 12:00 o'clock:	Specimen No. AAA-2 solar cell
At 2:00 o'clock:	Six 2- x 2-cm solar cells on Kapton (FRUSA panel)

At 4:00 to 5:00 o'clock: Specimen AAA-3 and AAA-4
                              respectively (reference solar cells)

At 6:00 o'clock: Sample WW witness plate

At 7:00 o'clock: Sample AAA-4

At 8:00 o'clock: Sample AAA-3

At 10:00 o'clock: Four 2- x 4-cm cells on honey-
                              comb (ATS-F panel)

At center: Specular reflector
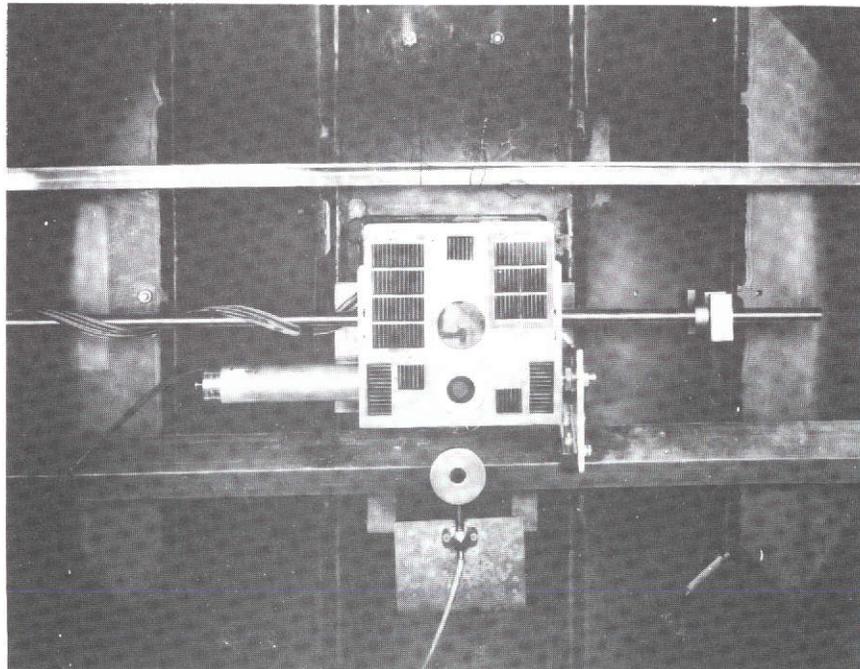
Figure 7-5. Sample Holder in Position for In-Situ
             Measurements

Figure 7-6 is a photograph of the sample plate facing the ion source.
The reference solar cells are located in the upper left quadrant behind a
copper plate which is clamped to the LN_2 cooled collector. The neutral
detector, shown above the entrance aperture, was not used in these
experiments. The 1/8-inch J_+ probe to the left of the aperture was used
to monitor beam intensity.

Figure 7-7 is a photograph from the light source end of the chamber
when the sample plate was facing the ion source. The integrating sphere
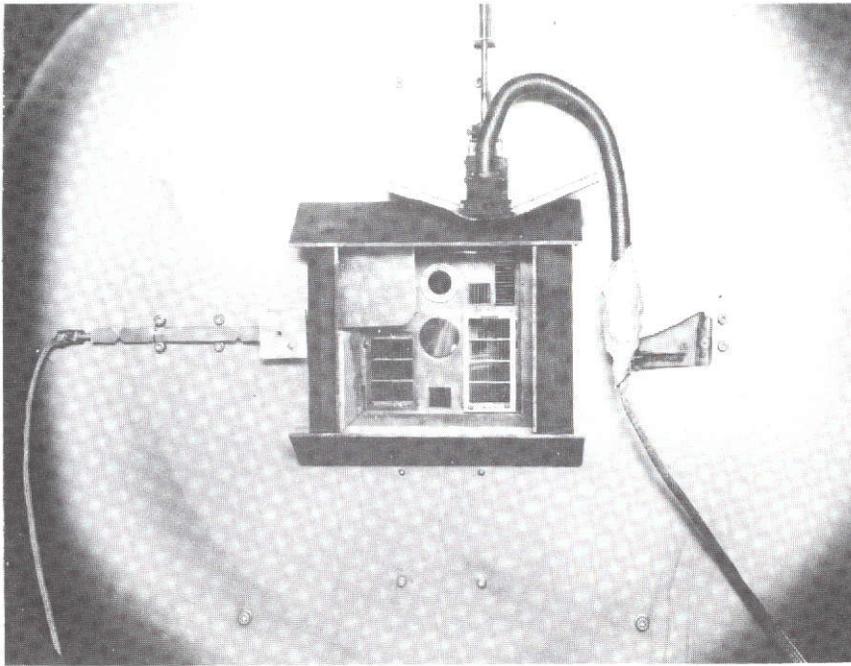
Figure 7-6.   View From Ion Source Showing Samples
in Position for Ion Beam Exposure
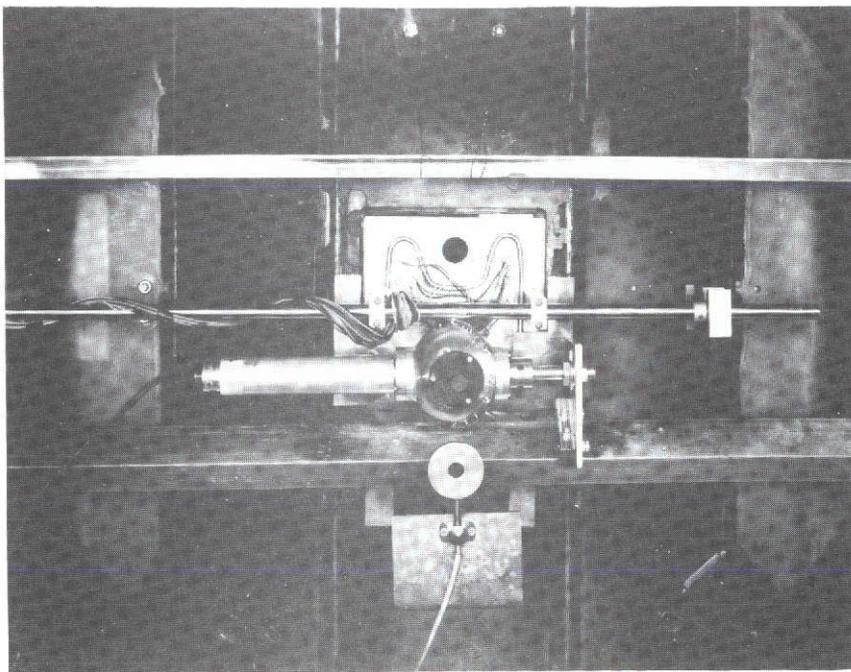
Figure 7-7.   View From Rear of Tank Showing Radio-
meter, Integrating Sphere, and Photo-
multiplier Tube Housing

and the photomultiplier used to measure changes in witness plate trans-
mission can be observed just below the axis of the sample plate suspen-
sion rod. In this position the photomultiplier reads the direct light input
to the integrating sphere. When the sample holder is in the position of
Figure 7-5 the witness plate intercepts the light into the integrating
sphere. Prior to the first ion bombardment this reduced the readout to
the photomultiplier by R_o where

$$R_o = 0.9887 \pm 0.0022$$

Figure 7-8 is a photograph of the sample plate as seen from the ion
source when specimen characteristics are being measured. During
normal testing the J_+ probe shutter was in place to monitor the ion
beam and protect the rear surfaces of the sample plate and wiring from
the beam, as illustrated in Figure 7-9.

The temperature of the sample holder was maintained at $24^{\circ}C \pm 2^{\circ}C$
during ion beam exposures. Following the sequence of exposures, hot
water (45° to $50^{\circ}C$) was passed through the water tubes to aid in evapor-
ation of any cesium which had been deposited on the sample surfaces.
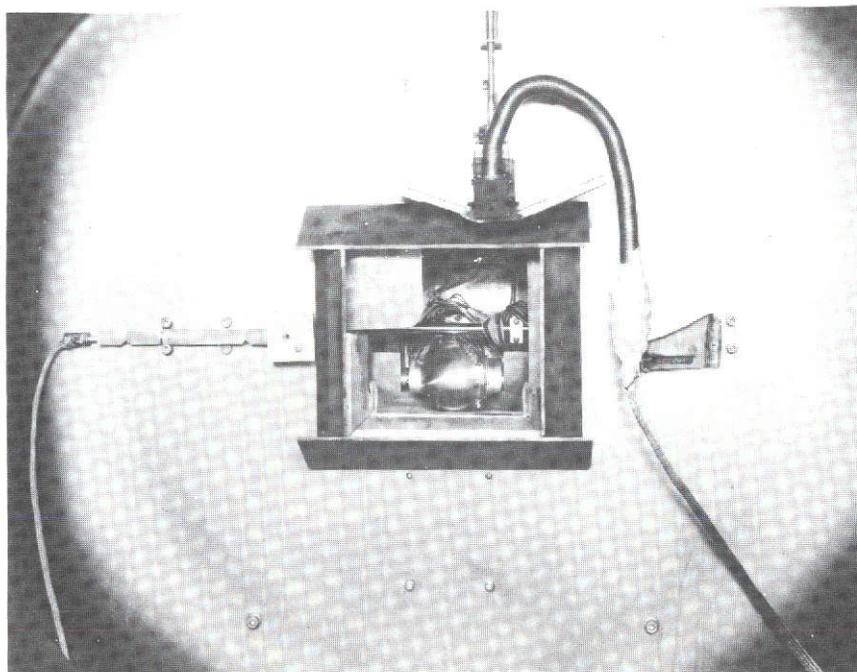
Figure 7-8.   View From Ion Source Showing Samples
Positioned as in Figure 7-5
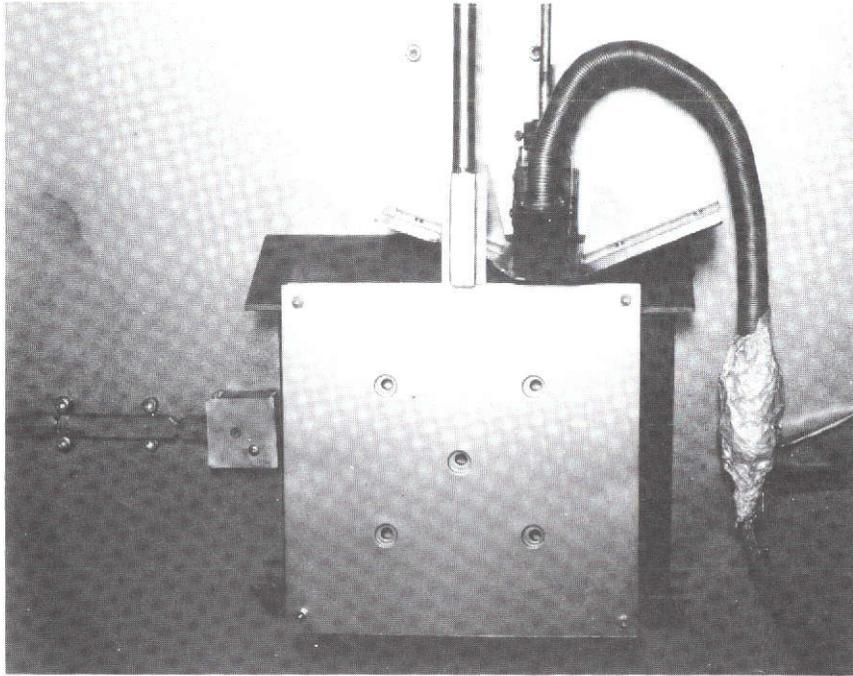
Figure 7-9.   Array of 5 J_+ Probes Used to Determine
Beam Current Density

10-volt Cesium Ion Generation

The original plan for using a reduced exposure of 550-volt ions to simulate the dosage rate of 50-volt ions was discarded at the customer's request.   A decision was made to use 10-volt ions, if possible.

A careful study of the ion source operation and the variables led to an operating mode which assured a reasonably uniform and low density beam of 10-volt cesium ions.   The conditions are:

- Source voltage: +10 volts

- Accel grid voltage: -65 volts

- Accel grid basic pitch: 0.024 inch

- Diode spacing: 0.040 inch

- Neutralizer downstream location: 0.25 inch

- Neutralizer: 0.005-inch diameter x
                                           1.25-inch long

                                           2 amps x 6 volts dc

• Neutralizer dc potential: -1.5 to +4.5 volts with
                                  respect to ground (0 to
                                  +6 along its length)

Neutralizer bias is applied to the positive end of the wire. When the bias voltage is zero, the negative end of the wire is at -6 volts and ion energies are several volts too low. As the bias is raised, ion energy reaches the correct value for a bias voltage of +4.5 volts. With a bias voltage of 6 volts or over, accelerator grid drain current increases to undesirably high levels.

Typical ion current density is 20 microamperes per cm^2 at the source. This leads to an arrival rate at the samples of 2.5×10^{10} ions per cm^2 per second.

When the samples are not being bombarded the moveable probe at 27 inches downstream from the source is moved in to measure beam uniformity and ion energy. This probe has been fitted with a fine mesh screen grid to reduce field penetration. Thus, the current to the collector as measured with an electrometer becomes zero when the collector is biased positively to equal the ion voltage. Typical cut-off characteristics from this probe are plotted in curve (1) of Figure 7-10.

During exposure of the samples to the ion beam a monitor J_+ probe located in the close vicinity of the samples was used to monitor beam density and occasionally check the ion energy. This probe has a 1/8-inch-diameter aperture and has a voltage cut-off characteristic to 10-volt ions as illustrated by curve (2) of Figure 7-10.

7.4 RESULTS

Ion bombardment of samples was terminated after 336 hours of exposure to 10-volt ions. During this time a total dose of 2.75×10^{16} ions/cm^2 had accumulated. Onset of significant changes in sample characteristics occurred for an accumulated dose above 5×10^{15} ions/cm^2. Measurements taken at the end of the run showed the following effects:

• Solar cell short circuit current decreased a maximum
  of 3 percent (for the honeycomb mounting).

• Lens coating sample transmission was reduced slightly
  less than 10 percent to the quartz iodine lamp spectrum.
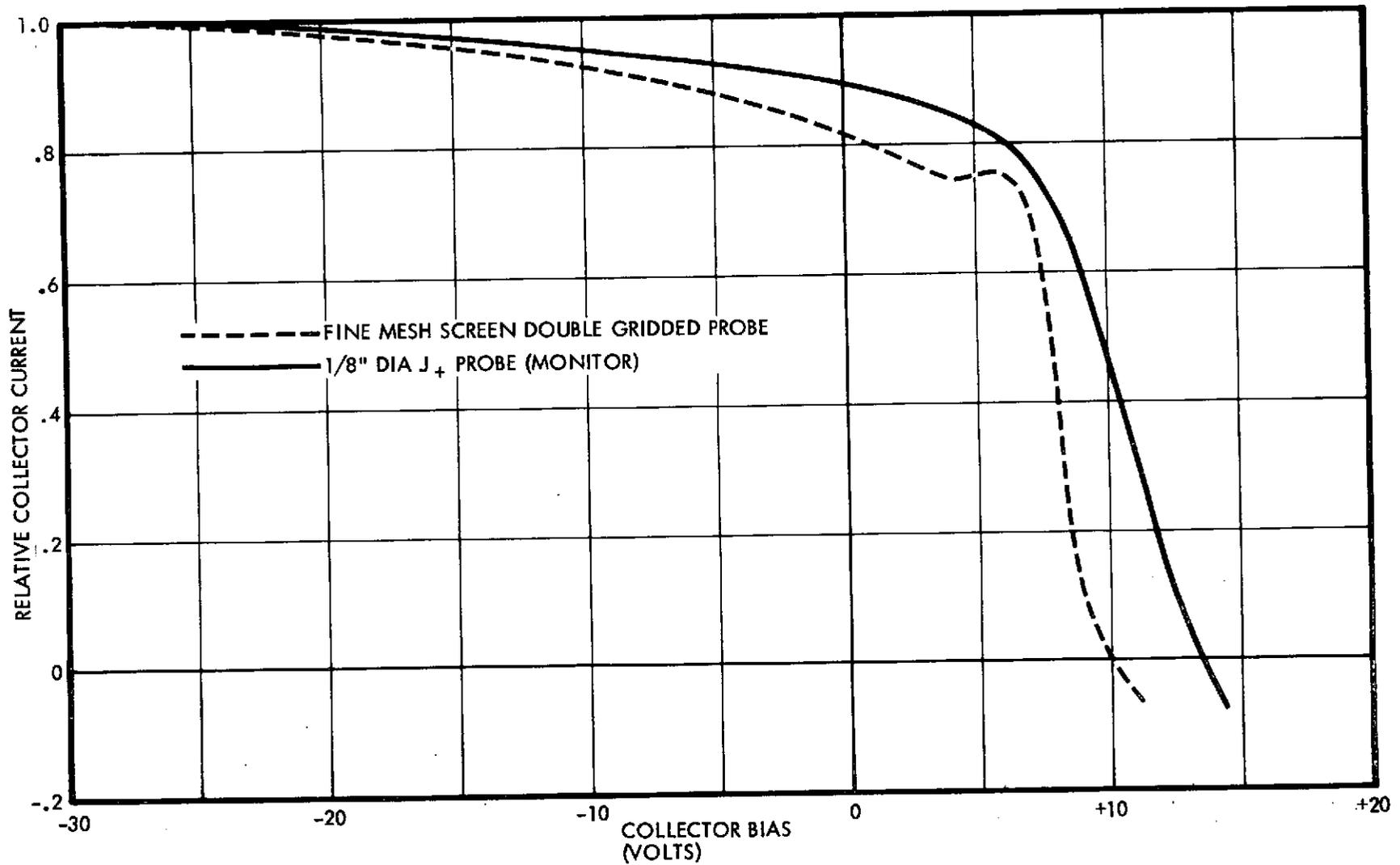
Figure 7-10. Relative Collector Current of Two Probes as a Function of Collector Bias for 10-Volt Ions

- Diffusivity of the specular reflector was barely detectably increased.

- Total reflectance of the specular reflector to helium-neon laser light decreased 10 percent.

Functional monitoring of all samples was performed after each of 10 exposures. These exposures are detailed in Table 7-2 below.

Table 7-2. Summary of 10-Volt Ion Beam Exposures

| Exposure | Date | | Source Current μA | Average J_+ Current Nanoamps | Exposure | | Dose Ions/Cm^2 |
	Start	Finish			Hours	Ions/Cm^2	
1	3/8/73	3/8/73	60	1.57	0.08	0.864×10^{13}	0.864×10^{13}
2	3/30	3/30	44	1.1	0.08	0.633	1.5
3	3/30	3/30	42	1.0	1.0	7.2	8.7
4	4/2	4/4	43	0.83	43.8	262.0	2.7×10^{15}
5	4/9	4/12	28	0.887	60.1	383.8	6.54
6	4/12	4/13	32	0.95	28.2	192.9	8.47
7	4/13	4/16	38	1.13	63.9	519.9	1.367×10^{16}
8	4/16	4/20	35	1.22	71.5	628.2	2.0
9	4/23	4/26	30	1.59	63.0	720.0	2.7
10	5/2	5/2	52	1.2	4.0	34.6	2.7

Solar Cell Results

After each exposure the quartz-iodine lamp was focused on each cell or group of cells and the short-circuit current was measured using a digital voltmeter. These readings were generally repeated three times to assure consistency. For each sample, a ratio was computed of the sample short-circuit current to the sum of short-circuit currents from the two reference cells which were shielded from the ion beam (specimens AAA-3 and AAA-4).

The group showing the largest change was the array of four 2- x 4-cm cells on a honeycomb substrate. No change was noted up to and including exposure No. 7 with an accumulated dose of 1.37×10^{16} ions/cm^2. However, the short-circuit current had decreased by 1.3 percent after 2×10^{16} dosage and by 2.9 percent after 2.75×10^{16}. After the samples had been warmed by flowing hot water through the cooling tubes for a period of 16 hours, this relative drop in short-circuit current recovered to 2 percent.

The FRUSA panel (six 2-x2-cm solar cells on Kapton) showed slight degradation after exposure 7, 1.66 percent after 2×10^{16}, 2.66 percent after 2.75×10^{16} and recovered to 2.26 percent after the 16-hour warmup.

Specimen AAA-2 solar cell showed a 1.39 percent drop after exposure 7 and 2.1 percent after 2.75×10^{16}. Warmup did not improve the results for this sample.

Samples AAA-4 and AAA-3 (exposed) both registered a 1 percent decrease after exposure 7 and 1.5 percent after the final exposure. Warmup improved the results to 1.36 percent.

The measurement error based upon repeatability of the data is about ±0.5 percent.

Lens Coating Sample

Transmission into the photomultiplier tube with and without the WW witness plate was measured after each exposure. The results are plotted in Figure 7-11 which shows that almost all of the 10 percent total decrease in transmission occurred after a total exposure of 10^{16} atoms/cm^2.

Specular Reflector

The power meter readings from the laser light reflected from the specular reflector samples were measured with and without the second spatial filter, and then compared with the power reflected by the first surface mirror alone.

The change in specularity as measured by the ratio of power meter readings with and without the second spatial filter is illustrated in the
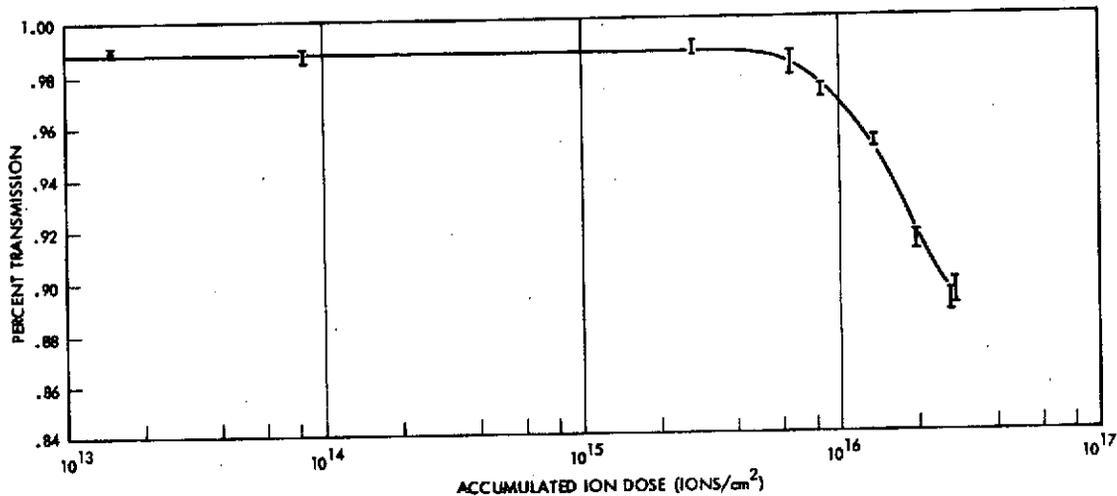
Figure 7-11.   Witness Plate Transmission as a Function of
                Accumulated Ion Dosage.   The method used in
                making this measurement cancels out the
                effect of attenuation by the vacuum window.

plot of Figure 7-12.   Although the scatter in the data is generally poor,
there appears to be a distinct degradation of specularity after an accu-
mulated dose of 10^{16} ions/cm^2.

However, at the termination of the test the quartz window was
removed and the ratio then measured 0.983 compared to 0.99 originally.

Reduction of total reflectance is indicated by the plot of Figure
7-13 indicating a maximum loss of 11 percent at the 0.6328 μm
wavelength.

After the test completion and with the quartz window removed, the
total reflectance was remeasured and found to be 0.815 as compared to
0.90 originally.   From Figure 7-13 it was concluded that the major
portion of the change occurred after an exposure of 1 x 10^{16} ions/cm^2.

7.5 CONCLUSIONS

Solar cell samples, a lens coating sample, and a sample of the
material from the radiometer cooler cone have been exposed to impinge-
ment of 10-ev cesium ions for a total dose of 2.7 x 10^{16}/cm^2 over
a period of 336 exposure hours.   Changes in measured optical properties
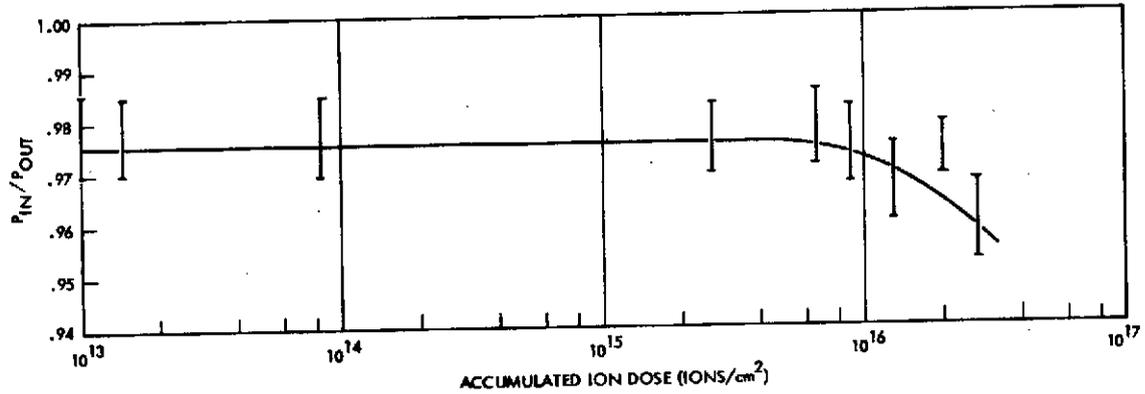
Figure 7-12.   Specularity Ratio for Radiometer Cone Sample
as a Function of Ion Dose.   This is a ratio
of total reflected light to that which passes
through a spatial filter (filter in/out).
Because this measurement is made outside the
vacuum chamber, increased light scattering by
the vacuum window is a significant source of
error in this result.
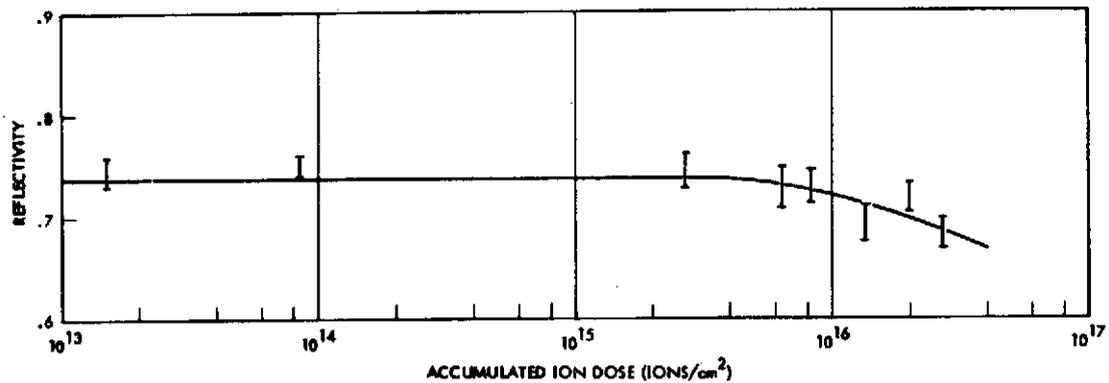
Figure 7-13.   Reflectivity of Radiometer Cone Sample as a
Function of Ion Dose.   This measurement was
made at a wavelength of 0.6328 μm, and
includes losses in the vacuum window as a
source of error.

were observed after a threshold dose of about $4 \times 10^{15}/cm^2$. The total dose for the test was equal to the dose estimated as that which would arrive at the radiometer cooler cone in the absence of any biasing protection. (See Appendix.) Tests at Electro-Optical Systems (Division of Xerox, Inc.) indicate that the scheme in which the cone and housing are biased separately from the spacecraft will effectively prevent charge-exchange ions from impinging on these surfaces. Accordingly, with respect to the radiometer experiment, our results indicate that a problem might have arisen after about 400 to 500 hours of ion engine operation if a means had not been found to protect this surface.

With respect to the solar panels, the test was, in retrospect, of more relevance than anticipated. It was initially thought that only high-energy ions (550-ev) would reach the solar panels. However, in light of the results given in Section 9, it is to be expected that high-energy ion current density to the solar panels will be less than charge-exchange ion current density by one to two orders of magnitude. The peak value of the ion current density curve implies an ion current density maximum at the solar panel of about 1×10^{11} cm^{-2} sec^{-1}, or a total ion dose of about $5 \times 10^{14}/cm^2$. This is almost an order of magnitude below the threshold for any effects on optical properties. This result, taken with those of Sections 4 and 8, in which the OSR samples simulate the solar cell cover glass, tends to confirm the prediction that no degradation of the solar panels will be caused by ion engine operation. There is also no evidence predicting damage to other solar panel materials at the expected ion dosages.

The startracker lens coating will be shielded from direct impingement by charge-exchange ions. However, even under this "worst-case" dosage, the degradation of this material was not sufficient to impair the ability of the detector to identify light from Polaris in the presence of normal background.

Although the results of measurements reported in Section 9 indicate high number densities of charge exchange ions in the space immediately adjacent to the ion engine exhaust plane, arrival rates of low-energy cesium ions at any given spacecraft surface are still difficult to predict with accuracy, especially for surfaces more than 20 to 30 centimeters downstream from the thruster.

8. BACKSPUTTERING EXPOSURES

8.1 POTENTIAL PROBLEMS

The problems under attention here relate to the overcoating of certain spacecraft surfaces by sputtered material. One source of sputtered material is the ion engine itself. A small current (usually less than 1 percent of the beam current) of charge exchange ions bombards the aluminum accelerator grid giving rise to a presumably cosine distribution of aluminum atoms with a source flux density of less than 10^{14} atoms/cm^2-sec. A second class of sputtered material sources consists of all spacecraft surfaces which intercept energetic high divergence angle propellant ions. These ions are customarily designated as Group 2 ions.

The ATS-F spacecraft configuration has been reviewed with these contamination sources in mind in an attempt to determine if serious interaction problems exist.

One ATS-F surface which is sensitive to even very thin films of contaminants is the solar array. The arrival rate of sputtered accelerator grid material will probably be less than 2×10^{10} cm^{-2}sec^{-1}.

The second source of sputtered material mentioned above is EVM surfaces under Group 2 ion bombardment. Reynolds[13] calculates that the arrival rate at the solar array of material from this source is negligible.

The north and south faces of the EVM are largely covered with optical solar reflectors (OSRs). These high emittance surfaces (quartz second surface mirrors) radiate heat from within the EVM under control of automatically positioned louvers in front of the OSRs. The louvers never allow a direct line of sight between the OSRs and the ion engine. However, energetic high divergence angle cesium ions can sputter material from the top surfaces of the VHRR cryogenic radiator housing and Polaris star tracker sun shades through the louvers and onto the OSRs. Through a similar process, louver material can reach the OSRs. In both cases, the pertinent questions are: What is the material deposited on the OSR? What is the rate of deposition? How will OSR properties change with the deposit thickness?

The material sputtered from the louvers will be aluminum, since that is the material of construction. However, small quantities of water vapor will be simultaneously arriving at the OSR surfaces, both by diffusion from within the quartz and from the outgassing of the nearby louvers. One expects, therefore, that some of the arriving aluminum atoms will become oxidized.

The exterior surfaces of both the VHRR and star tracker shades are painted with Dow Corning Thermatrol (DC 92-007) white paint. However, it is possible that after the ion engine is in operation for several hours these surfaces will have acquired an aluminum surface coating from the ion engine accel grid. The estimated aluminum atom arrival rate at the shades is a monolayer in 4 to 24 hours, depending on the grid erosion rate. If this flux exceeds the rate that atoms are sputtered from the surface by Group 2 ions, then the surface will become aluminized. Then aluminum, rather than paint, will be the predominant material sputtered onto the OSRs from these sun shades. At present, insufficient information is available about either the grid erosion rate or the Group 2 ion flux and energy distributions from the engine to predict whether the shades will in fact become aluminized.

8.2   EXPERIMENTAL PROCEDURES

The experimental goals of this series of tests were to measure changes in the transmittance (τ), absorptance (α), and emittance (ϵ) of vulnerable ATS-F surfaces as functions of deposition thickness of sputtered aluminum and DC 92-007.

For the backsputtering experiments a sputter target was installed in the vacuum facility. Ions from the source are partly collected by the ion beam collector. With the shutter open, those ions which are directed toward a square aperture in the collector may proceed to the sputter target. Then material which has been sputtered from the target proceeds directly to the sample position. Accordingly, the sample holder has been modified for these experiments so that it faces the rear of the tank and is parallel to the sputter target as shown in Figure 8-1. The aperture in the collector is 15.6 centimeters (6.125 inches) square. This maps into a 14.2 centimeters (5.6 inches)
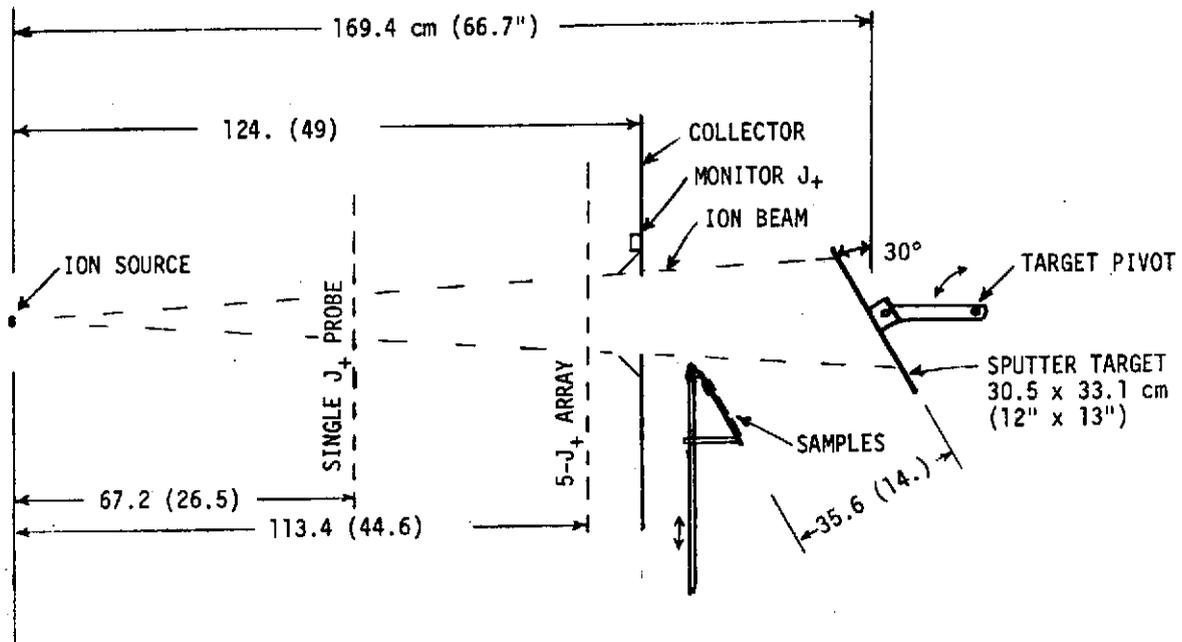
Figure 8-1. Arrangement of Sputter Target and Sample Holder in
Vacuum Tank Relative to Ion Source, Beam Collector
and Ion Density Probes

square at the position of the five J_+ array. Ion current at the sputter
target is determined from the average of the five J_+ measurements over
202.3 cm^2.

Figure 8-2 shows the modified sample holder with samples mounted
for the aluminum backsputtering experiments. An arrangement of pieces
cut from second-surface mirror (OSR) samples is mounted on the central
heat meter. Just to the right of this position a 2- by 2-centimeter solar
cell can be seen. The quartz crystal microbalance is mounted behind
the small hole above the solar cell sample. The two samples at the left
are DC 92-007 white paint and that at lower right is a polished aluminum
disc.

After the sample holder and sputter target had been mounted in the
chamber, the photograph of Figure 8-3 was taken to show the relative
positions of the target, sample holder, collector, and collector aperture.

An important part of the backsputtering experiment series was the
measurements using the quartz crystal microbalance. Accordingly, the
preliminary check-out of instrumentation was primarily concerned with
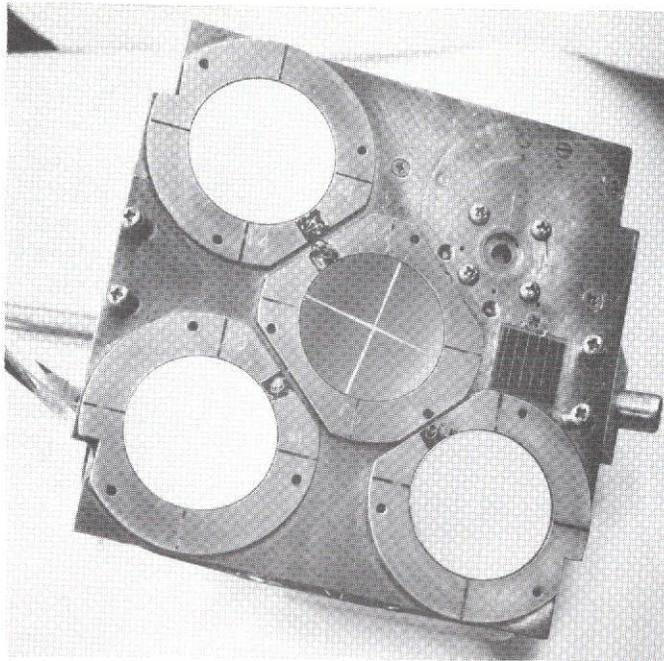
Figure 8-2. Modified Sample Holder with Samples Mounted for
            Aluminum Backsputtering
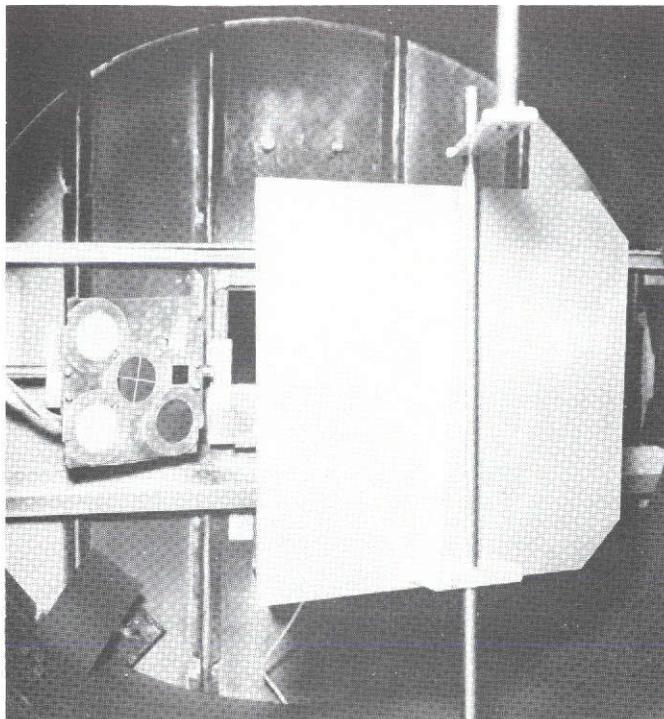
Figure 8-3. View from a Point near Solar Simulator Lamp Showing
            Sputter Target, Sample Holder, Collector, and Beam
            Aperture

this device. It is estimated that the quartz crystal microbalance has a sensitivity of 1.77×10^{-8} gm cm^{-2} Hz^{-1}. At 1.54×10^{15} atoms per monolayer of aluminum, this corresponds to about 3.9 Hz frequency change per monolayer when the crystal is operating at a frequency near 5 MHz. The temperture of the QCM may be monitored by means of a special thermocouple, and thermal test runs of the QCM have been made in vacuum to verify that the base frequency is stable, that the function of frequency versus temperature is repeatable, and that the temperature coefficent of frequency is known. All frequency measurements during sputtering exposures were made at very nearly the same temperature, but these temperature curves were used as required to make small corrections for temperature effects where necessary.

8.3 ALUMINUM BACKSPUTTERING EXPERIMENTS

The first target used was aluminum (alloy No. 1100-0, 99.0% Al). An initial 2-hour exposure (18 May) was invalidated by failure of the liquid nitrogen supply to the diffusion pump cold trap. Following this event, the samples were removed from the chamber and cleaned prior to the start of the "official" runs, although no visible contamination had occurred. After installation of the samples once again, the cryoliners were chilled. They remained cold throughout the entire test series.

Temperature of the sample holder is controlled by a water-cooling system. Either hot (50°C) or cold (18°C) tap water may be passed through water coils attached to the sample holder. Typically, during an exposure run, greater stability of water temperature is achieved by continuously mixing the cooling water in a 4-gallon reservoir from which it flows through the sample holder by gravity. Unless noted otherwise, hot water is passed through the coils when samples are not being exposed in order to minimize adsorption of material.

Test Summary

The experimental sequence (with comments) was as follows:

Between 30 May and 6 June, six exposures were made. Just before the first of these, the sample properties were measured in situ.

Run 1 lasted for 1 hour. Current density was mapped with the 5-J$_+$ array before and after the run, and was monitored during the run,

both at the source and by means of the monitor probe. (This procedure is common to all runs.) During the run, the ion beam was steady.

Between Run 1 and Run 2, the samples were maintained at nearly the same temperature as during the exposure.

Run 2 lasted for 40 minutes. The ion beam was steady.

Following Run 2, the sample properties were measured again.

Between Run 2 and Run 3, hot water was passed through the sample holder overnight.

During Run 3 the ion beam was steady for 20 minutes until a grid wire broke. The run was continued for another 80 minutes at greatly reduced current density.

Sample properties were measured at the end of Run 3. Following this, with the cryoliners still chilled, the tank pressure was increased to atmospheric with dry nitrogen, the ion source was removed, and a new grid was installed. The source was replaced, the tank was pumped down, and the sample holder was maintained at hot-water temperature over the weekend.

Run 4 and Run 5 were both made on the same day. The ion beam continued steady during both runs. Run 4 lasted 70 minutes; Run 5 took 2.2 hours.

Between Runs 4 and 5, cold water flow was maintained in the sample holder for about 4 hours.

Between Run 5 and Run 6, the samples were maintained at hot-water temperature overnight.

Run 6 lasted for 4 hours. The ion beam intensity (as indicated by the 5-J_+ array) was down about 10 percent at the end of the run from its starting value. A wire near the edge of the ion source apparently broke after about 3.5 hours; also, a small increase in ion source current had been noticed at 2.5 hours. Shortly after the termination of the run, the ion source grid failed completely. Sample properties were measured at the conclusion of Runs 4, 5, and 6.

<u>QCM Data</u>

A history of the quartz crystal microbalance frequency of oscillation is shown in Figure 8-4. The vertical scale is frequency shift from the starting value at the beginning of Run 1. The horizontal scale is as shown for the exposure intervals. Time between exposures varied from 4 hours to a few days and is therefore not scaled. Frequency shifts at start and end of each run have been corrected for temperature drift at the rate of 70 Hz per millivolt of thermocouple potential drift (all corrections less than 10 Hz). Between runs, especially when the sample holder was being heated, large frequency excursions occurred. The degree to which the frequency recovered after cooling had been restored is shown in the figure. Detailed structure within an exposure interval has been sketched from the strip-chart records.

The relationships among exposure time, ion dose, and QCM response may be seen in Table 8-1. The columns of the table show run number,
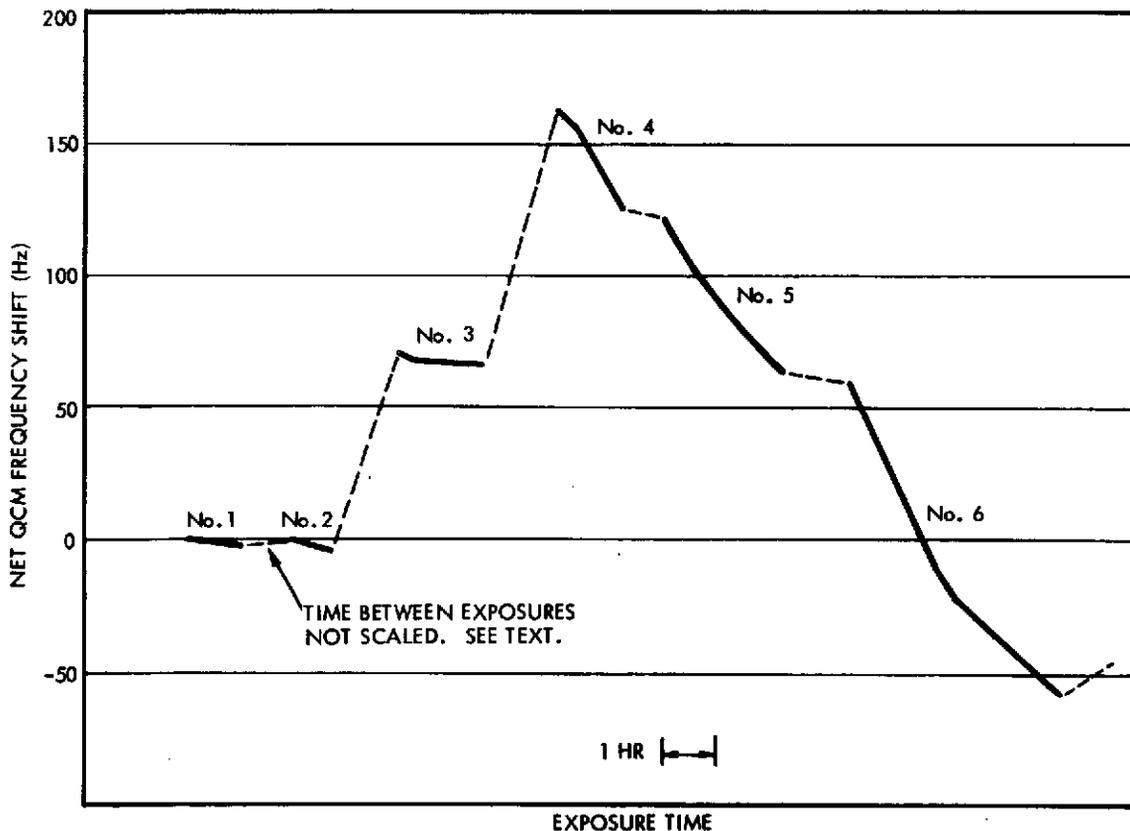
Figure 8-4. Quartz Crystal Microbalance History During Aluminum Target Runs

Table 8-1. Summary of Aluminum Backsputtering Runs

Run	Total Time (hours)	Ion Rate ($cm^{-2}sec^{-1} \times 10^{-13}$)	Ion Dose ($cm^{-2} \times 10^{-16}$)	QCM ΔHz	Total ΔHz (Exposures)	Ratio (c) ($Hz\ cm^2 \times 10^{17}$)	Mass Loading (d) ($gm\ cm^{-2} \times 10^8$)
1 (a)	1.0	1.67	6.03	-1.84	-1.84	3.05	3.3
2	1.7	2.13	11.15	-2.9	-4.74	5.66	8.4
3	3.3	(b)	13.65	-4.38	-9.12	17.52	16.1
4	4.5	2.61	24.62	-36.8	-45.92	33.55	81.3
5	6.7	3.17	49.73	-58.3	-104.22	23.20	184.5
6	10.7	3.37	98.26	-97.2	-201.42	20.03	356.5

Note: (a) No sample property measurements at this time.

(b) Includes 20 minutes at normal rate, 80 minutes at small rate.

(c) Figure of merit proportional to ratio of change of QCM to change in ion dose.

(d) Accumulated mass loading indicated by QCM at 1.77×10^{-8} gm cm^{-2} Hz^{-1} (no evaporation).

total accumulated exposure time, average ion arrival rate during the run, accumulated ion dose, shift in QCM frequency from beginning to end of the run, total accumulated shifts during runs, ratio of QCM changes to ion dose for the run, and indicated accumulation of mass loading. The ion dose rate and ion dose are computed at the plane of the $5-J_+$ array. Corresponding values at a plane normal to the beam axis and passing through the middle of the target would be 0.448 as large, although, of course, the indicated number of ions striking the target is the same using either number.

Thermophysical Properties of Samples

As the exposure series progressed, measurements of solar absorptance (xenon lamp) and infra-red emittance were made at the conclusions of runs. Also measured was the short-circuit current of a solar cell sample. Results of these measurements are shown in Figures 8-5 through 8-9. Here they are plotted against accumulated ion dose (measured at the plane of the $5-J_+$ array) inasmuch as that quantity is most easily related to accumulated ion engine operating time on a spacecraft. Although the QCM was reporting real changes in mass loading during the runs, the optical measurements could not detect any significant effects; there were also no observable changes in physical appearance of the samples. At the end of Run 6, real shifts were observed in absorptance of the quartz and white paint samples, but these effects largely disappeared after several hours at hot-water temperature. Emittances were affected very little. The emittance of the aluminum sample remained constant at 0.10 throughout the test.

At a temperature of 18°C it is quite likely that cesium which had been backsputtered from the target would condense on the samples. It is also likely that this would be re-evaporated at 50°C. The behavior of cesium is an obvious source of uncertainty in these experiments. Another source of complication is oxygen. It is well known that aluminum films acquire oxidized surfaces very quickly in air. It seems also likely that, at the rate at which aluminum could have been deposited on the samples, trace quantities of oxygen from the vacuum system or from the samples themselves could form aluminum oxides at nearly the arrival rate. If all of the material detected by the QCM during runs had been aluminum,
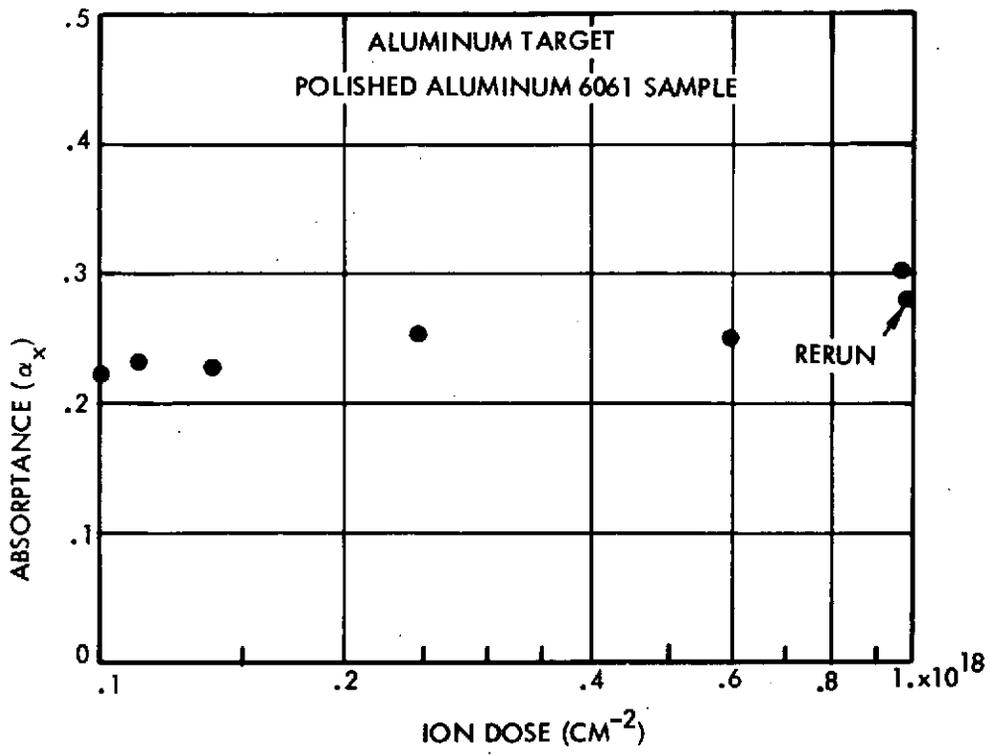
Figure 8-5.   Solar Absorptance of Polished Aluminum Sample, Aluminum Target
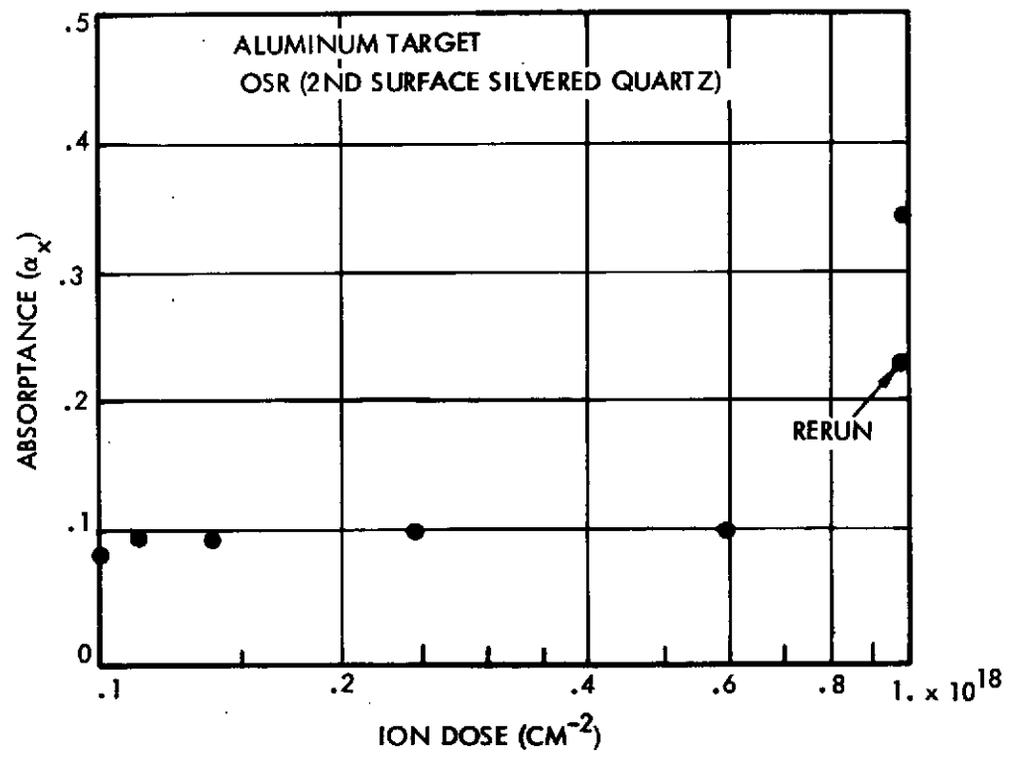
Figure 8-6.   Solar Absorptance of the OSR Sample, Aluminum Target
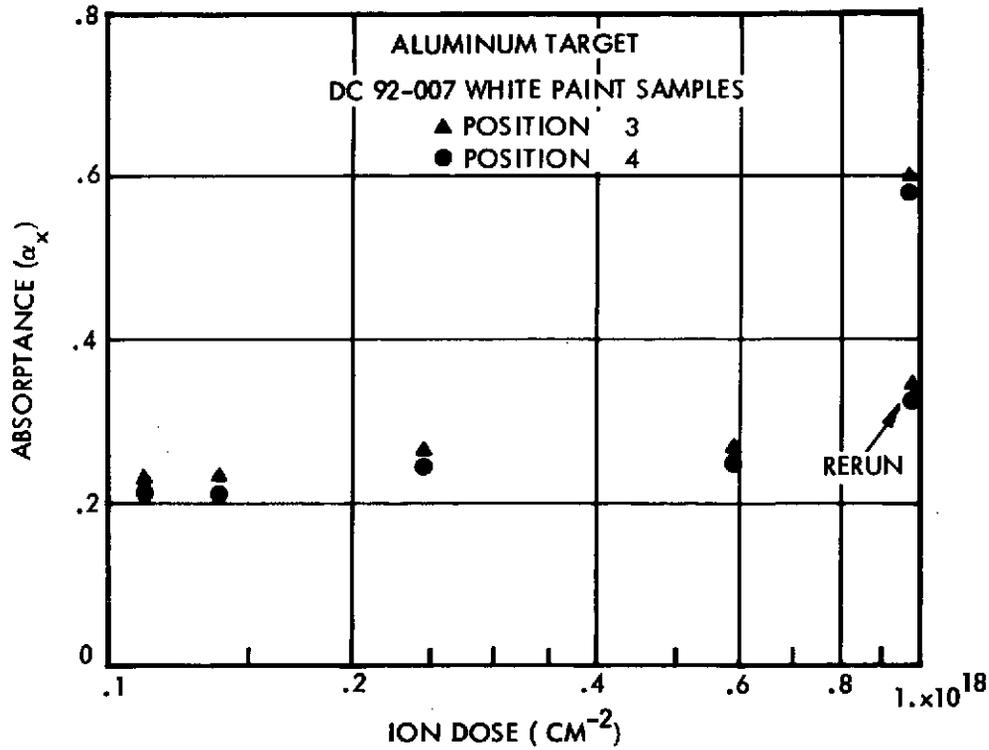
Figure 8-7. Solar Absorptance of White Paint Samples, Aluminum Target
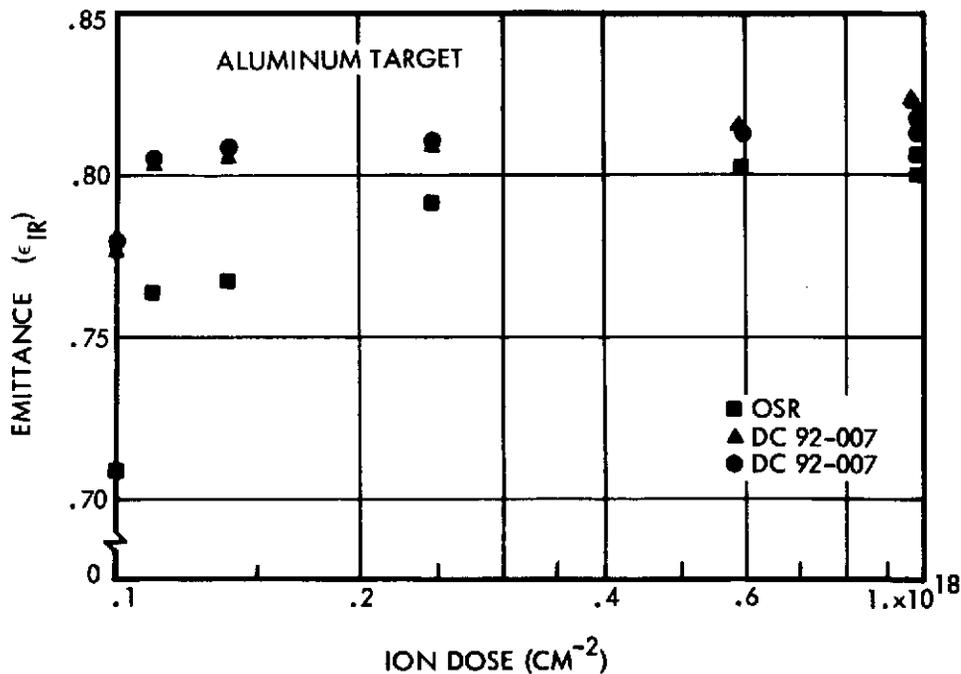
Figure 8-8. Infrared Emittances of OSR and White Paint Samples, Aluminum Target. Emittance of the polished aluminum sample was unchanged at 0.10. Initial values are erroneously low (expected to be 0.82 and 0.78 respectively).
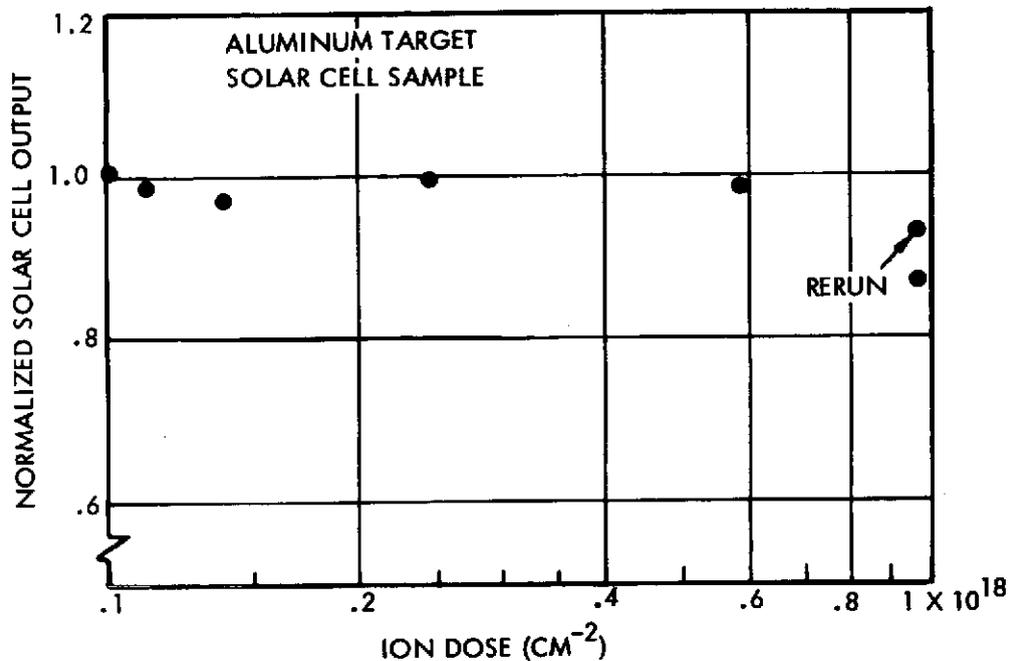
Figure 8-9. Normalized Short Circuit Current from Solar Cell Sample, Aluminum Target

the average thickness of the deposited layer would be at most 130 angstroms. This much aluminum should be detectable by optical means, but 100 angstroms or less of aluminum oxide might not.

If aluminum were present on the samples in sufficient quantity, even in chemically bound form, it would be detectable by the electron microprobe. Two samples of DC 92-007 white paint were examined for aluminum using this instrument. One sample was from the backsputtering series, the other was a new sample for control. The probe does a spectral analysis of X-radiation from atoms in a surface layer of the exposed sample. For this test, a 25-micron-diameter beam of electrons at 5 kev was used to limit the penetration into the sample surface to a minimum (estimated 5 to 6 microns). Results of the test are shown in Figure 8-10. The new sample has a strong silicon peak, probably from the silicone paint binder; the other sample has, in addition, a fairly strong peak from the K-alpha line of aluminum. It should be noted that, by the time this test was made, the exposed sample had been in air for several days, and hence there is no question but that any aluminum present on the surface is in a bound state. In a re-test of this sample, a significant indication from cesium was also observed.
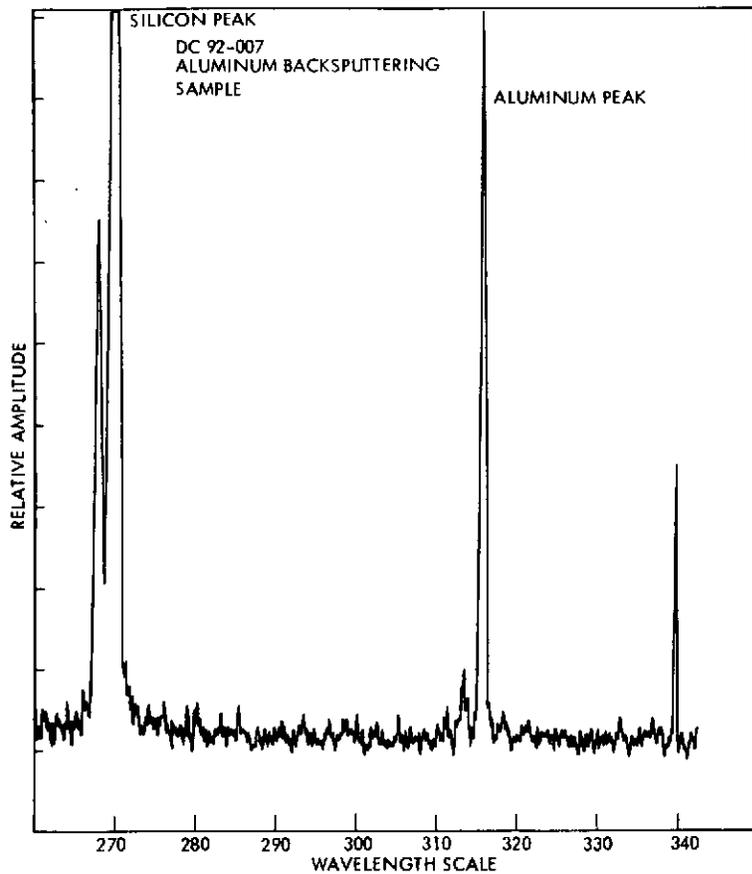
(a)
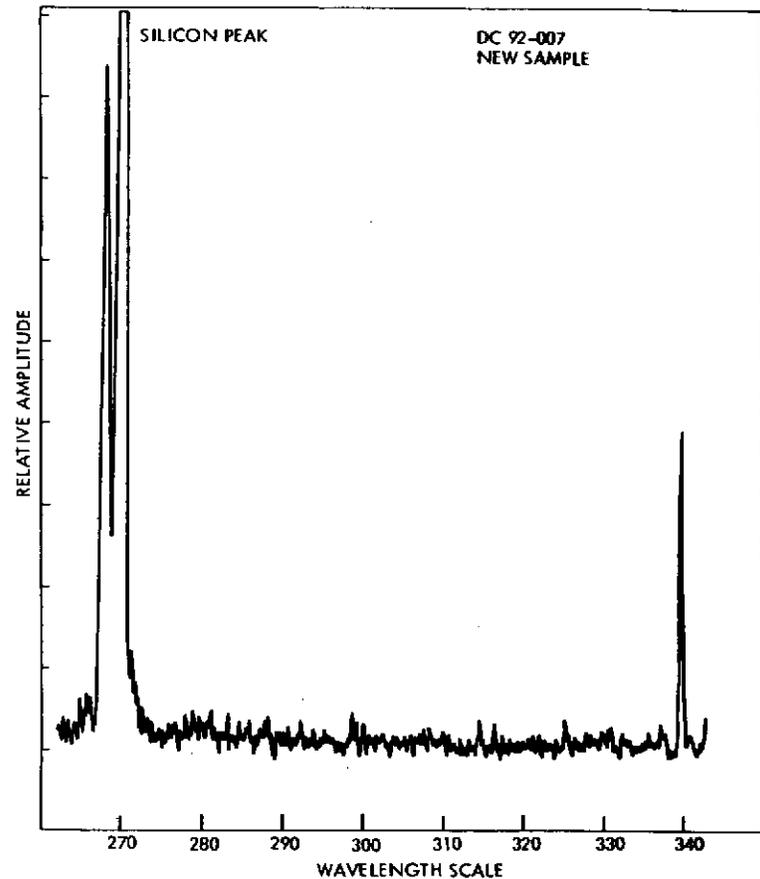
(b)

Figure 8-10.   Electron Microprobe Scan of White Paint Sample.   Response in wavelength region
shown reveals aluminum deposit on backsputtered sample (a), whereas none is
seen on a new sample (b).   The silicon peak is probably from the paint binder.

Conclusions

The effects of material backsputtered from a 1100-0 aluminum target plate did not produce significant permanent changes in test samples after an ion dose of about 2×10^{18} cesium ions/cm^2. Measured parameters were the thermophysical properties (solar absorptance and infrared emittance) of aluminum, quartz (OSR), and DC 92-007 white paint, and the electrical current output of a solar cell. By relating the magnitude of ion bombardment at the target and the geometry of this series to a particular spacecraft situation, one may estimate the margin of safety for this effect. In the case of the ATS-F spacecraft, no hazard is implied from sputtered aluminum films.

Some shift in thermophysical properties and solar cell output was noted after the last long exposure. As pointed out, this effect was largely reversed after a few hours. Whether the recovery was caused by evaporation of a cesium deposit or by oxidation of both cesium and aluminum metallic films cannot be determined. It can be suggested that the amount of aluminum deposited on the samples might represent a significantly dense film if not oxidized, and that the amount of oxygen which could be obtained from the spacecraft surface might be far less than that available from the vacuum chamber. To the extent that this is true, the present results are optimistic.

The results are inconclusive in the sense that the actual mass loading on the samples cannot be determined, nor, in fact, the composition of the deposited material. The most likely candidates are aluminum or aluminum oxide and cesium or cesium oxide (or hydroxide). The x-ray analysis of the surface qualitatively confirms that both cesium and aluminum are present. These are both foreign to the samples on which they were found. In the present experiment there is no way to quantitatively determine the mass loading of these materials or their ratio.

8.4   PAINT BACKSPUTTERING

At the end of the aluminum target backsputtering series, the sample holder was removed from the vacuum tank. The OSR and solar cell samples were cleaned by swabbing with alcohol and left in place.

The paint and polished aluminum samples were replaced with new samples. The aluminum target was replaced with a new target having a thick coat of DC 92-007 white paint.

Test Summary

During the period 12 June to 21 June, eight ion beam sputtering exposures were made. Properties of the samples were measured before Run 1 and at the conclusion of each run. Following are brief comments on conditions and problems during runs and on the status or sequence of operations between runs: .

Run	Comment
1	Beam steady.
**	Four hours cold water to sample holder.
2	Beam steady.
**	17 hours cold water.
3	Beam steady.
**	Overnight hot water.
4	. Grid short about 15 minutes into the run, corrected; beam steady after that.
**	Overnight hot water. Tank opened to replace grid, then pumped down 4 hours before start of next run.
5	Beam steady.
**	Cold water over weekend; then brief hot water before start of run.
6	Beam interrupted twice by grid shorts; problem corrected until end of run, then grid failed.
**	Hot water overnight; tank opened, pumped down, cold water to start of run.
7	Beam steady.
**	Overnight hot water.
8	Grid shorted once near end of run.

These details are included here so that they may be correlated with the history (temperature-corrected start-stop values) of the QCM shown in Figure 8-11 and with the summary of the series in Table 8-2.

At the conclusion of Run 8, it was intended that even more exposure be given to the samples. Accordingly, inasmuch as the ion source grid was giving so much trouble, a new ion source was installed in the facility. This task was finished just before the close of the work day on Friday, and the facility was left on the roughing pump to be checked later in the evening. This check revealed that a vacuum leak existed in the setup which was large enought to prevent switching to the high vacuum pump. As a result, the samples were left at about 1 torr pressure (air) over the weekend. Properties of the samples were measured in situ and some changes had occurred since the measurements at the end of Run 8.
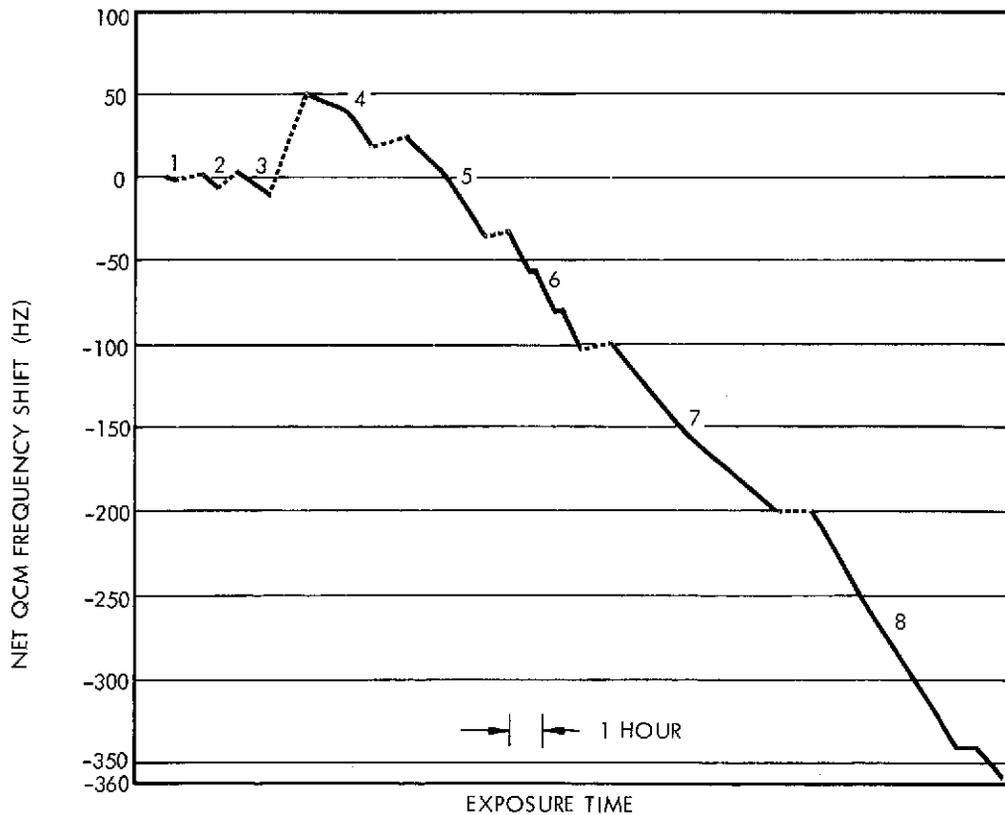
Figure 8-11. Quartz Crystal Microbalance History During Paint Target Runs

Table 8-2.   Summary of Backsputtering Runs Using Paint Target

Run	Total Time (hours)	Ion Rate ($cm^{-2}sec^{-1} \times 10^{-13}$)	Ion Dose ($cm^{-2} \times 10^{-16}$)	QCM ΔHz	TOTAL ΔHz (Exposures)	Ratio (Hz $cm^2 \times 10^{17}$)	Mass Loading (gm $cm^{-2} \times 10^{8}$)
1	0.25	1.6	1.44	- 1.1	- 1.1	7.64	1.9
2	0.75	1.82	4.72	- 5.7	- 6.8	17.38	12.01
3	1.75	1.29	9.37	- 12.0	- 18.8	25.80	33.3
4	3.75	1.47	19.93	- 33.3	- 52.1	31.53	92.2
5	6.17	1.85	36.05	- 58.6	-110.7	36.35	196.0
6	8.25	2.36	53.72	- 70.6	-181.3	39.95	320.9
7	13.25	1.61	82.62	-120.6	-301.9	41.61	534.4
8	18.75	1.81	118.46	-137.0	-438.9	38.22	776.8

Although these changes had been small, they were a large portion of the changes that had occurred during the preceding run. Furthermore, a visible pattern had appeared on the surface of the aluminum sample that had not been seen before the weekend. Since the ion dose for this series had already exceeded that of the aluminum series, it was decided to terminate the series and remove the samples for detailed examination.

Visual Examination

The photograph of Figure 8-12 was taken of the samples immediately after removal from the facility. It attempts to depict the surface films which were then visible on the aluminum (lower left) and OSR (center) samples, in particular. A thin, light-colored haze may be seen on the OSR sample, with lesser concentrations near the junctions of the four pieces, and greater concentration near the edges. Some splotchy patches are visible on the aluminum sample, with additional well-defined areas of fogging near the edges of the disk. The photo was taken with special lighting to make these features visible in the figure. In fact,
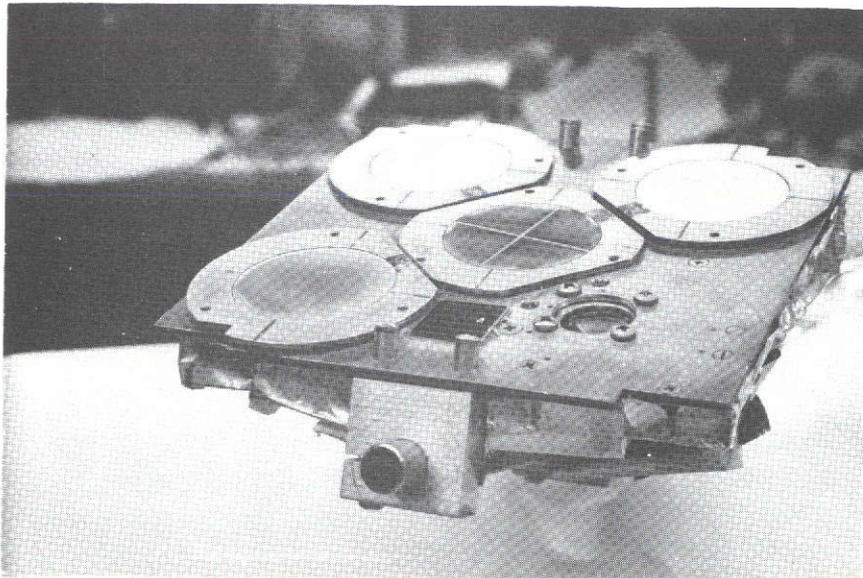
Figure 8-12.   Photo of Sample Holder and Samples after
                Removal from Vacuum Tank. Some alter-
                ations of surface appearance, especially
                near the edge of the aluminum sample (left),
                had occurred over a weekend in the pre-
                sence of an air leak.

8-18

except for the patches at the edge of the aluminum sample, special
lighting was needed to view these effects. Otherwise, the sample
holder and the other samples appeared to be in new condition.

Electron Microprobe Data

As in the aluminum backsputtering case, attempts were made to
confirm the presence of backsputtered material on exposed samples
using the electron microprobe. Full scans were made for the aluminum
and quartz samples with the following results:

		Element Found
Aluminum Sample:	copper	trace
	iron	low
	manganese	trace
	chromium	trace
	cesium	medium
	silicon	trace
	aluminum	high
	magnesium	low
Quartz (OSR):	silicon	high
	oxygen	high

The elements found in the surface of the aluminum sample may all be
accounted for as being constituents of the 6061 alloy, except for cesium.
If titanium had been found, it would almost surely have come from the
paint target, but none was found either on the aluminum or quartz
samples. It was later learned that the quartz samples had been pre-
pared by cutting with a water-cooled abrasive wheel; hence, any de-
posited film that was not resistant to rinsing with water would have been
washed away. This probably accounts for the failure to find any cesium
on the quartz sample. The obvious conclusion from these results is
that the hazy film which appeared on the samples was cesium hydroxide
which formed during the weekend-long exposure to air at 1 torr.

Thermophysical Properties

The effects of backsputtered products from a DC 92-007 target
plane on the thermophysical properties are shown in Figures 8-13
through 8-15. Points marked with arrows were taken after the exposure
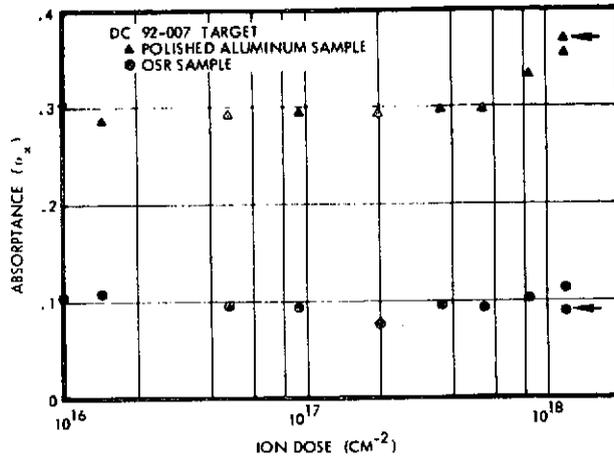
Figure 8-13.   Solar Absorptance of Quartz (OSR)
and Polished Aluminum Samples,
White Paint Target
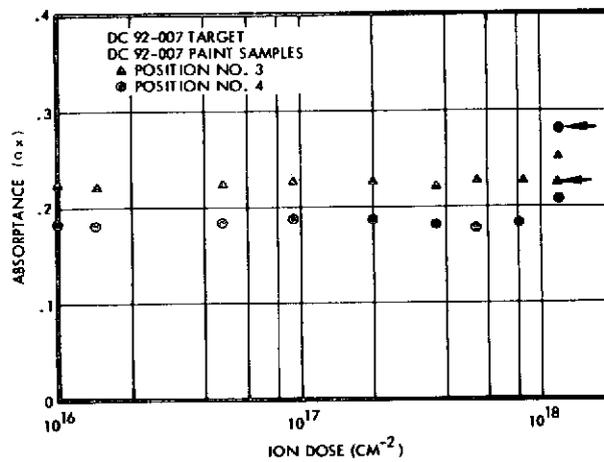
Figure 8-14.   Solar Absorptance of White Paint
Samples, White Paint Target
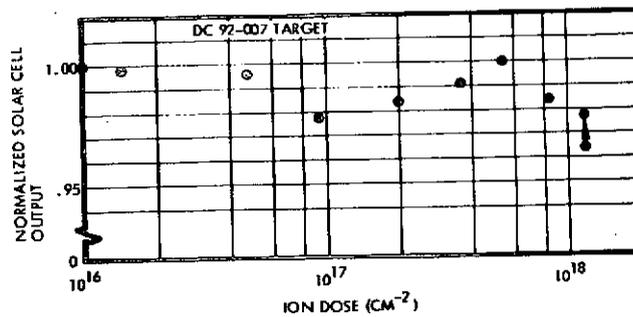
Figure 8-15.   Normalized Short Circuit Current
Output of Solar Cell Sample, White
Paint Target

8-20

to low-pressure air. Only one sample (polished aluminum) exhibited any significant change in properties until the last sputtering exposure exceeded 10^{18} Cs ions/cm^2. The data on Figure 8-13 indicate that a change in absorptance of the aluminum occurred at 8×10^{17} ions/cm^2, while no other samples changed at that point. The evidence seems to point to a chemical attack by cesium.

Conclusions

The absence of any titanium deposit from the white paint target on any of the exposed samples indicates either that the sputtering yield for cesium ion bombardment of this material is very low, or that the sputtered material may not adhere to the samples on encountering them. There is no evidence from these experiments that backsputtering of white paint will be a problem for the ATS-F spacecraft.

9. WIDE ANGLE MEASUREMENTS OF THE ATS-F ION
THRUSTER BEAM

Measurements described in this section were undertaken with a two-fold purpose. There was interest in exploring the unexpected result that biasing the neutralizer of the ATS-F ion thruster negatively relative to a simulated spacecraft surface had not succeeded in lowering the plasma potential relative to that surface. It had been hoped that this means would be available for repelling charge exchange ions from the radiometer cooler cone surfaces and from the surfaces of the radiometer cone shield and startracker shields. In addition, these measurements were desired for use in estimating the ion dosage for both high-energy ions and for charge-exchange ions which will be experienced on spacecraft surfaces during the lifetime of the ion engine experiment.

The program accomplished diagnoses of the thrust beam with the spacecraft surface unbiased, and biased positively relative to the neutralizer potential.

Measured parameters of the thrust beam include electron temperature, plasma potential, average thrust and charge-exchange cesium ion energies, ion current density profiles with spacecraft biased and unbiased, including and excluding charge-exchange ions, and dynamic resistance measurements between the thrust beam and tabs on the spacecraft surface. In the data reduction, special attention was given to the production mechanism and transport of the charge-exchange cesium ions to the spacecraft surface.

An alternative biasing scheme had been proposed, in which only the radiometer cooler cone is biased relative to the neutralizer. Tests performed under another program have confirmed that this method will protect the cooler cone without impairing the neutralization of the ion beam.

9.1 EXPERIMENTAL FACILITIES

The experiments were performed in the Electro-Optical Systems large vacuum system which is 22 feet in diameter with liquid nitrogen cooled shrouds. A portion of the facility and the diagnostic probes is shown in Figure 9-1. The floor and shrouds are at ground potential while the 14-foot by 14-foot square collector can be isolated from ground. The

6 FT R.

PROBE PACKAGE

COLLECTOR

ION ENGINE

RETARDING
POTENTIAL
ANALYZER

θ

37°

SPACECRAFT
SURFACE

CRYOWALL

FLOOR

22 FT. DIA.
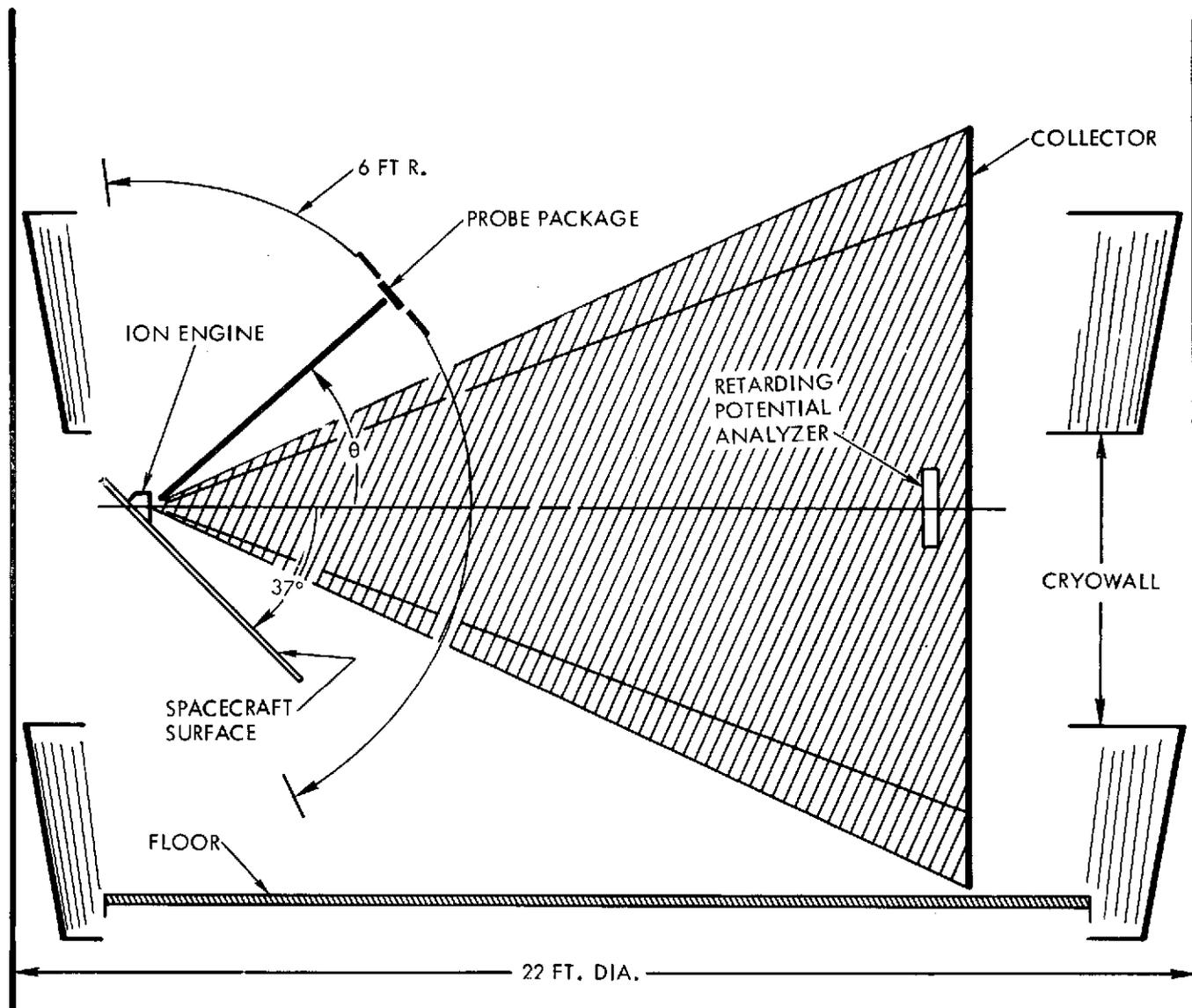
Figure 9-1. Experimental Facility

collector is located ~15 feet from the thruster face. The 54-inch by
64-inch spacecraft surface is a conductor, which simulates the ATS-F
spacecraft surface, with overlying conducting tabs to monitor current to
various portions of the spacecraft surface. There is an additional struc-
ture located on the spacecraft surface which specifically represents the
radiometer cooler cone on the ATS-F craft. This tab is located, when
viewing the spacecraft surface head-on, near the lower left corner of the
surface. The orientation of the surface is 37 degrees to the horizontal
and the thrust beam axis, whereas the exact specification of the thrust
beam axis to the craft surface, between 35 to 40 degrees, will not be made
until the ATS-F craft has been fully integrated.

The 8-centimeter (beam) diameter cesium ion engine was built by
Electro-Optical Systems and employs a cesium vapor discharge neutralizer.
For the experiments performed in the program the thrust ion energy
ranged from 500 to 550 ev with a total ion beam current of ~0.11 ampere.
The cesium vapor discharge neutralizer normally operated with a 5-volt
potential difference between the neutralizer and the keeper, and a total
electron injection potential of 10 volts. Therefore, with the collector
operated near chamber ground, the neutralizer and the spacecraft surface
at -6 volts, the plasma potential at the injection region was a few volts
above chamber ground.

The thrust beam diagnostic probes included a retarding potential
analyzer and a probe package consisting of emissive probes, a Langmuir
probe, and a Faraday cup. The large, 6-inch by 12-inch aperture, retard-
ing potential analyzer was fixed on the axis of the beam ~13 feet from the
thruster. The probe package, illustrated in Figure 9-2, was mounted on
a boom and moved on an arc of 6-foot radius centered at the thruster face.
The arc was located in a vertical plane such that the probe package could
scan through the thrust beam axis. A unique feature of the probe package
was its ability to scan the thrust beam to very large angles, $-60 < \theta < 110$,
(θ in degrees), with respect to the thrust beam axis. The emissive
probes were mounted on ~10-inch stalks tangent to the arc described by
the probe package. The emissive portion of each probe was a little
"hairpin" of 0.002-inch diameter tungsten wire ~0.50-inch long. The
Langmuir probe, located 10 inches in front of the Faraday cup, consisted

EMISSIVE PROBE

FARADAY-CUP PROBE

LANGMUIR PROBE

EMISSIVE PROBE
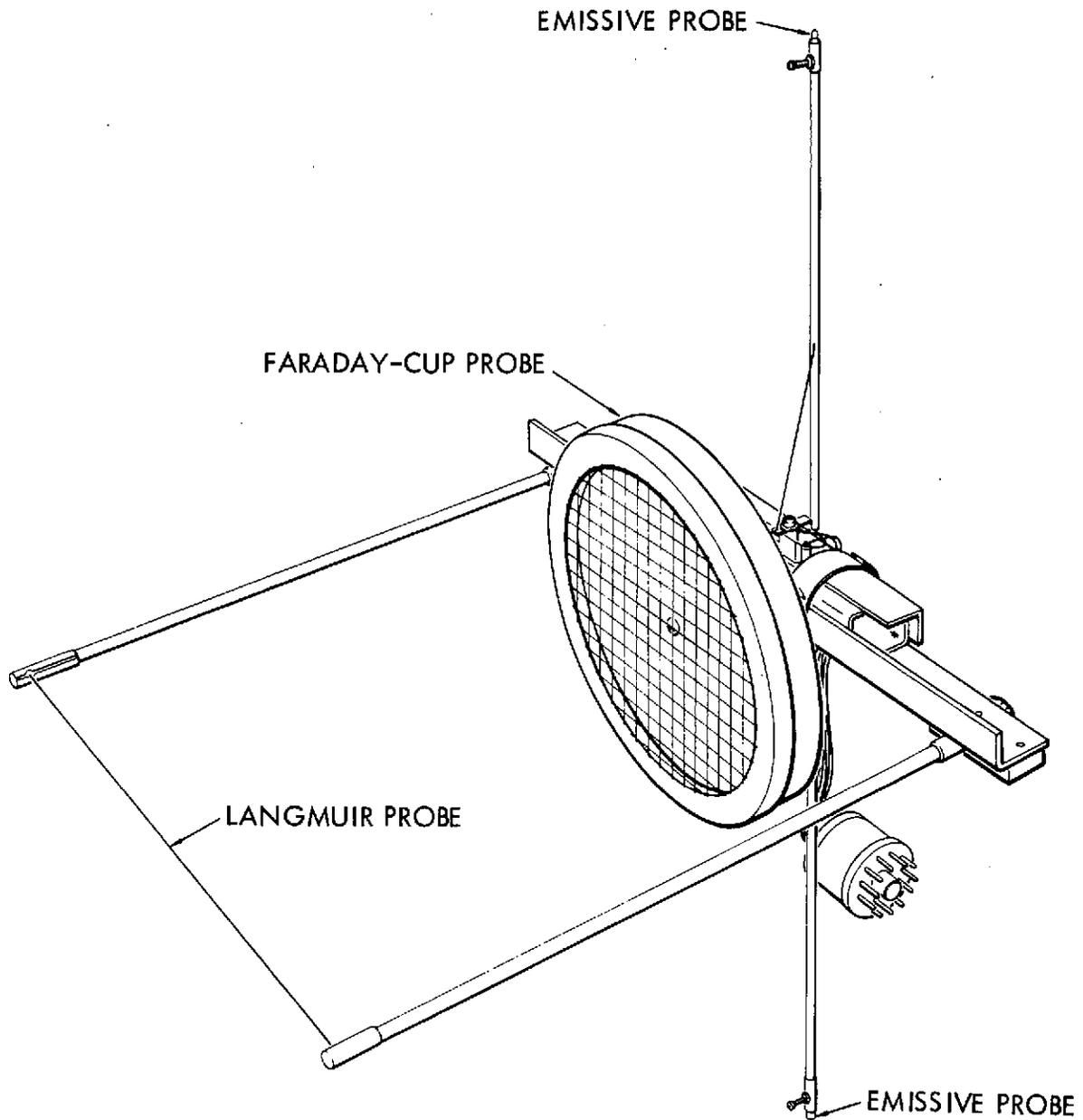
Figure 9-2. Probe Package

of an 8-inch-long 0.005-inch-diameter tungsten wire which was operated
at ~1000°C. The Faraday cup has an aperture of 3-1/2-inch diameter and
a double grid structure with an optical transmission of 45 percent.
Because the grids could be separately biased, the Faraday cup also served
as a retarding potential analyzer.

9.2 EXPERIMENTAL RESULTS

While operating the cesium ion engine in its normal mode (that is with an injection potential of approximately 10 volts and the spacecraft surface at the neutralizer potential), a retarding potential analysis and a Langmuir probe measurement were performed. The average cesium ion energy determined from the data of the retarding potential analyzer located ~1-1/2 feet upstream from the collector was ~550 ev. This result was anticipated, since the ion energy was set at 550 ev at the thruster. A Langmuir probe measurement was performed on the axis of the thrust beam approximately 5 feet downstream from the thruster. The data are shown in Figure 9-3 and give a value for the electron temperature of 0.4 ev. Recall that the injection potential was 10 volts so that is not inconsistent with the measured electron temperatures in the thrust beam of Hg ion engines with comparable injection potentials. Also, in laboratory experiments with cesium ion beams where the initial electron temperatures are known, the electron temperature in downstream regions has always been less than those in the injection region (Reference 4).

Next, Faraday cup scans through the thrust beam were performed for several neutralization conditions. Figure 9-4 shows a typical current density profile for the cesium ion engine functioning in its normal mode. Initially, about $\theta = 0$ (axis of the thrust beam) the thrust beam displays a parabolic core and an exponential wing. This same behavior is observed for laboratory plasma beams. However, moving to larger θ in Figure 9-4, one finds rather interesting structure in the current density. At $\theta \sim \pm 20$ degrees there is a little shoulder which falls off to an exponential wing. When $\theta \sim 53$ degrees there is a secondary peak with a slow fall-off at larger values of θ. The sharp decrease in current density at $\theta \sim -48$ degrees occurs because the Faraday cup is now in the shadow of the edge of the spacecraft surface (see Figure 9-1) and is no longer in the line of sight of the thruster. Such structure has not been observed for laboratory cesium plasma beams. But of greater concern is the fact that for this "pencil" beam a sizable current density is present at high angles (large θ).

The neutralization condition was effectively changed by biasing the spacecraft surface relative to the neutralizer. Figure 9-5 displays the current density profile for the thrust beam along the same physical path
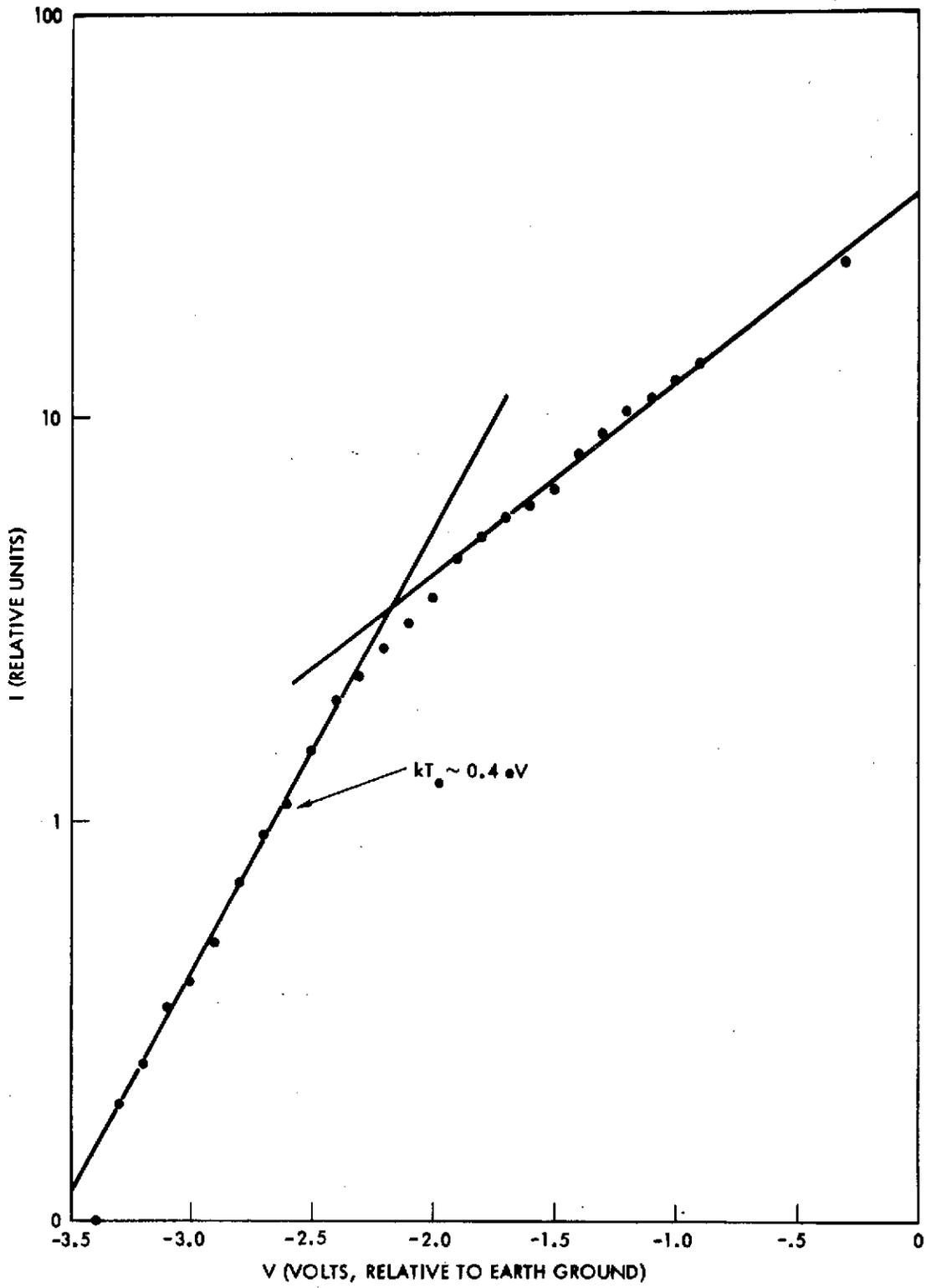
Figure 9-3. Langmuir Probe Measurement on the
Axis of the Thrust Beam
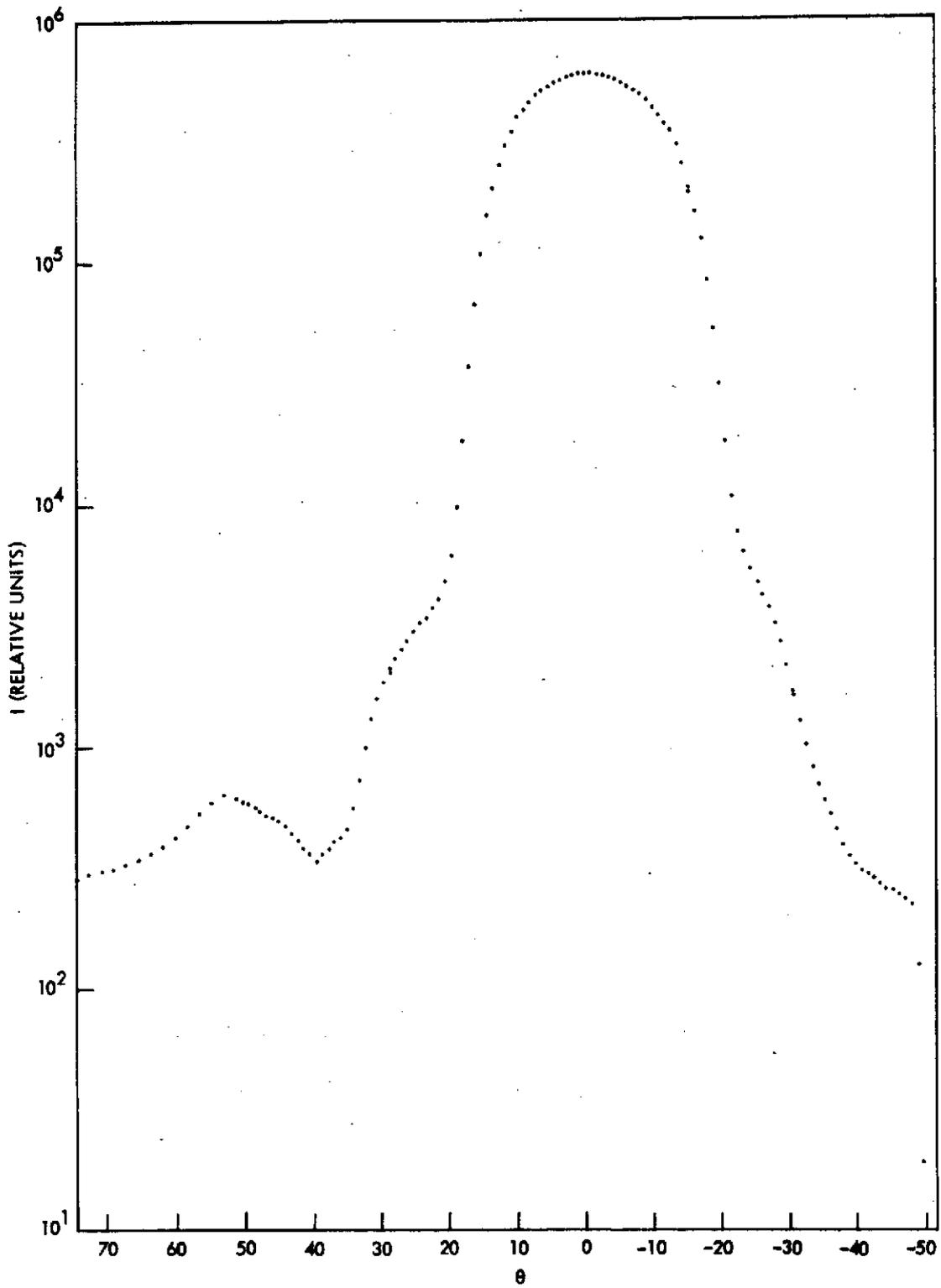
Figure 9-4. Ion Current Density Profile for the Case Where the
Spacecraft and Neutralizer are at the Same
Potential

9-7
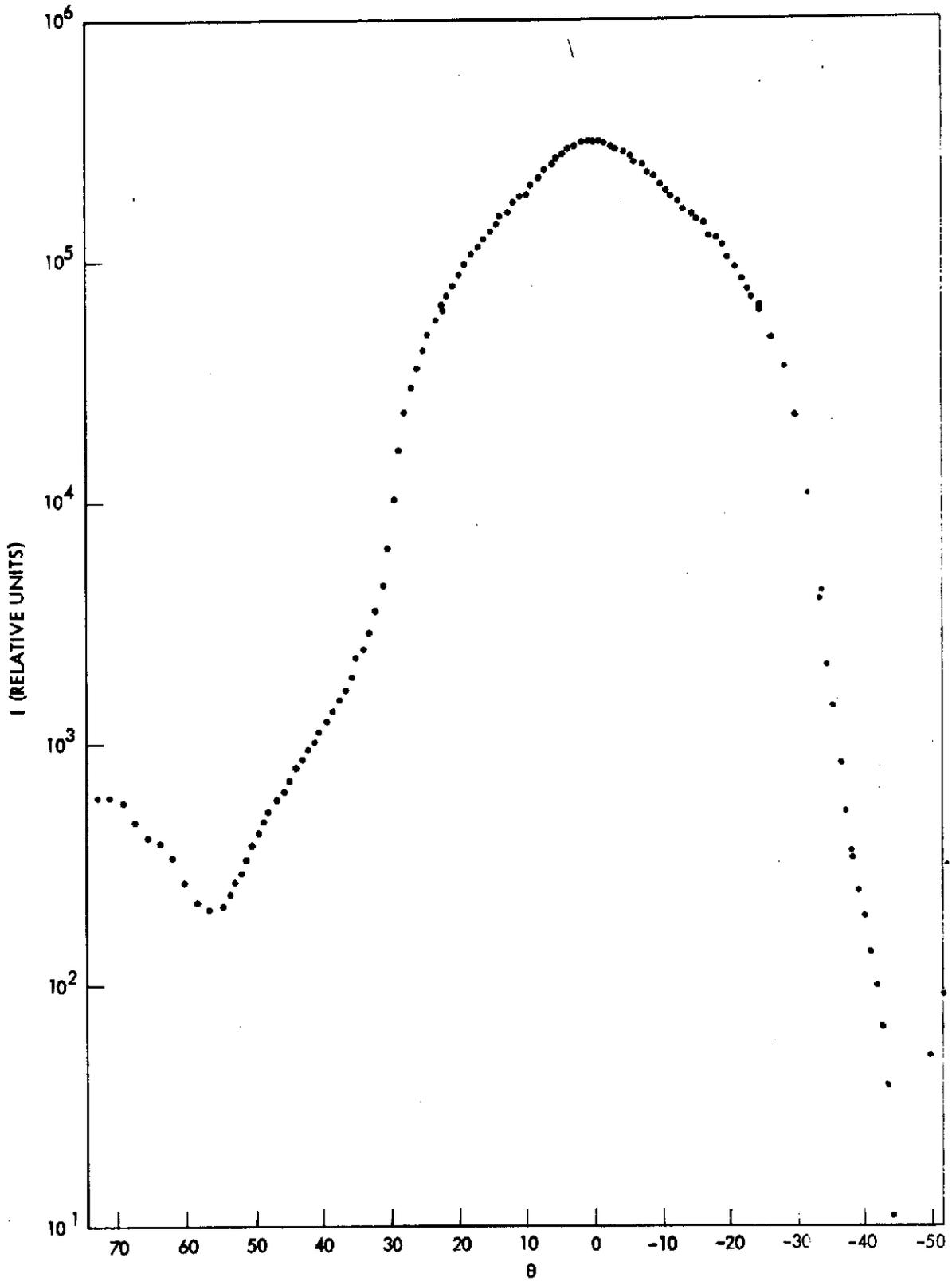
Figure 9-5. Ion Current Density Profile for the Case Where the Spacecraft is Biased 30 volts More Positive Than the Neutralizer

as the previous figure. Notice that basically the same structure is present, but the thrust beam has a lower central amplitude and appears to be spread out. This leads one to believe that somehow the electron temperature has increased and the resulting increase in electron pressure has caused the thrust beam to broaden.

However, of primary concern is the large current of ions present at high angles, at the left side of the figure. If the thrust beam has azimuthal symmetry about its axis, and there is no reason to doubt this; and if the current density profile that is observed 6 feet from the thruster is indicative of the current density profile much closer to the source, then it is highly probable that the operation of the thruster can interact with spacecraft systems located on the side nearest the thruster. Specifically the side in question could become coated with the propellant, changing the surface's electrical state, emissivity, and absorptivity. Consequently, tabs on the spacecraft surface were biased and the current collected as a function of this bias was measured. The derivative of the collected current with respect to the bias voltage which is now a differential resistance for one tab is shown in Figure 9-6. Minimum values for the differential resistance of any particular tab biased a few volts more positive than the spacecraft range from 300Ω to 1000Ω, which indicates there is good coupling between the spacecraft surface and the thrust beam and that with an angular separation of 37 degrees between the beam axis and the surface, the spacecraft surface is being washed by the thrust beam plasma.

A retarding potential analysis was performed in the region of the secondary peak in the current density shown in Figure 9-4, since, under the assumptions made earlier, this secondary peak should occur in the region of space occupied by the spacecraft surface. The analysis revealed that the current density peak resulted from lower energy (~2 ev) ions. The result was also verified when a Faraday cup scan was performed with and without a positive 10-volt bias (with respect to ground) on the Faraday cup collector. Addition of the bias excluded the low energy (<10 ev) ions from being collected, and altered the high-angle beam profile as shown in Figure 9-7. Here, a significant departure from the current density plot of Figure 9-4 is seen to occur at an angle of about 30 degrees. Thus, the high level of ion current observed at high angles ($\theta > 40$ degrees for normal operating conditions) is mainly due to low energy ions.
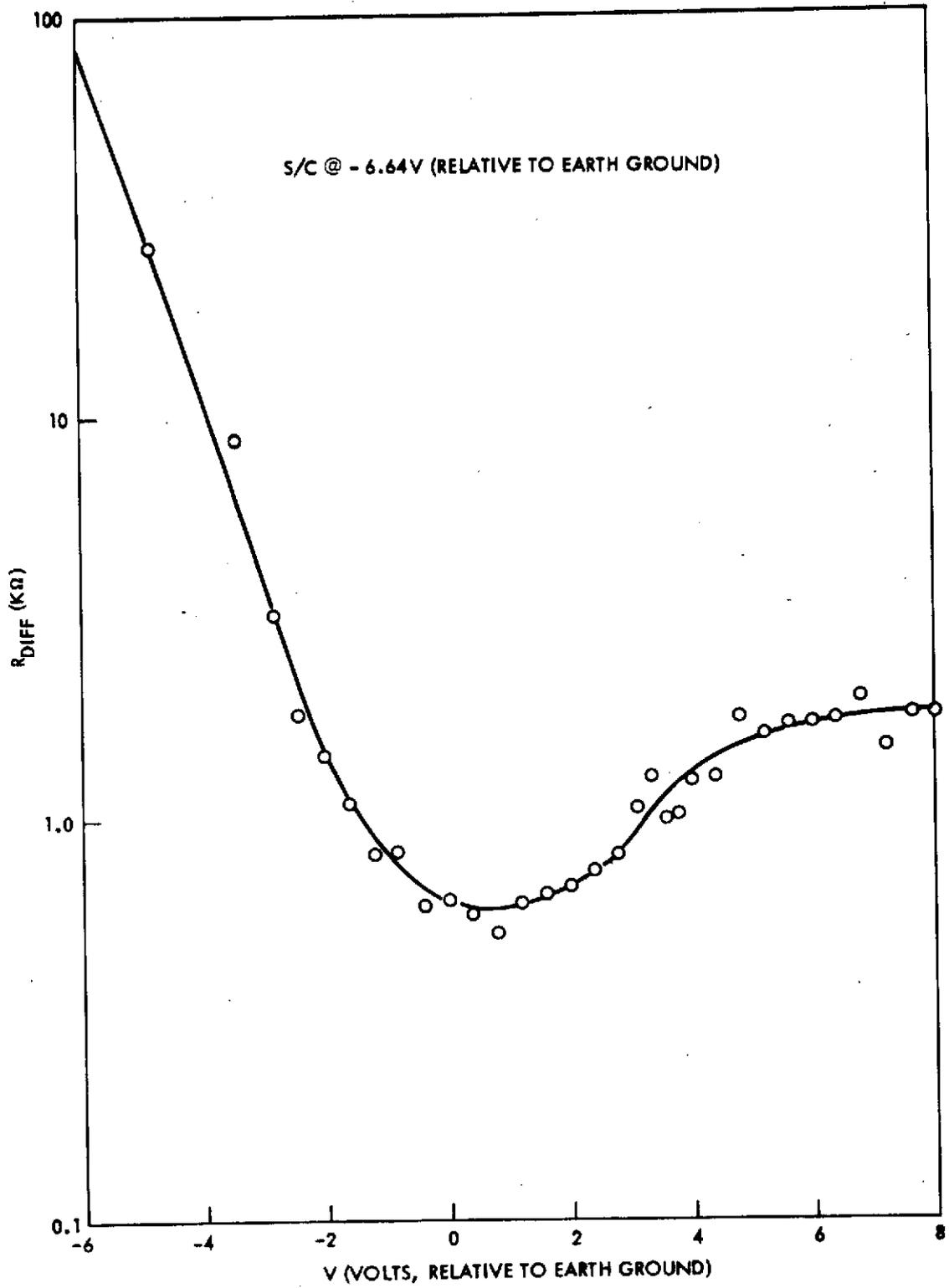
Figure 9-6.   Typical Differential Resistance of a
Tab to the Thrust Beam
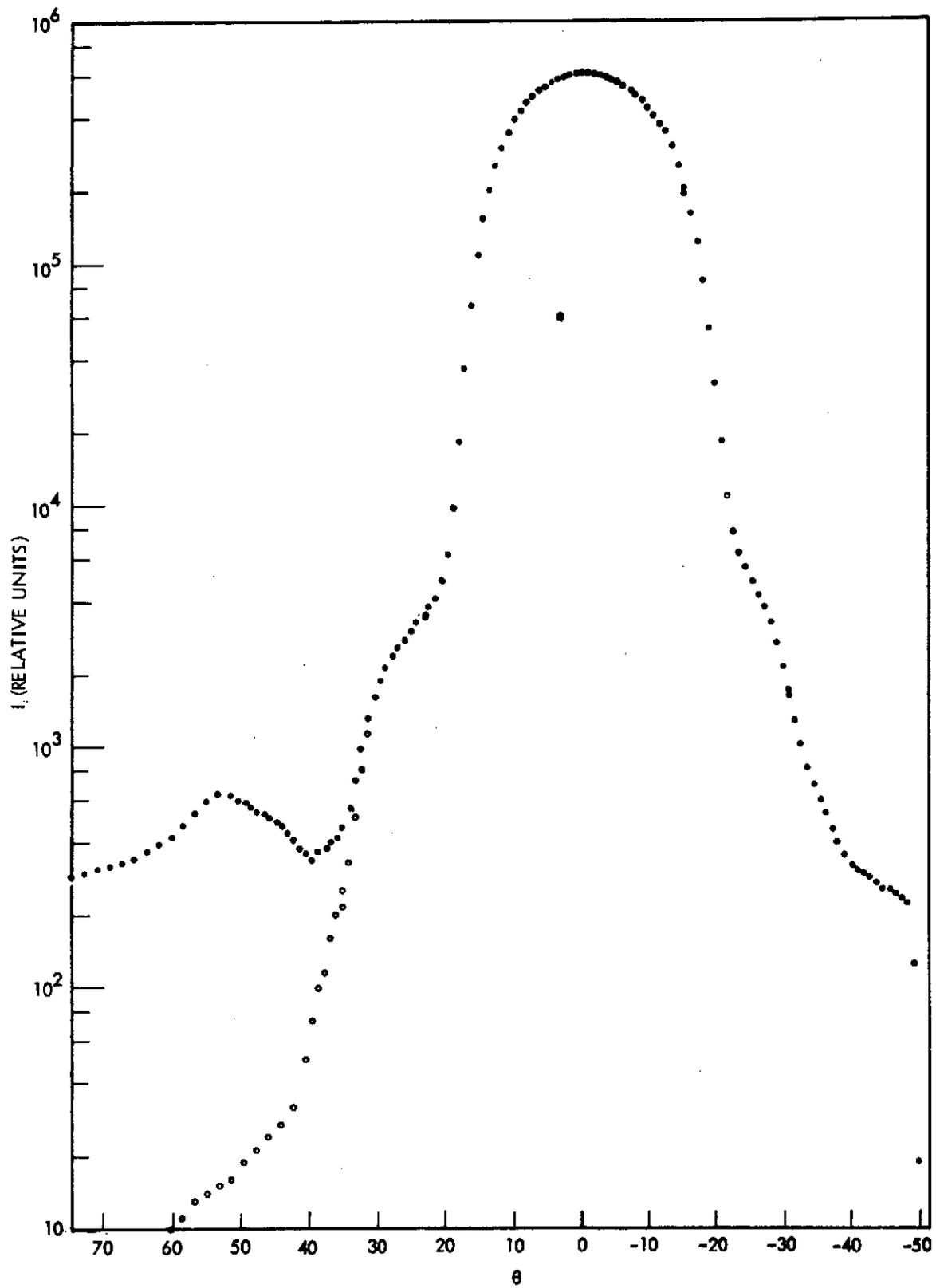
Figure 9-7. Ion Current Density Plot Showing Variation in
High-Angle Current Caused by a 10-Volt
Positive Bias on Probe Collector

9.3 ANALYSIS

As stated earlier, the program focused on the good coupling of the thrust beam to the spacecraft surface and the resulting surface contamination by the cesium ions. To better illustrate the environment of the spacecraft surface and downstream regions an ion number density (ions/cm^3) contour map was constructed. The data from Figure 9-4 were used in the calculation with a slight degree of fairing of the thrust ion and the low energy ion current density profiles. Also, the number density was assumed to fall off as $1/r^2$ with a point source located at the center of the thruster. Figure 9-8 is the ion number density contour map with the spacecraft surface and the plane across the top of the radiometer cone drawn in. Ion number densities in the region of the radiometer cone range from 4-8 x 10^5 ions/cm^3, and range for the major portion of the craft surface from 6 x 10^5 to 4 x 10^6 ions/cm^3. The ions in this region are predominantly low energy (~2 ev) cesium ions, and after ~30 hours of operation of the ion engine, with no preventative measures taken, one monolayer of cesium atoms will have been deposited on the radiometer cone entrance plane.

The source of the low energy cesium ions at high angles is believed to be the neutral cesium atoms released from the thruster which have charge-exchanged with the thrust beam ions. The propellant utilization of the cesium ion engine employed has not been determined; however, a propellant utilization of 95 percent is a reasonable estimate. Under normal operating conditions the total ion beam current was 0.11 ampere, which sets an upper limit for the total current of neutral cesium atoms released at 3 x 10^{16} atoms/sec. Thus, sufficient numbers of neutral atoms may be released to provide the currents of low energy ions observed.

The neutral cesium atom release distribution from the thruster and the thrust ion current density everywhere downstream is not known. Therefore, an exact calculation of the charge-exchange ion distribution and numbers could not be performed. But one can crudely calculate the probability that charge-exchange will occur for an atom along a series of trajectories starting from some specific point at the thruster. An estimation of the magnitude of the charge-exchange ion production and distribution could then be made.
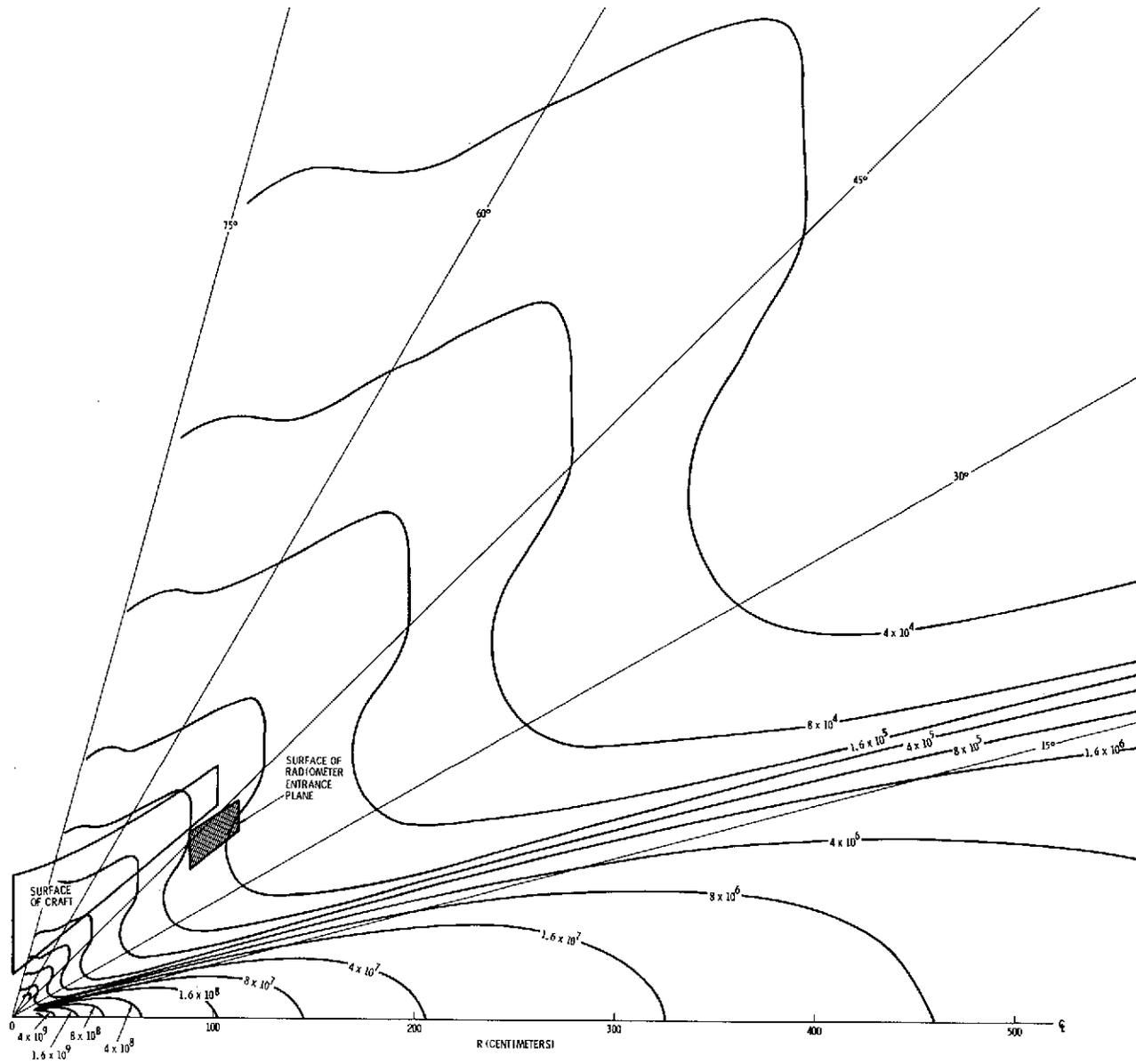
Figure 9-8. Ion Number Density Contour Map

First a contour map of the thrust ion current density (ions cm^{-2} sec^{-1}) was constructed. Two such maps were drawn, the first, Figure 9-9, used the data from Figure 9-4; and the second, Figure 9-10, used data from Figure 9-5. In the calculations for both maps, azimuthal symmetry about the beam axis and a $1/r^2$ fall-off were assumed, but the source point was taken to be located behind the ion source. This extended source model was employed since emphasis was placed on the thrust ion current densities in the near vicinity of the thruster. For Figure 9-9, the source point was located 17.2 centimeters behind the front surface of the thruster allowing, from the data, an order of magnitude fall-off in ion current density from the center to the edge of the thruster. The contour was not extended beyond a cone of half-angle >20 degrees (measured through the source point), since specification of current densities near the source outside the cone would be highly speculative and the contribution to the charge-exchange probability outside the cone will be negligible. In Figure 9-10, the source point was also located 17.2 centimeters behind the front surface of the thruster; however, for this case the ion current density at the center is a factor of two greater than at the edge of the thruster. This contour map was not used in the charge-exchange calculations since it is unlikely that the thruster would be operated under the same bias conditions. But, the current density contours have been extended to large angles to indicate ion current density levels which the spacecraft surface intercepts.

In order to calculate the probability, $P(z)$, that a neutral atom released from the thruster at $z = 0$, and moving through the thrust beam will charge-exchange with a thrust ion after traveling a distance z, the following relation must be evaluated:

$$P(z) = 1 - \exp\left[-\int_0^z \frac{\sigma j_+(z)}{v_o} dz\right]$$

where $\sigma = 4 \times 10^{-14}$ cm^2 (Reference 15) $j_+(z)$ is the thrust ion current density at z, and v_o is the neutral atom speed which is taken to be 2×10^5 cm/sec. $P(z)$ was evaluated for two release points for neutral atoms on the front surface of the thruster, one at the center and the other at the edge. The neutral atom trajectories will be straight lines,
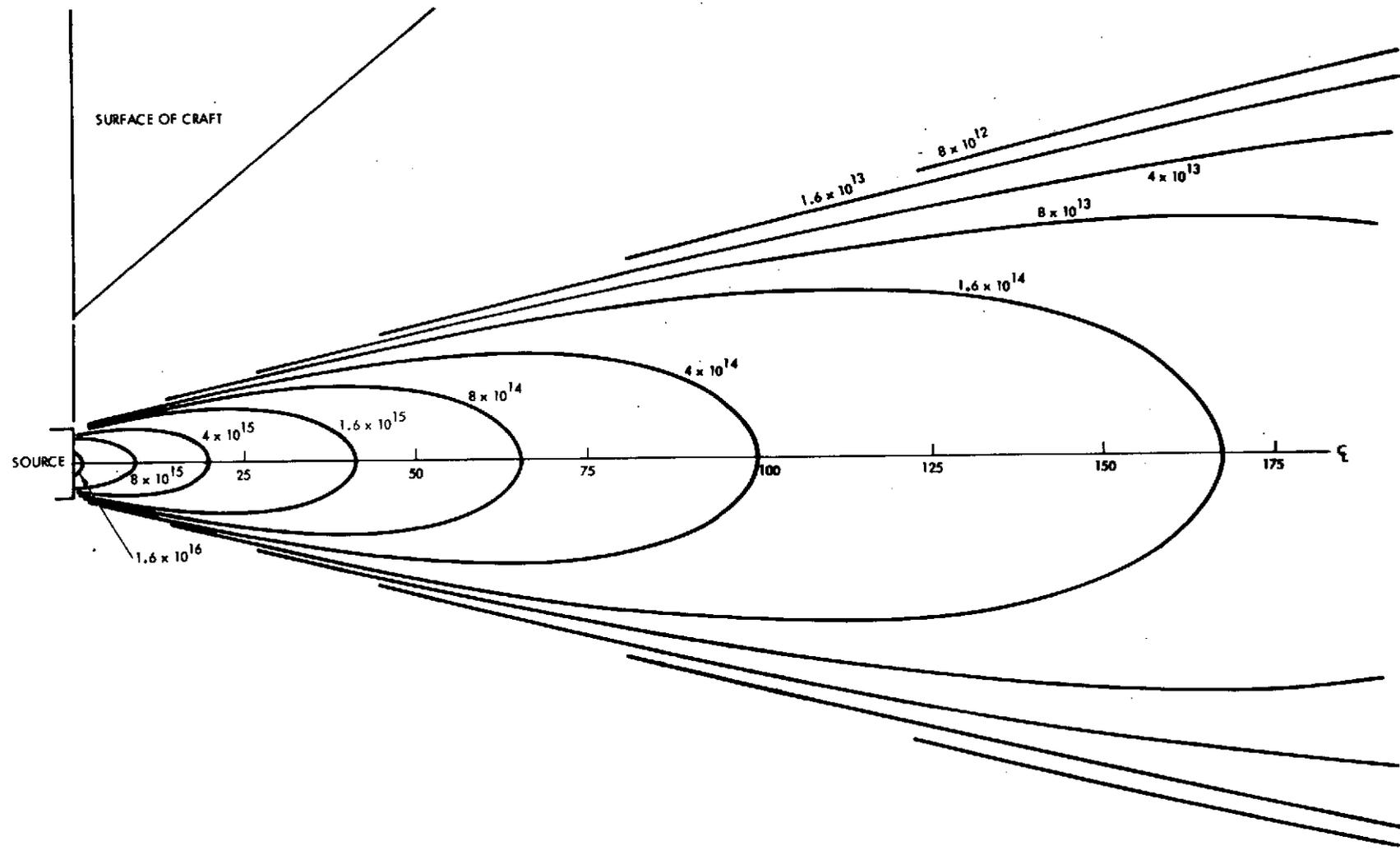
Figure 9-9. Ion Current Density Contour Map (Data from Figure 9-4)
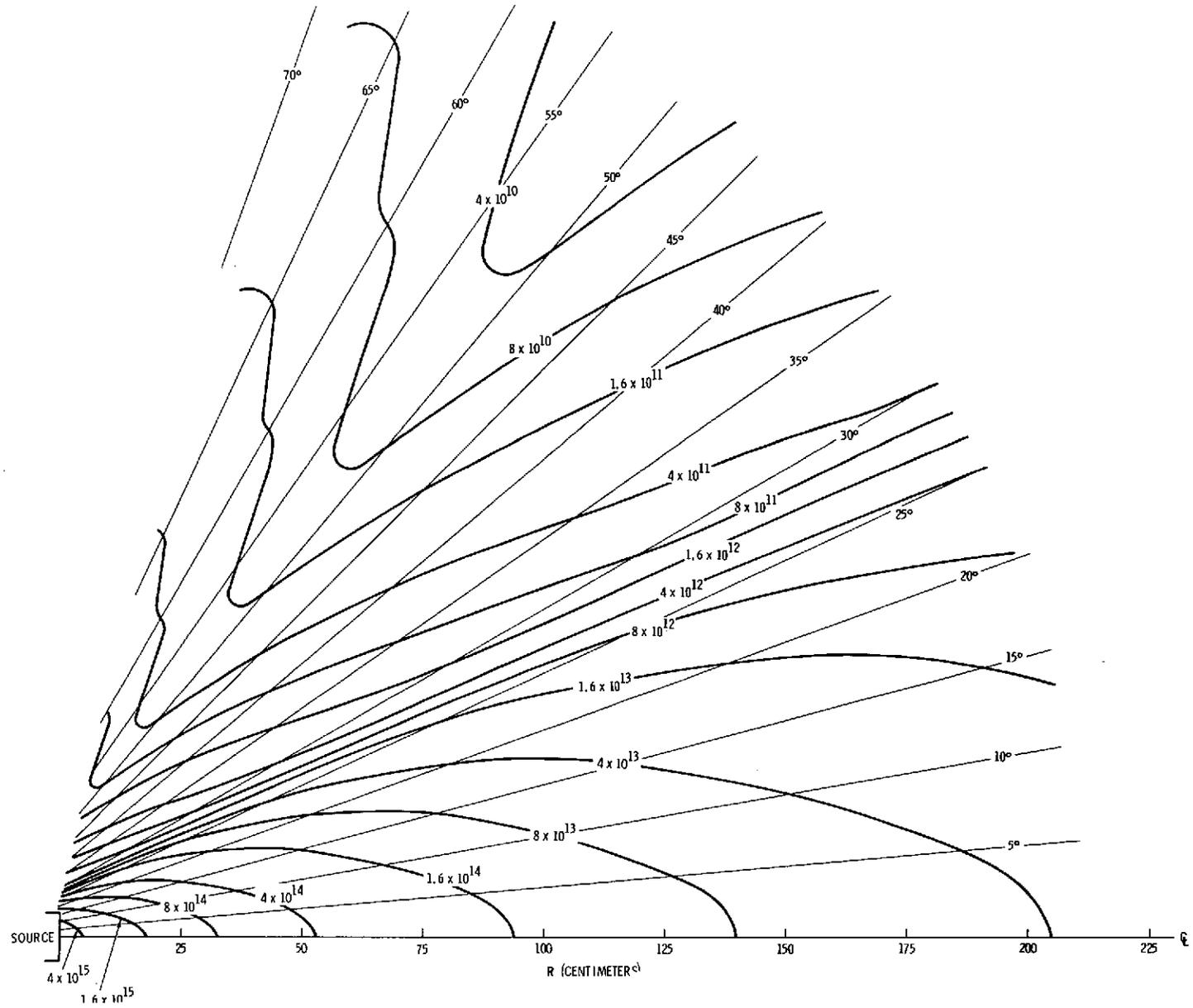
Figure 9-10. Ion Current Density Contour Map (Data from Figure 9-5)

and these trajectories were then drawn on Figure 9-9. From the figure one can now determine $j_+(z)$ along any trajectory and the integral in the exponential can be evaluated numerically. Figures 9-11 and 9-12 were then generated by calculating $P(z)$ along many different trajectories for the two release points. The contours indicate lines of constant $P(z)$ labeled in percent. For example, as shown in Figure 9-11, a neutral atom is released at the center of the source and travels along the axis of the beam. After moving 10 centimeters from the source, the atom has a 20 percent probability of undergoing charge-exchange with a thrust ion. Small deviations in the contour lines from smooth curves are a result of the numerical integration in that a small number of intervals were employed. From Figures 9-11 and 9-12 one can determine the charge-exchange probability for the two extreme neutral release points and then infer charge-exchange probabilities for any other release points on the thruster face.

After the first round of measurements, it was determined that the thruster beam behavior was similar to laboratory plasma beams encountered previously and that one could apply the electrostatic barometric equation to the thrust beam. Consequently, at any point along the axis of the thrust beam, because of the large density gradients in the radial direction, electric fields are present and in the radial direction. Therefore, the low energy charge-exchange ions are always being directed radially out of the thrust beam.

Originally, it was felt that the low energy charge-exchange ions could be repelled from the spacecraft surface by biasing the spacecraft surface positive with respect to the neutralizer and at least a few volts more positive than the plasma potential. However, independent measurements have indicated that the plasma potential in the injection region also increases as the surface bias is increased. Additionally, it appears that even when the craft surface was biased 28 volts above the neutralizer, the surface may still have been below the plasma potential in the region near the surface. Consequently, the injection potential for the electrons must have increased, resulting in increased electron temperature. This increased electron temperature would cause the thrust beam to broaden, as exhibited by Figure 9-5. When the thrust beam divergence increases,
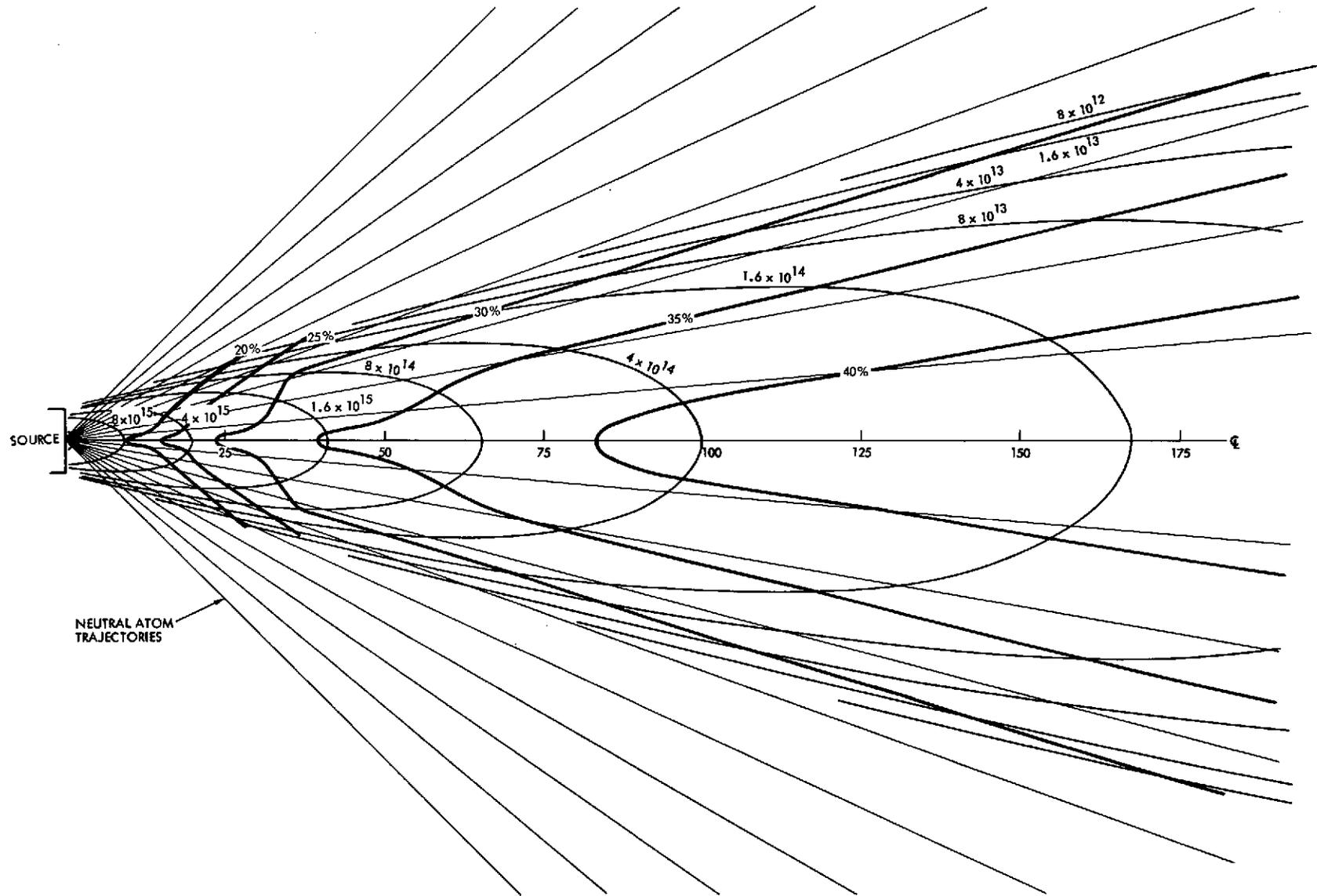
Figure 9-11. Charge-Exchange Probabilities for a Neutral Cesium Atom Released From the Center of the Thruster Face with 2 ev Average Energy
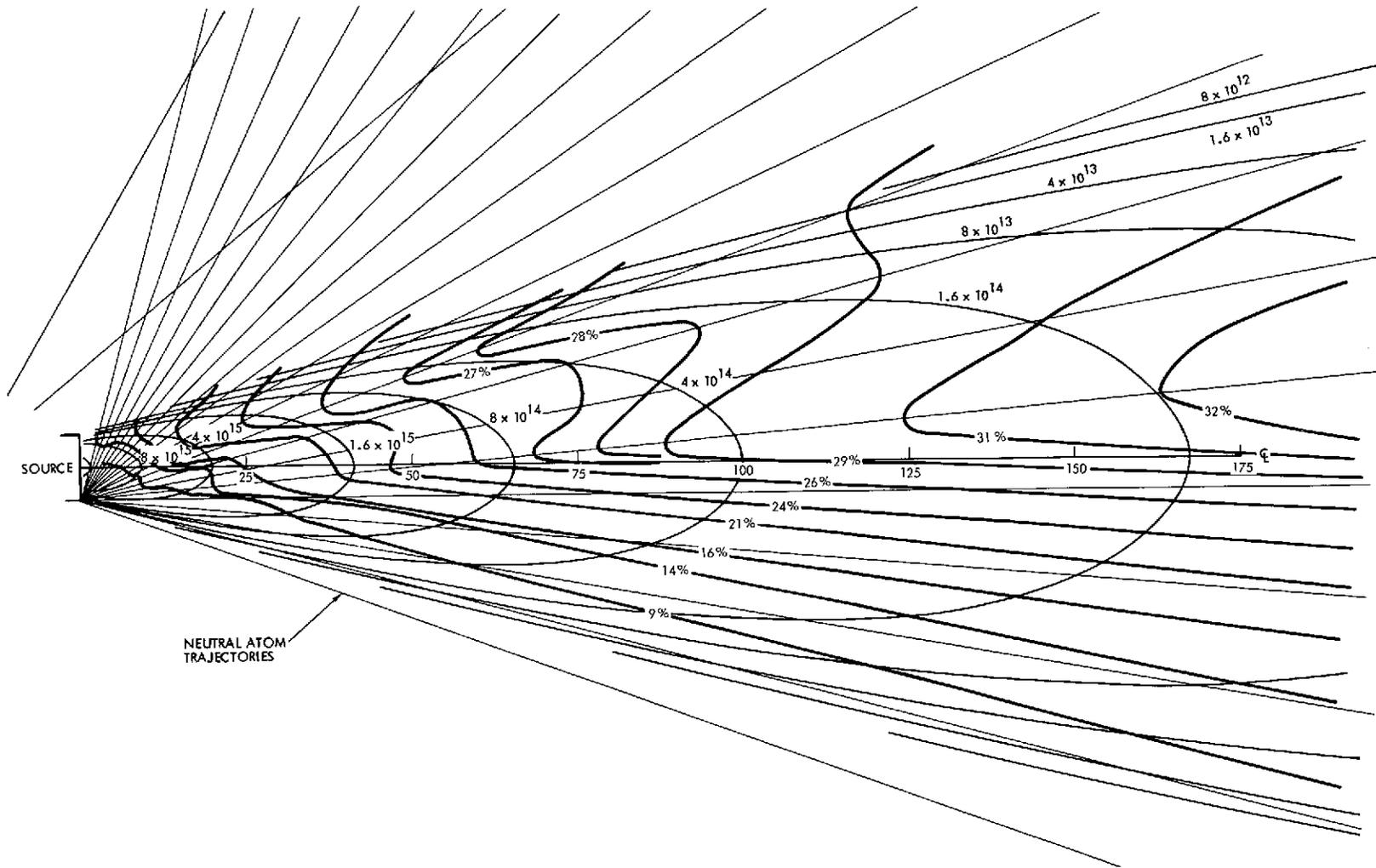
Figure 9-12. Charge-Exchange Probabilities for a Neutral Cesium Atom Released From the Edge of the Thruster Face with 2 ev Average Energy

the efficiency of the thruster decreases since the ions acquire radial velocity components. Also, of importance, Figure 9-10 indicates the spacecraft surface intercepts thrust beam ions which have enough energy to, in addition to possibly coating surfaces, erode spacecraft surfaces. Biasing only the tab which represents the radiometer cooler cone positive relative to the neutralizer, resulted in electron currents to this tab. Increasing the bias to +28 volts, tab much more positive than the plasma, did not cause the thrust beam to spread. At this bias, since the charge-exchange ions only have a few ev of energy, it should be energetically impossible for the charge-exchange ions to reach the tab. The exact relationship expressing the coupling of the neutralizer-thrust beam-spacecraft is not presently known and only a qualitative description of the effect has been given.

9.4 CONCLUSION

The configuration of the spacecraft having been fixed, the problem of coating the spacecraft surface and particularly the radiometer cooler cone with low energy charge-exchange cesium ions exists. Attempts at biasing the entire spacecraft surface positive 10 to 30 volts, relative to the neutralizer, to repel the charge-exchange ions have resulted in large electron currents from the thrust beam to the spacecraft surface and a spreading of the thrust beam. The surface of the spacecraft can still intercept thrust ions, which may coat or erode the surface. Also, the increase in divergence of the beam reduces the efficiency of the thruster. Hence, only the tab which represents the radiometer cooler cone was biased positive 28 volts relative to the neutralizer, the remaining spacecraft surface at neutralizer potential, to repel the charge-exchange ions. Electrons were still collected by the tab, but it should now be energetically impossible for charge-exchange ions to reach the tab. Also, there appears to be no detectable increase in thrust beam divergence, since the electron currents collected by the tab are much smaller than those observed for the entire spacecraft surface when it was biased positive. The total area and location on the spacecraft surface which can be protected from charge-exchange ion deposition, by this biasing technique, before the thrust beam character is altered, has not been determined. But, charge-exchange ions can be prevented from depositing on the radiometer cooler cone with no apparent alteration of thruster operation or behavior.

REFERENCES

1. D. F. Hall, "Evaluation of Electric Propulsion Beam Divergence Effects on Spacecraft," 08965-6013-RO-00, Final Report, Contract No. NAS7-575, TRW Systems, Redondo Beach, California, September 1969.

2. D. F. Hall, "Electrostatic Propulsion Beam Divergence Effects on Spacecraft Surfaces," Final Report, Vol. 1, JPL Contract 952350, Doc. No. 11985-6001-RO-00, TRW Systems, Redondo Beach, California, August 1970.

3. D. F. Hall, "Electrostatic Propulsion Beam Divergence Effects on Spacecraft Surfaces," Final Report, Vol. II, JPL Contract No. 952350, 17 January 1973.

4. J. F. Staggs, W. P. Gula, and W. R. Kerslake, "The Distribution of Neutral Atoms and Charge-Exchange Ions Downstream of an Ion Thruster," Journal of Spacecraft and Rockets, Vol. 5, No. 2, pp. 159-164, February 1968.

5. D. F. Hall, B. E. Newnam, and J. R. Womack, "Electrostatic Rocket Exhaust Effects on Solar-Electric Spacecraft Subsystems," Journal of Spacecraft and Rockets, Vol. 7, No. 3, pp. 305-312, March 1970.

6. D. F. Hall and L. R. Kelley, "Experimental Techniques to Determine Electrostatic Rocket Exhaust Effects on Spacecraft Surfaces," AIAA Paper 70-1144, September 1970.

7. D. F. Hall and H. E. Green, "Erosive and Chemical Effects of Energetic Mercury Ions Bombarding Spacecraft Surface Materials," AIAA Paper No. 72-446, April 1972.

8. L. R. Kelley, E. E. Luedke, and D. F. Hall, "Damage of Thermal Control Coating Proper Ties by Energetic Mercury Ion Bombardment," AIAA Paper No. 72-445, April 1972.

9. D. F. Hall and W. C. Lyon, "Low Thrust Propulsion System Effects on Communication Satellites," AIAA Paper No. 72-519, April 1972.

10. E. James, R. Worlock, T. Dillon, G. Gant, L. Jan, and G. Trump, "A One-Millipound Cesium Ion Thruster System," AIAA Paper No. 70-1149, September 1970.

11. R. Worlock, E. James, W. Ramsey, G. Trump, G. Gant and L. Jan, "A North-South Stationkeeping Ion Thruster System for ATS-F, AIAA Paper No. 72-439, April 1972.

12. J. M. Sellen, Jr., W. Bernstein and R. F. Kemp, "Generation and Diagnosis of Synthesized Plasma Streams," Rev. of Sci. Inst., 36, No. 3, pp. 316-322, March 1965.

13. T. Reynolds, "Analysis of Possible Cs-Ion Beam Interactions on the ATS-F," private communication to R. O. Bartlett, NASA/GSFC, July 8, 1971.

14. J. M. Sellen, Jr. , R. F. Kemp and R. H. Hieber, "Observation of Neutralized Ion Thrust Beams in the 25-Meter NASA Testing Chamber," 8603-6039-KU-000, Section III. G of "Investigation of Ion Beam Diagnostics," 8603-6037-SU-000, Final Report, Contract NAS8-1560, April 1964, TRW Systems Group, Redondo Beach, California, July 1964.

15. L. L. Marino, A. C. H. Smith and E. Caplinger, Phys. Ref. , 128, 2243 (1962).

APPENDIX
COMPARISON OF LABORATORY ION DOSAGES WITH MAXIMUM EXPECTABLE ION DOSAGES FOR ATS-F

During the Series I cesium ion beam tests, the ion source was able to deliver total ion dosages of from 2.7 to 7.0 x 10^{16} ions/cm^2 in each of several runs. As will be shown below, these values of maximum available ion doses are about 2 orders of magnitude greater than the "worst-case" dosages of low energy charge exchange ions which may arrive at sensitive surfaces of the ATS-F spacecraft during ion engine lifetime. If the neutralizer biasing scheme for protecting the spacecraft from charge-exchange ions performs as anticipated, the actual ion dosages will be negligible.

Numerical estimates of charge-exchange ion dosages for sensitive surfaces on the ATS-F spacecraft were given by Lyon in Reference A-1, for the case where no protection was to be afforded by electrical biasing. His calculations are reviewed here using updated geometrical relationships based on modifications to the spacecraft which resulted from Lyon's earlier calculations. Many of the assumptions used in the original calculation remain the same. It is assumed that the ion flux onto sensitive spacecraft surfaces is due to Group 4 ions, and that these ions are accelerated radially, at right angles to the primary beam direction, by a positive exhaust plasma potential of about 10 volts.

In repeating Lyon's calculations, we are again assuming that beam exhaust potential is above spacecraft potential, or that neutralizer potential is the same as spacecraft potential. Thus, no account is taken of the fact that a neutralizer biased negative with respect to the spacecraft can reduce or even remove the total Group 4 ion flux to the spacecraft. In this sense, these calculations represent a "worst case", or a failure mode type of operation.

The approximate Group 4 ion flux as derived by Lyon is as follows:

$$N(r,x) = QD^2 n\Gamma_0/8\bar{v}x \ [16(r/D)^4 + 8(r/D)^2 + 1]^{1/2} \qquad \text{(A-1)}$$

$N(r,x)$: $(cm^{-2}sec^{-1})$ The Group 4 ion arrival rate perpendicular to the surface of a cylinder of radius x whose axis is the thruster centerline

Q: (cm^2) The Cs^+/Cs^0 charge exchange cross section, taken as 3×10^{-14} cm^2 (Reference A-2)

D: (cm) Thruster exhaust port diameter, taken as 8.6 cm

n: $(cm^{-2}sec^{-1})$ Primary ion flux density at thruster exhaust port, taken as 10^{16}

Γ_0: $(cm^{-2}sec^{-1})$ Neutral flux at engine exhaust plane, taken as 10^{15}, corresponding to a propellant utilization efficiency of 90 percent

$\bar{v}$: (cm/sec) Average neutral velocity for a perfect 500°K Cs vapor, equal to 2.8×10^4 cm/sec

x: (cm) Perpendicular distance from thrust center-line to sensitive spacecraft surface

r: (cm) Perpendicular distance from the center of the ion engine exhaust plane to the plane of generation and movement of Group 4 ions of interest.

The application being investigated is relevant to the Series II testing. The sensitive spacecraft surfaces are the coated lens in the startracker, the specularly reflecting surface near the cold spot inside the radiometer sunshade and parts of the solar panels having a view of the thruster exhaust port. The geometrical layout of the first two surfaces with respect to the thruster is shown in Figure A-1. These two surfaces were analyzed for Group 4 ion incidence only. The solar panels were analyzed for primary beam incidence only.

Figure A-1 is not to scale. Critical dimensions were derived from available drawings. A point was chosen in front of the cold patch in the radiometer aperture at a location 3 inches north, 19 inches east and 47 inches down relative to the center of the thruster exhaust plane. A point in the entrance aperture of the furthest (most westerly) star tracker shade was found to have a location 2.1 inches north, 21.4 inches west and 37.5 inches down relative to the center of the thruster exhaust plane. The thruster exhaust beam points down and north, at an angle of 40 degrees from the vertical. A point on the bottom center of the solar panel was chosen, and was found to be at an angle of 73 degrees line of sight from the thrust centerline, and 280 inches from the center of the exhaust plane.

Group 4 Flux on Radiometer

With the given geometry, it was found that the bottom and eastern-most radiometer mirrors could see a charge-exchange ion flux from the exhaust beam, if it were not electrostatically repulsed. The cold-spot is shielded in any case.

Lyon's equation was used to calculate the arrival rate at the radiometer aperture, using values of $r = 96.2$ cm and $x = 86$ cm. The arrival rate is 2.3×10^9 cm^{-2} sec^{-1}. Lyon obtained a value of 2.2×10^{10} cm^{-2} sec^{-1} for values of $r = 65$ cm and $x = 81$ cm. The more up-to-date geometry is more favorable in producing a reduced Group 4 flux, but the differences are not only due to geometry. With the newer geometry, the graphs shown by Lyon give just a factor of two reduction. The other factor of five apparently comes from a difference in neutral and beam flux densities. In any case, the numbers can probably be regarded as compatible within the accuracy inherently obtainable by the method.

The arrival rate obtained from this equation is associated with a given direction, the direction of the distance x. This direction was found to be at an angle of about 40 degrees with both the bottom and east side mirror surfaces inside the radiometer. Thus, the net flux density onto the unshielded portions of each mirror is about 1.7×10^9 ions cm^{-2} sec^{-1}, if not electrostatically shielded.

ION ENGINE

THRUST BEAM

LOUVERS

STAR TRACKER SHADE

COLD PATCH

SPECULAR REFLECTOR

VHRR SHADE

GROUP 4 ION FLUX

EAST FACE

STAR TRACKER SHADE

NORTH FACE
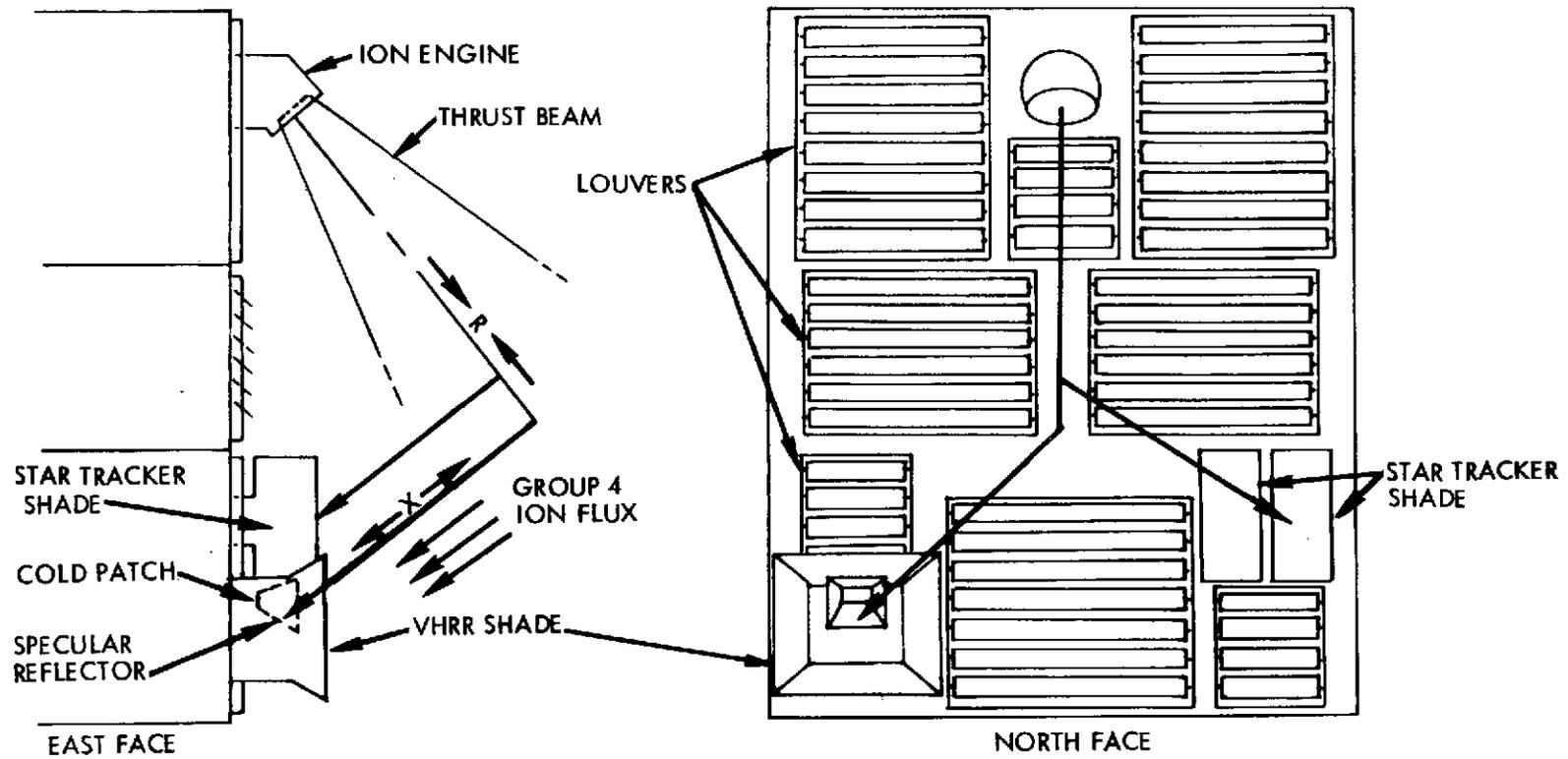
Figure A-1. Sketch Showing Relative Locations of Two of the Three Sensitive Surfaces of Concern in the Series II Ion Beam Tests

In computing total dose, the thruster rated operating time of 4400 hours is used. The effective dose rate may be expressed as 2.7×10^{-4} $\mu a/cm^2$. Over 4400 hours, the total dose is thus 2.7×10^{16} ions/cm^2 or 1.2 μa-hrs/cm^2.

The mirror temperature is approximately 200°K. Assuming a sticking coefficient of one for the charge exchange ions incident on the mirror, the time to form one monolayer is about 65 hours. A 4400-hour run will deposit nearly 70 monolayers.

The estimated energy of Group 4 ions incident on the radiometer mirrors is of order 10 volts, corresponding to internal beam potential, if the spacecraft is not electrostatically shielded.

Group 4 Flux on the Star Tracker Lens

The star-tracker lens is shielded by an aperture consisting of a housing and a series of baffles having a secondary field of view $\pm$ 14 degrees, 15 minutes about the sensitive plane and $\pm$ 29 degrees, 21 minutes about the insensitive plane. These angles define the extreme angles for light rays or particle trajectories to strike the lens. From this one can determine that particles arriving on the lens must always do so at an angle of incidence of less than 33 degrees from the normal. It was determined that Group 4 ions incident at the aperture of the outer (westernmost) star tracker have trajectories incident at 40 degrees from the normal. Thus the lens is shielded from all such trajectories.

The inner star tracker location was not considered. It is understood from available data that this star tracker is to be removed.

The arrival rate of Group 4 ions at the star tracker aperture was calculated assuming no neutralizer bias; again, a "worst case" type of assumption. The values r = 76.5 cm and x = 79.2 cm are appropriate for this geometry. Using these values in Lyon's equation, we obtain an arrival rate of 3.9×10^9 cm^{-2} sec^{-1} for charge exchange ions. The direction of incidence is again radially from the thrust beam, and at an incidence angle of 40 degrees from the normal (north-south) axis. Thus the arrival rate across the star tracker aperture plane is about 3.0×10^9 cm^{-2} sec^{-1}, for the case of no electrostatic shielding.

This is nearly equivalent to the flux on the radiometer mirrors. However, this flux is incident on the interior of the housing and baffles. If we assume that this flux reevaporates from the interior surface as neutral cesium and that half of it escapes again through the aperture, we can estimate a flux at the star tracker lens of about 1.5×10^9 cesium atoms cm^{-2} sec^{-1}. Furthermore, the energy of this flux will be closer to spacecraft temperature than to the Group 4 flux energy, and hence may be expected to stick rather than cause sputtering damage.

Incidence of Primary Beam Ions on the Solar Panels

A simplified analysis of the incidence of primary beam ions (550 volts Cs^+) on the solar arrays was done. A point midway along the underside of the solar panel was chosen. This point has a view of the exhaust port of the ion engine, at a distance of 280 inches, and an angle of 73 degrees from the thrust vector direction.

All points on the solar panel are located along lines of sight from the thruster having angles between 70 and 75 degrees from the thrust axis. These wide angles are well out of the primary beam. There is no data available on 550-volt ion incidence at these angles, and the veracity of any modeling done in the analysis is open to question. We chose to use the "near field model" supplied by Thaine Reynolds (Reference A-3) as representing a reasonable upper limit for flux density. The values obtained from this model are much greater, at these angles, than the values obtained from the corresponding "far field model".

The model is of the following form:

$$j = \bar{j} \, c(R_0/Z)^2 \, e^{-\lambda^n (1-\cos\theta)^n} \qquad (A-2)$$

where

  j: Primary ion current density
  $\bar{j}$: Average beam current density; 10^{16} ions/cm^2/sec
  R_0: Thruster port radius; 4.3 cm
  Z: (cm) Axial distance along thrust direction
  θ: Azimuth angle measured from thrust direction

Near field model parameters:

$c = 5.38$

$\lambda = 11.38$

$n = 1.76$

The calculation yields a flux density of 2×10^4 ions cm^{-2} sec^{-1}. Over a period of 4400 hours, the resulting total dose is about 1.0 ion/cm^2.

Thrust Vectoring

The effect of vectoring the thrust beam 7 degrees in the direction of the radiometer housing was investigated. We expect a change in Group 4 ion flux from two sources: (1) the change in the variables r and x in Lyon's equation and (2) the change in the angle of incidence. In this approximation, the net change due to both effects is less than five percent. A similarly small effect will hold for the star tracker.

When thrust vectoring is considered with respect to the solar arrays, the effect is more profound. The case considered is that in which the beam is deflected 7 degrees toward the solar panel. In Equation (A-2), the ratio of the exponential terms for angles of 73 and 64 degrees is about 5×10^5. This implies that if all of the ion engine operation were to take place with the maximum thrust vector deflection, the total primary ion dose would reach 5×10^5 ions/cm^2.

REFERENCES

A-1. W. C. Lyon, "Propellant Condensation on Surfaces Near an Electric Rocket Exhaust," Jour. Spacecraft and Rockets, Vol. 7 No. 12 p 1494, December 1970.

A-2. Perel, et al., Phys. Rev. 138, No. 4A, pp A937-A945, May 1965.

A-3. Letter of 8 July 1971 to Robert Bartlett, from Thaine Reynolds, Subject: Interactions of Cs Thruster on the ATS-F Satellite.